

Department of Micrometeorology  
University of Bayreuth, Germany

Characterisation of the  
atmospheric boundary layer in a  
complex terrain using  
SODAR-RASS

Diploma thesis  
in Geoecology

by Jens-Christopher Mayer

March, 2005

---

## Contents

Contents .....	II
Abstract .....	IV
Zusammenfassung .....	V
1. Introduction .....	1
2. Theoretical background .....	3
2.1 SODAR .....	3
2.1.1 Principle of acoustic sounding .....	4
2.1.2 Doppler shift .....	5
2.1.3 Calculation of the wind vector .....	6
2.1.4 Broadening of the backscattered spectra .....	7
2.1.5 Limitations of SODAR measurements .....	8
2.2 RASS .....	10
2.3 Wind and temperature profiles .....	12
2.4 Mixed layer height .....	14
2.5 Low-Level Jets .....	16
3. Material and Methods .....	19
3.1 Experiments WALDATEM-2003 and ECHO 2003 .....	19
3.2 Acoustic sounding system .....	21
3.2.1 Setup of the system .....	21
3.2.2 Determination of the height range .....	22
3.2.3 Detection of fixed echoes .....	23
3.2.4 Determination of the noise height .....	24
3.2.5 Sounding parameters for the continuous measurements .....	25
3.3 Data processing .....	26
4. Results and discussion .....	27
4.1 Comparison with tower measurements .....	27
4.2 Wind and temperature profiles .....	29
4.2.1 General characteristics .....	29
4.2.2 Profile dependence on stability parameter $\zeta$ and geostrophic conditions .....	32
4.2.3 Topographic effects on single profiles .....	39
4.2.4 Low-Level Jets .....	41

---

4.2.5	Shear layers .....	48
4.3	Development of the mixed layer .....	53
4.3.1	Observations of the development of the mixed layer .....	53
4.3.2	Model results of the development of the mixed layer .....	57
5.	Conclusions .....	61
6.	References .....	63
7.	Index of Figures.....	73
8.	Index of Maps.....	76
9.	Index of Tables .....	77
10.	Index of the used abbreviations and symbols.....	78
11.	Appendix A .....	81
12.	Appendix B.....	83
	Acknowledgements .....	85
	Eidesstattliche Erklärung.....	86

## Abstract

This work investigates wind- and temperature profiles at a complex meteorological measurement site in a mountain range. In complex terrain, the wind field is strongly affected by topography, and thus the profiles strongly depend on wind direction. The knowledge of these dependencies is important for the interpretation of measurements performed at this site.

The wind- and temperature profiles were obtained during the complex exchange experiment WALDATEM-2003 from May to July 2003, using a SODAR system METEK DSDPA.90/64 with a 1.29 GHz RASS extension. The experiment was conducted at the Waldstein Weidenbrunnen measurement site in the Fichtelgebirge mountains, NE Bavaria, Germany. The site is located at the NE flank of the mountains on a saddle, 765 m above sea level. Additional measurements for a comparison between the SODAR-RASS system and measurements from a meteorological tower were carried out during the ECHO 2003 campaign at the Research Centre Jülich, Germany from July to August 2003. The evaluated wind- and temperature profiles have a height resolution of 20 m and a maximum height of 1 km above ground level.

In this study the occurrence of wind shear layers under different wind directions is presented. Further investigations focus on the development of the mixed layer and the occurrence of low-level jets at a complex site, results being compared experiments in flat terrain or urban regions. For the Waldstein Weidenbrunnen site, the wind direction's frequency distribution indicated three main wind directions, defining three main sectors: North, Southeast and West. Wind profiles within the North sector were characterised by a counter clockwise turn with increasing height and frequently occurring low-level jets, wind profiles within the Southeast sector showed a clockwise turn of the wind by up to  $90^\circ$  with increasing height and a secondary wind maximum in the bottom 200 m. Profiles within the West sector showed an exponential increase of the wind speed and a clockwise turn of the wind by  $30^\circ$  with increasing height. An evaluation of wind profiles under different conditions of atmospheric stability revealed a significant influence of the topography especially for the Southeast sector. Three low-level jet events were observed during the experiment. Their duration ranged from one to ten hours, with peak wind speeds between  $9 \text{ ms}^{-1}$  and  $12 \text{ ms}^{-1}$ , all three occurred for wind directions from the north sector. The development of the mixed layer was derived after different criteria for several days, results were compared to model calculations. Elevating rates for the mixed layer height were found to vary between  $140 \text{ mh}^{-1}$  and  $400 \text{ mh}^{-1}$ .

---

## Zusammenfassung

Die vorliegende Arbeit untersucht Wind- und Temperaturprofile an einem komplexen Mittelgebirgsstandort. In gegliedertem Gelände wird das Windfeld stark von der Topographie beeinflusst. Dadurch ist die Form der Wind- und Temperaturprofile stark von der Windrichtung abhängig. Diese Abhängigkeiten spielen eine große Rolle bei der Interpretation von meteorologischen Messungen an einem derartigen Standort.

Die Wind- und Temperaturprofile wurden während des Experiments WALDATEM-2003 im Zeitraum von Mai bis Juli 2003 mit Hilfe eines SODAR-Systems METEK DSDPA.90/64 in Kombination mit einer 1,29 GHz RASS-Erweiterung gemessen. Die Messungen fanden am Messfeld Waldstein Weidenbrunnen im Fichtelgebirge, NE Bayern statt. Das Messfeld befindet sich im Bereich der NE-Flanke des Fichtelgebirges auf einer Sattelstruktur in 765 m ü. NN. Weitere Messungen für einen Vergleich des SODAR-RASS Systems mit Messungen eines meteorologischen Masten wurden von Juli bis August 2003 während der ECHO 2003 Kampagne am Forschungszentrum Jülich durchgeführt. Die ausgewerteten Temperatur- und Windprofile haben eine Höhenauflösung von 20 m und einer Reichweite bis zu 1 km über Grund.

Neben der mittleren Windstatistik für den Experimentzeitraum wird das Auftreten von intensiven Scherungsschichten bei bestimmten Windrichtungen beschrieben. Die Entwicklung der Mischungsschicht sowie das Auftreten von Low-Level Jets in gegliedertem Gelände werden untersucht und mit Ergebnissen von Experimenten aus dem Flachland bzw. aus städtischem Umfeld verglichen. Die Häufigkeitsverteilung der Windrichtung zeigte drei Hauptrichtungen, die zur Abgrenzung dreier Hauptsektoren herangezogen wurden: einem Nordsektor, einem Südostsektor und einem Westsektor. Windprofile des Nordsektors wiesen eine Drehung gegen den Uhrzeigersinn mit zunehmender Höhe auf und waren geprägt durch häufig auftretende Low-Level Jets. Im Südostsektor zeigten die Windprofile eine starke Drehung bis zu 90 ° im Uhrzeigersinn mit zunehmender Höhe. Dazu trat ein sekundäres Windmaximum innerhalb der untersten 200 m über Grund auf. Der Westsektor wies Profile mit einer exponentiellen Windzunahme und eine leichten Drehung um 30 ° mit zunehmender Höhe auf. Eine Auswertung der Profile unter verschiedenen Stabilitätsbedingungen zeigte insbesondere für den SE Sektor einen ausgeprägten Einfluss der Topographie. Während des Experimentes wurden drei Low-Level Jet Ereignisse beobachtet, alle bei nördlichen Windrichtungen. Sie dauerten zwischen einer und zehn Stunden und erreichten Spitzenwindgeschwindigkeiten von 12 ms<sup>-1</sup>. Die

Entwicklung der Mischungsschicht wurde nach verschiedenen Kriterien für mehrere Tage abgeleitet und mit Ergebnissen eines Modells verglichen. Die beobachteten Anwachsraten der Mischungsschicht lagen zwischen  $140 \text{ mh}^{-1}$  und  $400 \text{ mh}^{-1}$ .

## 1. Introduction

The main objective of this study is the meteorological characterisation of the Waldstein site up to the lower atmospheric boundary layer. This characterisation is important for measurements within the surface layer as well as for model calculations concerning the origin of substances in the atmosphere. Strong wind shear with height complicates assumptions about the origin of air masses at the site, as it can cause different trajectories within different layers (Roth et al., 1989). Additionally, strong wind shear within the lower atmospheric boundary layer can enhance the atmospheric turbulence in the entire layer down to the surface and it affects the dynamic stability of the atmosphere, causing exchange processes to increase (see e.g. Hanna and Chang, 1992). Basic characteristics of wind and turbulence at the Waldstein site are already being investigated in the surface layer (Mangold, 1999), and the atmospheric turbulence above the canopy up to a height of 140 m has been subject to detailed research (Thomas et al., 2005). In this study, the characterisation of the site is extended up to a height of 1 km. Wind profiles were chosen for this characterisation as wind flow is strongly affected by topography and the profiles describe the behaviour of the wind flow from near the surface up to altitudes well beyond the surface layer. The profiles are analysed for the influence of the topography under different atmospheric stability conditions with regard to local wind statistics.

To describe wind profiles above the surface layer where common theoretical descriptions of the wind profile cannot be applied, only a few methods exist. For extrapolations from single point measurements, usually performed near the ground, one approach is to use the power law (Justus and Mikhail, 1976; Doran and Verholek, 1978; Irwin, 1978; Sedefian, 1980; Joffre, 1984; Hsu et al., 1994). Alternative attempts are discussed by Göckede (2000). A physically exact solution of the equation of motion with the geostrophic wind as the upper boundary, is provided by the resistance law (Blackadar and Tennekes, 1968; Wippermann, 1973; Zilitinkevich, 1989). As most of the experiments used to develop and validate these methods were performed at sites with more or less flat terrain, these laws can only be acceptable for undisturbed flows. Obstacles like mountains or canalising valleys in the direction of the approaching flow cause complex effects on the wind field. Therefore, information about the real wind profile up to the geostrophic height level is needed to properly characterise a site in complex terrain. This information can only be obtained from measurements, e.g. with SODAR sys-

tems, as parameterisations cannot account for the individual topography's influence on the wind profile.

When dealing with wind profiles, a phenomenon called the low-level jet must be considered. A low-level jet is a thin stream of fast moving air with maximum wind speeds of  $10 \text{ ms}^{-1}$  to  $20 \text{ ms}^{-1}$  usually located in a height of 100 m to 300 m (Stull, 1988). Due to the intense shear turbulence can be induced above and below the jet, even if the atmosphere is regarded to be statically stable stratified (Hanna and Chang, 1992; Reitebuch et al., 2000). This turbulence can influence flux measurements and change the concentration of chemical constituents (Beyrich, 1994; Corsmeier et al., 1997). Therefore part of the characterization of the Waldstein site is the analysis of low-level jets, namely their frequency of occurrence and their intensity.

An important parameter at every measuring site is the height of the mixed layer. It indicates the depth of the layer in which conservative variables such as potential temperature and humidity are nearly constant with height due to the mixing processes (Stull, 1988). The mixed layer height is an important scaling parameter because it influences parameters of the surface layer (Panofsky et al., 1977; Peltier et al., 1996; Johansson et al., 2001), discussed by Thomas (2001). It is frequently derived from boundary layer models (e.g. Blackadar, 1997) as it cannot be determined from direct, ground-based measurements. Another approach to determine the height of the mixed layer are remote sensing techniques such as SODAR systems (see e.g. Emeis et al., 2004) for which simple criteria are given by Beyrich (1997) and Seibert et al. (2000). Up to now the determination of the mixed layer height using remote sensing techniques was done mainly at sites in flat terrain (e.g. Beyrich, 1995). To complete the characterization of the Waldstein site, mean characteristics of the observed development of the mixed layer as well as single day observations are presented and compared with results of the Blackadar (1997) model.

## 2. Theoretical background

The following chapter provides an overview of the theoretical background for the sounding system used as well as the properties of the atmospheric boundary layer that was investigated. The first part deals with the historical development of SODAR systems and the difficulties associated with its operation whereas the second part adds the theory of the RASS technique. Thirdly, the theoretical background for the wind and temperature profiles is presented. The last section introduces the theory for determining the mixed layer height from SODAR data.

### 2.1 SODAR

The first acoustic sounding system was developed by the English physicist Tyndall. He observed sound scattering from turbulence while studying the propagation of sound waves through sea fog (Tyndall, 1874). The term SODAR, an acronym of sound detecting and ranging, appears in the paper from Gilman et al. (1946) for the first time dealing with the fading of radar signals under particular atmospheric conditions. After the theoretical problem of sound scattering by turbulence was first formulated and generally solved by Obukhov (1941), in the following two decades the fundamental theory of sound wave scattering was established by Obukhov (1943), Blokhintzev (1946a; 1946b), Tatarskii (1961; 1971) and Monin (1962) in Russia and Kraichnan (1953), Lighthill (1953) and Batchelor (1957) in the USA. These new findings stimulated scattering experiments of Kallistratova (1959), leading to Monin's (1962) calculation of the scattering cross section in terms of the spectra of temperature and velocity, which agreed with the results of Batchelor (1957). An important step towards the modern SODAR system was made by McAllister (1968), McAllister and Pollard (1969a) and McAllister et al. (1969b) who were the first to use a facsimile recording of echo intensity. This height-time cross section will be referred to as a sodagram. Therefore it was possible to get a picture of the temporal variation of the atmosphere's acoustic reflectivity. The first Doppler SODAR measurements began with high-frequency bistatic scattering experiments of Kelton and Bricout (1964). Since then the efficiency of SODAR systems has been enhanced to measure real-time profiles of wind velocities up to several hundred meters above the ground. A SODAR system belongs to the group of remote sensing systems. The basic concept of a SODAR system can be monostatic or bistatic. In the bistatic system, the emitting and the receiving antenna are separated, monostatic systems have one antenna with transceivers, i.e.

combined transmitters and receivers, which are switched into receiving mode after the sound pulse is emitted. Since we used a monostatic system, further explanations will be limited to this type of SODAR.

Two different technical solutions for the beam steering of a monostatic SODAR system exist. The older type consists of one separate antenna for each beam. That means, such a SODAR has at least three big transducer tubes. The newer type consists of a phased array of transducers. In this case, the beam steering is electronically controlled by applying a distinct phase shift from one row to the next when emitting a sound pulse. Due to interference, the resulting beam is tilted against the zenith over the edges of the mount. If there is no phase shift between the rows of the transducers, the pulse is emitted vertically. With a square shaped mount five logical antennas are available, one vertical and four tilted antennas. The beam angle against zenith depends on air temperature and the acoustic frequency. It increases with decreasing air temperature and decreasing frequency.

### 2.1.1 Principle of acoustic sounding

A sound pulse of a well defined audible frequency is emitted from the SODAR antenna. While propagating through the atmosphere, a small fraction of the energy is scattered back to the receiving antenna of the SODAR. The scattering elements are small-scale temperature inhomogeneities of a typical size distribution, transported with the mean wind flow (Kallistratova, 1997). These temperature inhomogeneities are due to turbulence in regions of changes in potential air temperature. They can be associated with thermal plumes originating from surface heating or with gradients of the potential temperature, as can be found at inversion layers. Enhanced turbulence at shear layers increases the development of such inhomogeneities. To receive a maximum of returned energy, the scale of these inhomogeneities  $l_i$  must be similar to the wavelength of the acoustic frequency  $\lambda_a$ . This dependency is known as the Bragg condition (Eq. ( 1 ) ), where  $\Theta_B$  is the Bragg angle (i.e. the angle of incidence of the acoustic pulse).

$$l_i = \frac{\lambda_a}{(2 \sin \Theta_B)} \quad (1)$$

In the case of ideal backscattering where the Bragg angle equals  $90^\circ$ , the relation between the scale of the inhomogeneity and the acoustic wavelength simplifies to Eq. ( 2 ).

$$l_i = \frac{1}{2} \cdot \lambda_a \quad (2)$$

When temperature inhomogeneities of adequate scale are present, the transmitted  $P_T$  and received  $P_R$  acoustic power are related to one another as shown in Eq. (3) from Little (1969)

$$\frac{P_R}{E_R} = P_T E_T e^{-2(\alpha_c + \alpha_m)R_s} \frac{c_a \tau}{2} \frac{AG}{R^2} \sigma \alpha_e, \quad (3)$$

where  $A$  is the antenna aperture,  $\alpha_c$ ,  $\alpha_m$  and  $\alpha_e$  are the classical, molecular and excess attenuation,  $c_a$  is the speed of sound,  $E_R$  and  $E_T$  is the efficiency of received and transmitted power,  $G$  is the effective aperture factor,  $R_s$  is the distance of the scattering volume from the antenna,  $\sigma$  indicates the scattering cross section and  $\tau$  is the length of the transmitted pulse.

In the case of a monostatic SODAR, the scattering cross section is given by the expression (Tatarskii, 1971)

$$\sigma = 0.0039 k^{1/3} \frac{C_T^2}{T^2}, \quad (4)$$

where  $C_T^2$  is the temperature structure parameter,  $k$  is the acoustic wave number, which is  $2\pi/\lambda_a$  and  $T$  is the ambient air temperature.

The received signal is recorded at a high frequency and the obtained time series is subdivided into gates which correspond to discrete height intervals of the atmosphere. The allocation of these gates to a height above ground is calculated from an estimated speed of sound, adjusted by a standard temperature measurement near the SODAR. For each gate the intensity and mean frequency of the backscattered signal is determined. The intensity of the backscattered signal correlates with the refraction structure function parameter  $C_N^2$ . Eq. (5) shows the dependency of  $C_N^2$  on  $C_T^2$  (Wyngaard et al., 1971), where  $p$  is the mean air pressure.

$$C_N^2 = \left( 79.2 \cdot 10^{-6} \cdot \frac{p}{T^2} \right)^2 \cdot C_T^2 \quad (5)$$

### 2.1.2 Doppler shift

The backscatter intensity leads to profiles of acoustic reflectivity of the atmosphere. When the received mean frequency is compared to the emitted frequency, a slight shift can be determined. This shift is known as the Doppler shift. Two different cases need to be distinguished:

a displaced transmitter and a displaced receiver. If the receiver remains steady and the transmitter is displaced towards the receiver, the wave fronts of the emitted sound are compressed. This compression leads to a decreased wavelength of the propagating sound. The acoustic frequency  $f$  and  $\lambda_a$  are described by the expression

$$\lambda_a = \frac{c_a}{f}. \quad (6)$$

As a result of the shorter wavelength, the receiver records a higher frequency compared to the emitted one. If the transmitter is moving away from the receiver, the emitted sound wave is protracted, which results in a lower received frequency. In the second case, the transmitter remains steady and the receiver is moved. When moving towards the transmitter, i.e. contrary to the approaching sound waves, the time between identical phases is reduced, which means the frequency of the acoustic wave seems to be increased. When moving the receiver away from the transmitter in the direction of the propagating sound wave, the time between two identical phases becomes longer, resulting in a lower received frequency. More detailed explanations of the Doppler effect can be found in textbooks of physics, e.g. Alonso and Finn (1967).

In the case of a SODAR, the acoustic pulse is scattered back by the inhomogeneities of temperature, travelling with the mean air flow. As these inhomogeneities act as the transmitter of the backscattered sound, the second case of the Doppler shift is valid for a SODAR system. The Doppler shift is only dependent on the relative velocity between transmitter and receiver, i.e. between the inhomogeneity and the receiving antenna. The radial wind velocity  $v_r$  along the beam axis of a monostatic SODAR is given by Eq. (7), where  $f_e$  and  $f_s$  are the emitted and the backscattered (received) frequency.

$$v_r = -\frac{c_a}{2} \left( \frac{f_s}{f_e} - 1 \right) \quad (7)$$

### 2.1.3 Calculation of the wind vector

The three dimensional wind vector can be calculated, if at least three independent radial wind velocities are determined. By measuring radial wind speed along the vertical pointing antenna  $a_3$  and along one of the tilted antennas and knowing the tilt angle against zenith  $\psi$ , the hori-

zonal component for the tilted antenna can be obtained. From two horizontal components perpendicular to each other the horizontal wind speed  $v_h$  can be calculated (see Figure 1).

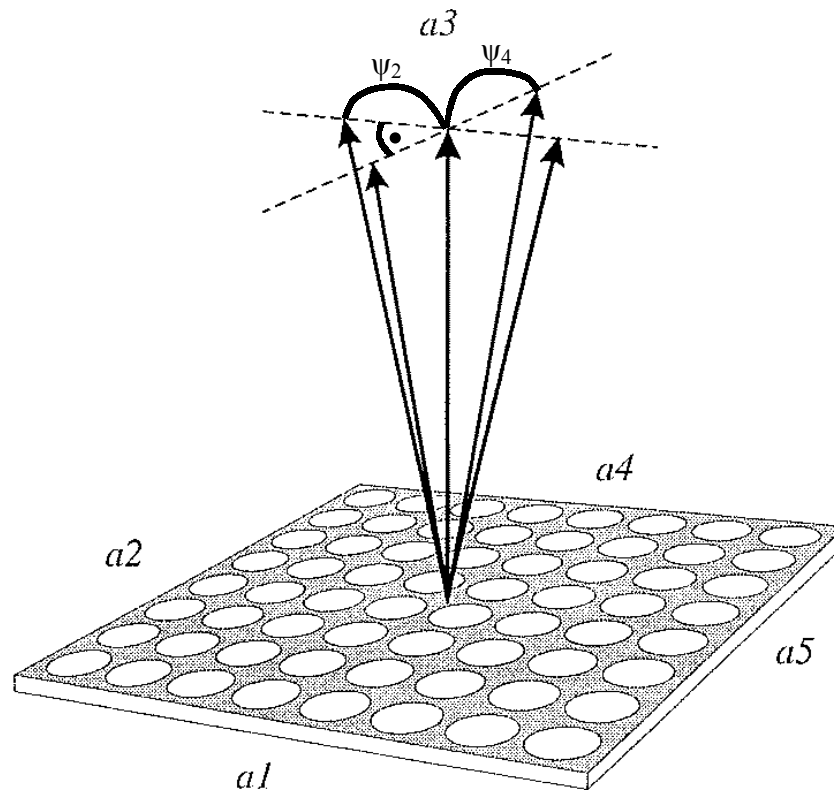


Figure 1: Square shaped phased array with resulting five antennas ( $a1 - a5$ ). The angles against zenith are indicated as  $\psi_2$  and  $\psi_4$ , the horizontal angle between the antennas is  $90^\circ$ . From: METEK, DSDPA.90 user manual, modified.

### 2.1.4 Broadening of the backscattered spectra

An important parameter for the turbulence state is the standard deviation of the vertical wind velocity  $\sigma_w$ . It is used in dispersion models such as that from Blackadar (1997) and to derive diffusion categories (Pasquill, 1961). It can be obtained from the high frequent time series of the vertical wind velocity  $w$  (e.g. Quintarelli, 1993) or from the broadening of the mean backscattered spectra. When  $\sigma_w$  is derived from the broadening of the mean backscattered spectra, the spectra of several soundings are averaged in frequency space. The broadening of the mean spectra compared to the emitted single spectrum is proportional to  $\sigma_w$ . Some difficulties concerning measurements of  $\sigma_w$  with the SODAR technique result from the greater averaging time and the greater sampling volume, compared to sonic measurements (Keder et al., 1988). As Finkelstein et al. (1986) have shown, SODARs tend to overestimate  $\sigma_w$  when its value is low and to underestimate it when it is large. Thomas and Vogt (1993) found a general under-

estimation of  $\sigma_w$  from SODAR measurements compared to those from ultrasonic anemometer measurements.

When  $\sigma_w$  is derived from the broadening of the spectra, the contribution of the background noise to the received spectrum must be eliminated. Therefore the spectrum of the background noise is measured prior to each sounding and then subtracted from the received spectrum. Given a high level of noise, the spectrum after this correction is smaller than the emitted one, resulting in a negative broadening, which leads to negative calculated values of  $\sigma_w$ . When  $\sigma_w$  is derived from the high frequent time series of the vertical wind velocity, negative values of  $\sigma_w$  can not occur, as  $\sigma_w$  is calculated following Eq. ( 8 ).

$$\sigma_w = \sqrt{\frac{1}{n} \sum (\bar{w} - w')^2} \quad (8)$$

Here  $n$  denotes the number of samples,  $\bar{w}$  is the mean vertical wind velocity and  $w'$  is the fluctuation of the vertical wind velocity.

### 2.1.5 Limitations of SODAR measurements

The dominant physical limitation of SODAR measurements is the attenuation of the acoustic waves while propagating through the atmosphere. Three different forms of attenuation must be distinguished. The first is the classical attenuation  $\alpha_c$  (Eq. ( 3 )) due to the effects of viscosity, heat conduction, and molecular diffusion. Its behaviour is well known and it is small compared to the two remaining forms of attenuation for frequencies usually used by SODAR systems (Neff, 1975). Molecular attenuation  $\alpha_m$  (Eq. ( 3 )) occurs due to the excitation of the internal energy modes of  $O_2$  molecules during the passage of the acoustic waves (Neff, 1975). This type of attenuation increases rapidly with increasing acoustic frequency especially at lower relative humidity (Harris, 1966). For more details concerning the attenuation of sound in the air see (Harris, 1963) and (Harris, 1966). Classical and molecular attenuation are basically functions of temperature and humidity. Figure 2 shows the dependence of  $\alpha_c$  and  $\alpha_m$  on the acoustic frequency. The third type of attenuation is the excess attenuation  $\alpha_e$ . The excess attenuation describes the loss of acoustic intensity due to turbulent beam broadening and refraction by the wind (Neff, 1978; Mouldsley and Cole, 1980). This parameter causes a reduction in the backscattered signal intensity. Haugen and Kaimal (1978) showed that  $\alpha_e$  increases with increasing acoustic frequency, which results in a decreasing beam width, and with increasing wind speed.

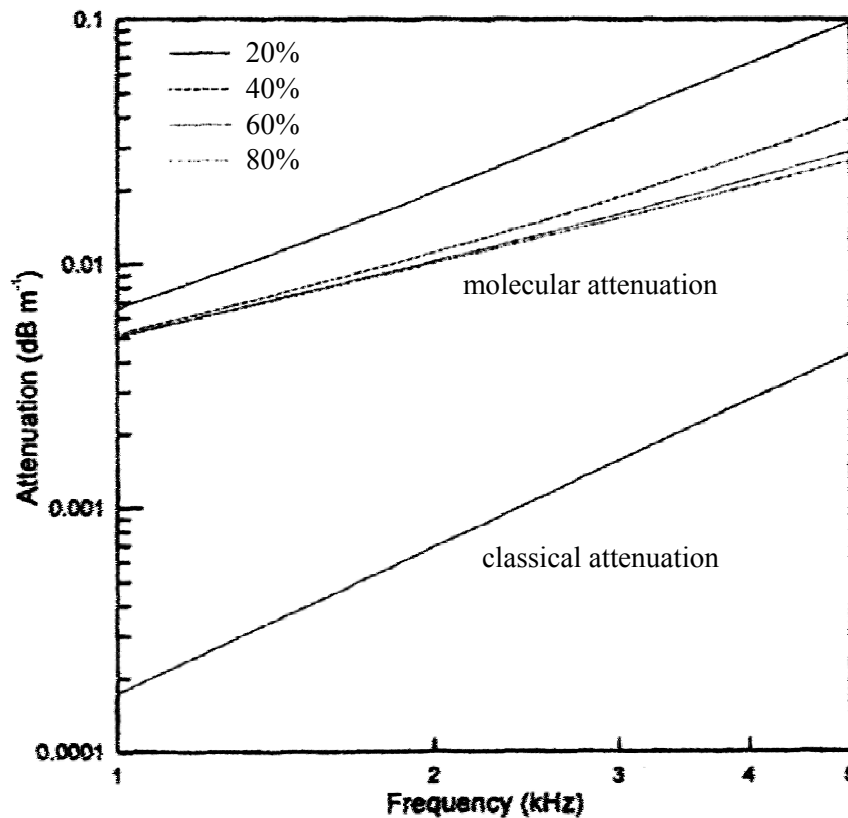


Figure 2: Classical and molecular attenuation as a function of acoustic frequency. These curves are based on equations given by Neff (1975) for a temperature of 20 °C (Crescenti, 1998).

The contribution of  $\alpha_e$  to the total attenuation is smaller than from  $\alpha_c$  and  $\alpha_m$ , but cannot be neglected (Moulsley et al., 1979). As a SODAR system works in the audible frequency range, the amount of environmental noise added to the backscattered signal can strongly limit its ability for wind velocity determination. In a noisy environment, the critical step is to differentiate between the Doppler-shifted backscattered signal and the ambient background noise (Neff and Coulter, 1986). The sources of background noise can be classified into active and passive sources. These can be subdivided into broad-band or narrow-band (Crescenti, 1998). Most of the ambient noise is active and broad-band. It can overlap the acoustic sounding frequency of the SODAR and effectively decreases the signal-to-noise ratio, SNR. The SNR is defined as the ratio of the level of the information bearing signal power to the level of the noise power, measured in decibels (dB). The result is a decrease of the maximum vertical range of the measurements. As the backscattered power decreases exponentially with height, higher gates are more susceptible to being lost. Sources of narrow-band active noise like birds or insects affect the SODAR performance in different ways depending on their type. If the noise sources have a frequency component within the frequency range of the SODAR, they

can be misinterpreted as a valid backscattered signal. The result is an erroneous wind value which can be found in all gates. If the noise is too strong, the receiver can get saturated, resulting in a missing value for the wind velocity. To minimise such difficulties, the site should be selected very carefully. It should be free of extraneous ambient background noise in order to get a maximum sounding range and correct wind data for all measured heights.

Besides the active noise, the passive noise can cause severe problems. Passive noise sources are objects that reflect a part of the transmitted acoustic pulse back to the SODAR. Typical sources of passive noise are buildings, towers and trees. While most of the transmitted energy is focused in a narrow beam, sidelobes do exist (Simmons et al., 1971). They cause a small amount of acoustic energy to be transmitted almost horizontally. If these waves hit a reflecting stationary object, they return to the antenna with zero Doppler-shift. This type of signal is therefore called a fixed-echo. It will be interpreted by the SODAR as a valid wind speed of  $0 \text{ ms}^{-1}$  due to the zero Doppler-shift. Often it is not possible to predict whether an object will cause fixed-echoes or not. In general, a site for SODAR measurements should be as free as possible of any obstacles, and the tilted beams should point away from obstacles. Nevertheless, a critical search for influenced data should be done when installing a SODAR system or after changes take place in the system's vicinity.

Finally, it should be kept in mind that operating a SODAR system in a populated area can cause some annoyance to the residents.

## 2.2 RASS

The RASS (radio acoustic sounding system) technology is a method of remotely determining atmospheric temperature profiles by combining acoustic and RADAR (radio detecting and ranging) techniques. RASS systems can be designed as an individual system or as a RADAR extension for a SODAR system. The main advantage is to get instantaneous temperature profiles. RASS systems track the acoustic wave fronts with a Doppler RADAR to determine the speed of sound  $c_a$ . It was first studied by Fetter (1961). The speed of sound is related to the acoustic temperature  $T_a$ , which is almost equal to the virtual temperature  $T_v$  (Kaimal and Gaynor, 1991).

$$T_a = T \cdot \left( 1 + 0.32 \cdot \frac{e}{p} \right) \quad (9)$$

$$T_v = T \cdot \left( 1 + 0.38 \cdot \frac{e}{p} \right) \quad (10)$$

Here  $e$  is the water vapour pressure.

Further development of RASS systems were made by Marshall et al., (1972) and the method was later extended to larger sounding ranges (Matuura et al., 1986; May et al., 1988).

In a RASS system, the RADAR detects backscattered radiation from fluctuations in the refractive index of the air induced by an emitted sound pulse. The Doppler shift of the backscattered signal yields the vertical propagation speed of these density perturbations, i.e. the speed of sound. Strong backscatter is only obtained when the Bragg condition holds, i.e. the acoustic wavelength  $\lambda_a$  is half of the RADAR wavelength  $\lambda_e$ , and the almost spherical acoustic wave fronts are not drifted away due to strong wind, so that the backscattered signal is focused onto the receiver antenna (May et al., 1988).

$$\lambda_e = 2 \cdot \lambda_a \quad (11)$$

A theoretical analysis of the backscattered electromagnetic power and the SNR was performed by Marshall (1972).

Gating the returns provides the required height resolution. Out of the various combinations of sound source and radio source combinations, the following explanations deal with a constant radiating RADAR and a pulsed sound source. In case of the Doppler RASS which will be considered here, the Doppler-shift of the reflected electromagnetic waves yields the speed of sound. The gating is determined from the product of the travel time of the sound wave and  $c_a$ , where  $c_a$  is calculated from a standard temperature measurement. The returned Doppler-shifted RADAR signal is evaluated in every gate and  $c_a$  is calculated. The functional relation to the acoustical temperature is

$$T_a = \frac{c_a^2 \cdot M}{\kappa \cdot R} = \left( \frac{c_a}{20.047} \right)^2, \quad (12)$$

where  $\kappa$  is the adiabatic coefficient of air,  $M$  is the molar mass of air and  $R$  is the universal gas constant.

Experiments to check the ability of RASS systems to provide reliable measurements of  $T_v$  showed a very good agreement with radiosonde and tower observations (May et al., 1989; Vogt et al., 1990). The application of Bragg's law (see Eq. ( 1 )) to RASS measurements im-

poses certain complexities. To receive a clear RADAR signal, the Bragg condition must hold. As the speed of light is not effected by air temperature and wind, the relation between electromagnetic frequency and electromagnetic wavelength is fixed. Thus the required wavelength of the acoustic wave  $\lambda_a$  is the same at every height. As the air temperature and therefore  $c_a$  change with height and time, the relation between  $\lambda_a$  and the acoustic frequency  $f_a$  changes constantly. Therefore, the sound pulse of the RASS system must cover a sufficient range of frequencies to ensure the presence of a matching wavelength in every gate.

### **2.3 Wind and temperature profiles**

The wind velocity and their variation with height within the atmospheric boundary layer ABL is governed by a balance of large-scale horizontal pressure gradients, the roughness characteristics of the surface and the Coriolis force due to the rotation of the earth. This balance is modified by the diurnal cycle of heating and cooling which changes the thermal stratification of the ABL and by topographical features with their local or mesoscale effects on the wind flow (Arya, 2001).

In great altitudes, where the influence of the surface roughness vanishes, the wind vector is only the result of the balance of the pressure gradient force and the Coriolis force if advective and local accelerations are neglected. This wind is called the geostrophic wind (Arya, 2001).

At the earths surface the wind velocity vanishes. This is known as the no-slip condition for viscous fluids and is stated routinely in textbooks on fluid mechanics (see e.g. Batchelor, 2000). As the retarding influence of the rough surface on the wind is present within the whole ABL, the wind speed is forced to decrease gradually with decreasing altitude. Thus the geostrophic balance between pressure gradient and Coriolis force is modified by the frictional drag within the ABL. As the pressure gradient force is independent of the wind speed but the Coriolis force is not, the latter decreases with decreasing wind speed. This causes the wind to turn into the direction of the pressure gradient. This counter-clockwise turn with decreasing altitude is called Ekman spiral (Ekman, 1905; Taylor, 1915) and has typical values of around 30 ° between the geostrophic flow and the flow near the ground.

A simple description of the shape of the wind speed profile within the ABL is given by the power law (Doran and Verholek, 1978; Joffre, 1984; Hsu et al., 1994)

$$\frac{u_1}{u_2} = \left( \frac{z_1}{z_2} \right)^p. \quad (13)$$

Here,  $z_1$  and  $z_2$  denote two different measuring heights,  $u_1$  and  $u_2$  are  $v_h$  in measuring height  $z_1$  or  $z_2$  and  $p$  is the power-law exponent. Eq. (13) can be used to extrapolate the wind profile into the ABL from only one measured value of  $v_h$ , if  $p$  is known. For the parameterization of  $p$  several methods exist. Justus and Mikhail (1976) proposed a parameterization, where  $p$  depends only on  $v_h$  in a reference height. Other authors (Peterson and Hennessey, 1978) suggested a constant value of  $1/7$ , but this parameterization was only intended to calculate the annual amount of energy in the mean flow. Irwin (1978) presented a functional relationship of  $p$  to the surface roughness and the atmospheric stability, using the Monin-Obukhov similarity theory (Monin and Obukhov, 1954). For more concerning Monin-Obukhov similarity theory see textbooks of micrometeorology, e.g. Stull (1988), Kaimal and Finnigan (1994), Arya (2001), Foken (2003). These universal functions are valid only in the surface layer. Thus Irwin (1978) restricted the validity of his parameterization up to 160 m under neutral conditions and up to 100 m under stable or unstable conditions. Another parameterization accounting for stability and surface roughness was found by Sedefian (1980), who did not restrict the validity of the calculated profiles although universal functions are involved. To avoid a restriction to the surface layer, Sedefian (1980) proposed a simplified parameterization, using the stability classes after Pasquill (1961) with some modifications instead of the universal functions. More details concerning the Pasquill classes of atmospheric stability can be found e.g. by Blackadar (1997). A comparison between the described parameterizations can be found at Sedefian (1980).

The resistance law (Blackadar and Tennekes, 1968) provides an exact description of the wind profile in the ABL. It is a solution of the equation of motion. Variations of this law exist for different conditions of the atmospheric stability and stationarity (Wippermann, 1973; Zilitinkevich, 1989). The resistance laws use the geostrophic wind as an upper boundary condition for the calculation of the wind profile. The shape of the wind profile is defined by a parameter  $\mu$ , which accounts for the atmospheric stability, and the two parameters  $A(\mu)$  and  $B(\mu)$ , which are universal functions of the resistance law. As the ABL is very complex, the empirical evaluations of the parameters  $A(\mu)$  and  $B(\mu)$ , are very wide spread. More recently it was found, that  $A$  and  $B$  do not only depend on  $\mu$  but additionally depend on the Brunt-Väisälä fre-

quency (Zilitinkevich and Esau, 2002) and on the altitude of a capping inversion (Hess, 2004). This constrains the practical use of the resistance law. A detailed description of the mentioned methods can be found at Göckede (2000).

The mean temperature profile under dry adiabatic conditions is basically characterised by the dry adiabatic lapse rate, which is  $0.98 \text{ Km}^{-1}10^{-2}$ . This decrease of the temperature with increasing height is caused by the expanding air with decreasing pressure. The relation between changes in pressure and in temperature are given by the Poisson equation

$$\frac{T_2}{T_1} = \left( \frac{p_2}{p_1} \right)^\kappa, \quad (14)$$

where  $T_1$  and  $T_2$  are the mean temperature at height one and two,  $p_1$  and  $p_2$  are the mean air pressure at height one and two and  $\kappa$  is the adiabatic coefficient of air. Replacing  $T_1$  by  $\theta$  and defining a reference pressure of 1000 hPa instead of  $p_1$  leads to the definition of the potential temperature  $\theta$  (Eq. (15)), which is a measure for the heat content of the air.

$$\theta = T \cdot \left( \frac{1000}{p} \right)^\kappa \quad (15)$$

When replacing  $T$  by  $T_v$ , Eq. (15) gives the virtual potential temperature  $\theta_v$ . It includes the water vapor into the calculation of heat content of the air. Increasing values of  $\theta_v$  with increasing height indicate a statically stable stratified boundary layer and are typical for thermal inversions. Decreasing values for  $\theta_v$  are typical for unstable boundary layers. Under condensing conditions, as are in clouds or fog, the lapse rate is decreased due to the release of latent heat from condensation. Therefore the saturated adiabatic lapse rate is approx.  $0.6 \text{ Km}^{-1}10^{-2}$  (see e.g. Arya, 2001). As the heat content of the air changes during condensation processes, Eq. (15) is not valid under condensing conditions.

## 2.4 Mixed layer height

A short introduction into the dynamics of the ABL, the mixed layer height MLH and its definitions will be given in this section. A typical diurnal variation of the ABL can be seen in Figure 3. After sunrise, there is strong evolution of the convective boundary layer CBL, resulting in a mixed layer ML and a capping inversion above.

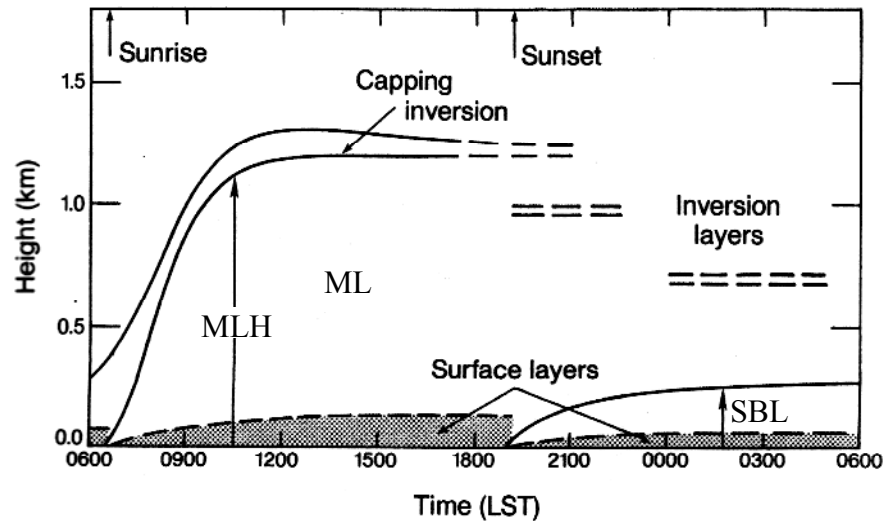


Figure 3: Evolution of the convective and stable boundary layers in response to surface heating and cooling. The time indicated is Local Standard Time LST (Kaimal and Finnigan, 1994, modified).

When the heating due to the radiation stops in the evening, the mixing process decays, and the cooling surface of the earth establishes a more and more stable boundary layer SBL. The air from the preceding CBL lays as a residual layer above the nocturnal SBL. This diurnal cycle is strongly modified by clouds or changes of air masses, resulting in a stronger or weaker occurrence of the mentioned effects.

For the ML, Beyrich (1997) and Seibert et al. (2000) give the following definition: Substances emitted into the ABL are gradually dispersed horizontally and vertically through the action of turbulence, and finally become completely mixed over this layer if sufficient time is given and if there are no significant sinks. As the substances are finally mixed over the entire layer, the term ML will be used in this study for the layer, and MLH for its vertical dimension. The terms mixing layer and mixing layer height, which can often be found in the literature, are taken as equivalent to mixed layer and mixed layer height. Several definitions for the MLH can be found in the literature (see Arya, 1981; Stull, 1988; Garrat, 1992; Seibert et al., 1998). Thus when dealing with the MLH, the applied definition has to be explained. Different methods of determining the MLH give different results under the same conditions, and probably none of them fits exactly to the above mentioned definition. As Seibert et al. (2000) explain, it is necessary to distinguish between the SBL and the CBL. For a CBL the common definition is the height where the heat flux gradient reverses its sign. This height is often used for scaling purposes. The SBL is much shallower than the CBL (Arya, 2001). It can be divided into a layer of continuous turbulence adjacent to the ground, and an outer layer of sporadic turbu-

lence. For scaling purposes, only the continuous turbulent layer is usually used (Seibert et al., 2000).

For determining the MLH from SODAR data, typical features of the backscatter intensity can be used to determine the MLH. Under stable conditions, a strong decrease above a region of less variable  $C_T^2$  due to shear produced turbulence can be found. As a criterion for the determination of the MLH from SODAR data, the upper boundary of a ground-based echo layer can be used. Results from comparisons of SODAR measurements with MLHs derived from temperature and wind profiles are quite inconsistent (Arya, 1981; Hanna et al., 1985). For more information concerning the determination of the MLH under stable conditions see Beyrich and Weill (1993). For the CBL, an elevated maximum of reflectivity at the top of the ML is a typical indicator of the MLH (Beyrich, 1997; Seibert et al., 2000). Some authors recommend the use of the lower boundary of this layer (Frisch and Clifford, 1974; Kaimal et al., 1982), other authors prefer the centre or the upper envelope (Noonkester, 1976). More criteria can be found at Beyrich (1997). Field studies to compare MH values derived from different measurement systems under convective conditions can be found e.g. by Russel et al. (1974), Noonkester (1976), Coulter (1979), Kaimal et al. (1982), Baxter (1991), Marsik et al. (1995) and Emeis et al. (2003; 2004). As the direct determination of the MLH from the profiles of reflectivity is restricted to situations when the MLH is within the technical operating range of the SODAR system, several attempts were made to obtain at least an estimate of the MLH for a deep CBL. Different methods are discussed by Beyrich (1995).

The ABL can exhibit very different shapes, for example a stable stratification with or without secondary maximums of wind speed, or a unstable stratification with or without capping inversions. Therefore it has proven to be impossible to derive the MLH by automatic algorithms from SODAR data (Beyrich, 1997; Coulter and Kallistratova, 2004), especially over complex terrain. One conclusion of an intercomparison study with independent estimates of the MLH stated: “hand reduction of the facsimile data estimated a more accurate mixing height than did the automatic routine” (Baxter, 1991).

## **2.5 Low-Level Jets**

Low-level jets LLJ modify wind profiles in several ways. The monotone increase of  $v_h$  with increasing height is altered to a strong increase below the jet and a decrease with increasing above. Due to the intense shear of  $v_h$ , turbulence is induced above and below the jet, causing

some mixing even if the atmosphere is determined to be stably stratified. In this section, the manifestation of a LLJ is described as well as its definitions from the profiles of wind speed and the conditions for its genesis.

A LLJ is a thin stream of fast moving air with maximum wind speeds of  $10 \text{ ms}^{-1}$  to  $20 \text{ ms}^{-1}$  usually located in a height of 100 m to 300 m (Stull, 1988). The occurrence of a LLJ has been observed at several sites in the world (see e.g. Kraus et al., 1985; Reitebuch et al., 2000; Banta et al., 2002; Engelbart et al., 2003; Lau and Chan, 2003). It was found, that the duration of a LLJ event can last up to several days and that it is not strongly limited to night times. But in most cases the LLJ event reaches its peak during the predawn hours. Therefore a LLJ is often designated as a nocturnal jet. A lot of different criteria to identify a LLJ in the datasets are known. Some criteria require a maximum of  $v_h$  greater than a specified threshold below a specific height (Bonner, 1968), others have the requirement of a supergeostrophic maximum of  $v_h$  (Brook, 1985). Stull (1988) defines a LLJ as occurring whenever there is a relative wind speed maximum that is more than  $2 \text{ ms}^{-1}$  faster than the wind speed above it within the lowest 1500 m of the atmosphere. Further classifications are given by Bonner (1968) and Mitchel et al. (1995). This classes are shown in Table 1.

Table 1: Categories of LLJ given by Bonner (1968) with the additional category 1 given by Mitchel et al. (1995).  $\Delta v$  indicates the drop of  $v_h$  above the jet. The highest category with fulfilled requirements is valid.

Cat. 0	$v_{h \text{ max}} > 0 \text{ ms}^{-1}$	$z (v_{h \text{ max}}) < 1.5 \text{ km}$	No limit
Cat. 1	$v_{h \text{ max}} \geq 10 \text{ ms}^{-1}$	$0 < z (v_{h \text{ max}}) < 3 \text{ km}$	$\Delta v \geq 5 \text{ ms}^{-1}$
Cat. 2	$v_{h \text{ max}} \geq 12 \text{ ms}^{-1}$	$0 < z (v_{h \text{ max}}) < 3 \text{ km}$	$\Delta v \geq 6 \text{ ms}^{-1}$
Cat. 3	$v_{h \text{ max}} \geq 16 \text{ ms}^{-1}$	$0 < z (v_{h \text{ max}}) < 3 \text{ km}$	$\Delta v \geq 8 \text{ ms}^{-1}$
Cat. 4	$v_{h \text{ max}} \geq 20 \text{ ms}^{-1}$	$0 < z (v_{h \text{ max}}) < 3 \text{ km}$	$\Delta v \geq 10 \text{ ms}^{-1}$

Beside this descriptive classification, a more genetic definition was given by Blackadar (1957), Buajitti and Blackadar (1957) and Holton (1967), who associated a LLJ with inertial oscillations and baroclinity associated with sloping terrain. According to Stull (1988) and Kraus et al. (1985) the occurrence of a LLJ is associated with at least one of the following situations:

- advective accelerations
- fronts
- land and sea breezes

- synoptic-scale baroclinity associated with weather patterns
- splitting, ducting and confluence around mountain barriers
- mountain and valley winds
- inertial oscillations
- baroclinity associated with sloping terrain.

A LLJ can be caused by more than one of these factors (Stull, 1988).

### 3. Material and Methods

This chapter provides information about the experiments and the data processing. The first section describes the experimental setup, section two provides information about the used equipment and the determination of sounding settings. The last part deals with the data treatment before the evaluation.

#### 3.1 Experiments *WALDATEM-2003 and ECHO 2003*

All data used in this study were obtained during two separate field experiments, namely the WALDATEM-2003 (WAVElet Detection and Atmospheric Turbulence Exchange Measurements) experiment (Thomas et al., 2004) and the ECHO 2003 (Emission and Chemical transformation of biogenic volatile Organic compounds) experiment (Koppmann, 2003).

The experiment WALDATEM-2003 was carried out from May to July 2003 at the Fichtelgebirge in the northeastern part of Bavaria, Germany at 765 m above sea level (Figure 4). The site is covered by spruce forest with an average canopy height of 19 m. The SODAR-RASS system was located in a small clearing (50°08'39''N, 11°52'00''E, approx. 100 x 200 m) in a distance of approx. 300 m apart from the flux tower station DE-Wei of the CarboEurope Cluster, where continuous eddy covariance measurements are performed using sonic anemometers and fast response gas analyzers.

The ECHO 2003 campaign was conducted from July to August 2003 at the Research Centre Jülich (Figure 5). It aimed on a better understanding of forest stands as a complex source of reactive trace gases into the troposphere. The mean canopy height of the forest surrounding the research centre was 30 m. The SODAR system was located in a large clearing of approx. 500m x 500m bearing the waste water treatment plant of the Research Centre Jülich. The 120 m tall meteorological tower of the Research Centre Jülich was used for comparisons with the SODAR measurements. A detailed description of the site can be found in Aubrun et al. (2004).

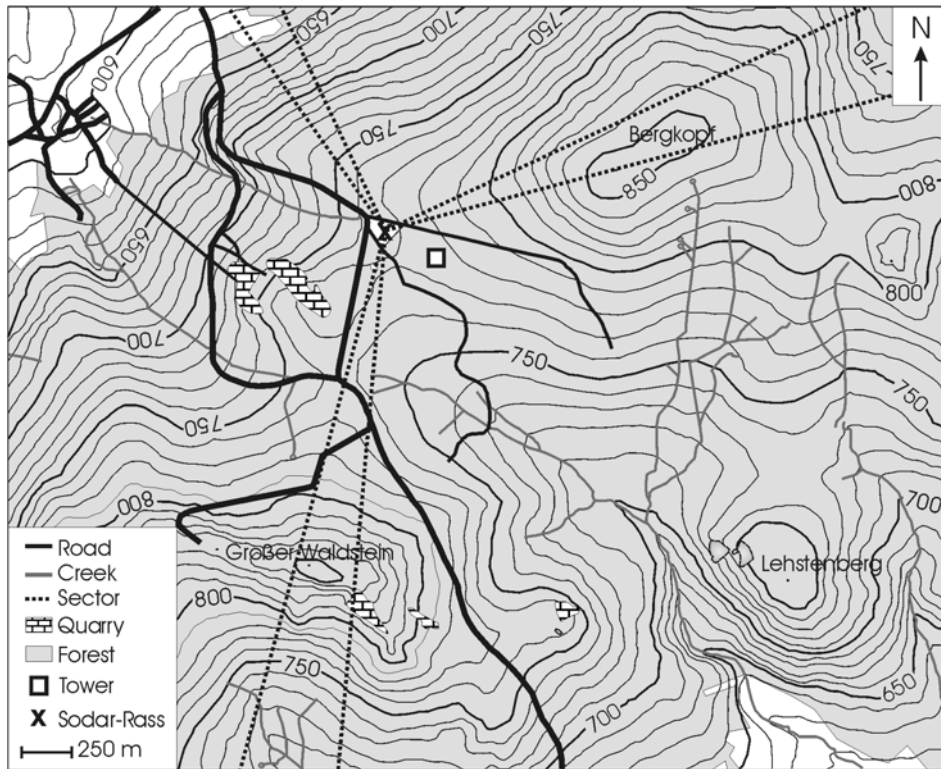


Figure 4: Map of the experimental site of WALDATEM-2003; numbers on isopleths are heights [m] a. s. l. The indicated sectors are main wind sectors, described in Subsection 4.2.1. Map adapted from: see Index of Maps, Map 1.

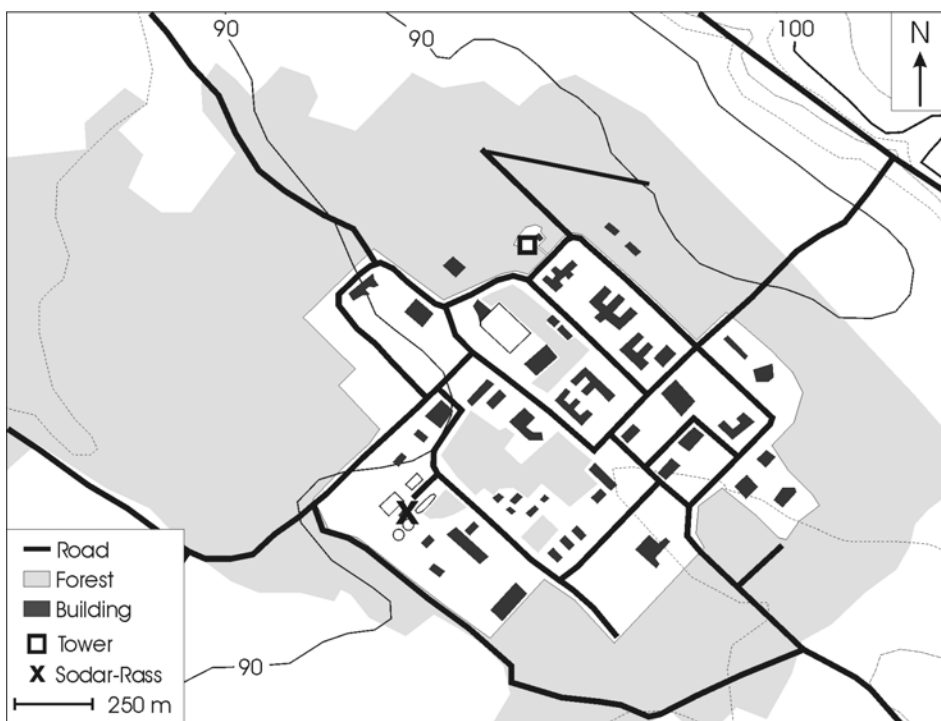


Figure 5: Map of the experimental site during ECHO 2003; numbers on isopleths are heights [m] a. s. l. Map adapted from: see Index of Maps, Map 2.

## **3.2 Acoustic sounding system**

This section presents the preparatory steps for SODAR measurements and for the data analysis. The first subsection describes the setup of the system. The next subsection shows the process of determining the sounding range at the specific location. The subsequent subsection deals with the important evaluation of disturbance due to noise or fixed echoes. In subsection four the determination of the noise height is described. The last subsection presents the results of the preparatory steps for the experiments WALDATEM-2003 and ECHO 2003.

### **3.2.1 Setup of the system**

The SODAR-RASS system was a DSDPA.90/64 combined with a 1290 MHz RASS extension (both Metek Meteorologische Messtechnik GmbH). The technical specifications can be found in Appendix A.

The SODAR-RASS-system consists of the following components:

- a phased array with 64 transceivers, surrounded from two sound absorbing shieldings, an inner and an outer shielding
- two parabolic dish RADAR antennas, located equidistantly on opposite side of the phased array
- the SODAR controls, consisting of the SODAR computer and a notebook.

After the phased array was mounted it was levelled exactly horizontally. The exact horizontal leveling is very important to assure a zero tilt of the vertical antenna A3 (see Figure 1 in Subsection 2.1.3). Before installing the inner and outer noise shielding, the sounding direction of antenna A1 was determined with a compass. This azimuth information is needed to calculate the wind direction (see Subsection 2.1.3). As a next step the acoustic shielding was mounted around the phased array. It is important to keep the same distance between the shielding and the transceivers on all sides of the phased array, to assure equal conditions for sound transmission and reception of the tilted beam directions. After the complete setup of the shielding, the system was fixed to the ground. The central power supply and the amplifiers for the transceivers were mounted on the outer noise shielding. The setup of the system was completed by the installations of the RADAR antennas at opposite sides of the SODAR. The RADAR dish antennas were leveled exactly horizontally.

An important parameter that needs to be adjusted is the so called cross-talk. It indicates the zero level of the received RADAR signal without sounding and should be around 0 dB. For

optimization purposes, slight corrections in the azimuth orientation or the leveling of the RADAR antennas were necessary. These corrections were done during the testing periods before starting the continuous measurements.

### 3.2.2 Determination of the height range

As Singal (1987) pointed out, the appropriate selection of the acoustic frequency is very important in the setup process of a SODAR system. During testing periods prior to the experiments, the SODAR-RASS system was operated at different acoustical frequencies to determine the optimal acoustical frequency for the soundings. For wind profile measurements and the observation of the development of the mixed layer, the sounding range should be as high as possible. As the absorption of sound waves increases non-linearly with increasing acoustic frequency (see Subsection 2.1.5), acoustical frequencies ranging from 1.0 kHz to 3.0 kHz were checked. An example for a set of five investigated frequencies is shown in Figure 6.

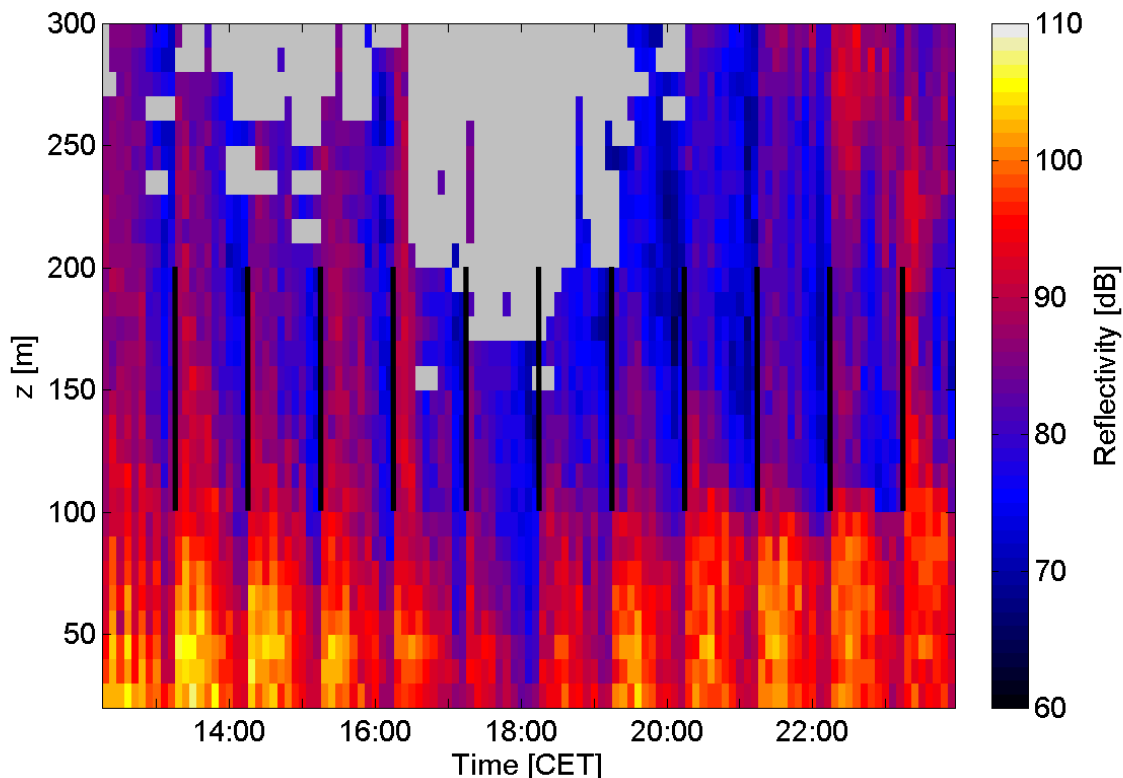


Figure 6: Sodargram of reflectivity for antenna A3 for May 5<sup>th</sup> 2003, 12:00 to 24:00 CET. The black lines indicate the beginning of a new scan through the investigated set of acoustical frequencies.

Each set starts with the lowest frequency, indicated with a black line, and continues to higher frequencies. The magnitude of reflectivity and the height of the uppermost gate clearly depends on the applied frequency as was described in Subsection 2.1.5. The set of acoustical frequencies which provided the required sounding range were passed onto further tests to optimize the sounding parameters.

### 3.2.3 Detection of fixed echoes

Fixed echoes can influence the data quality in a negative way and should be avoided whenever possible (see Crescenti, 1998). A fixed echo becomes evident as an increased reflectivity which persists on a certain height regardless of the meteorological condition. An example is shown in Figure 7. The selected range of acoustical frequencies was checked for the occurrence of fixed echoes. This examination has to be performed for each acoustical frequency long enough to comprise at least the different meteorological conditions of day and night. The influence of the different meteorological conditions is exemplarily shown in Figure 8. In a non-stably stratified ABL the reflectivity decreases with increasing height. Depending on the time of day and the acoustical frequency, the profiles in Figure 8 depart from this undisturbed profile.

From the tested acoustical frequencies with sufficient height range, the one with the lowest influence due to fixed echoes was chosen for the continuous measurements (see Table 2). For this selected acoustical frequency, the so called noise height has to be determined.

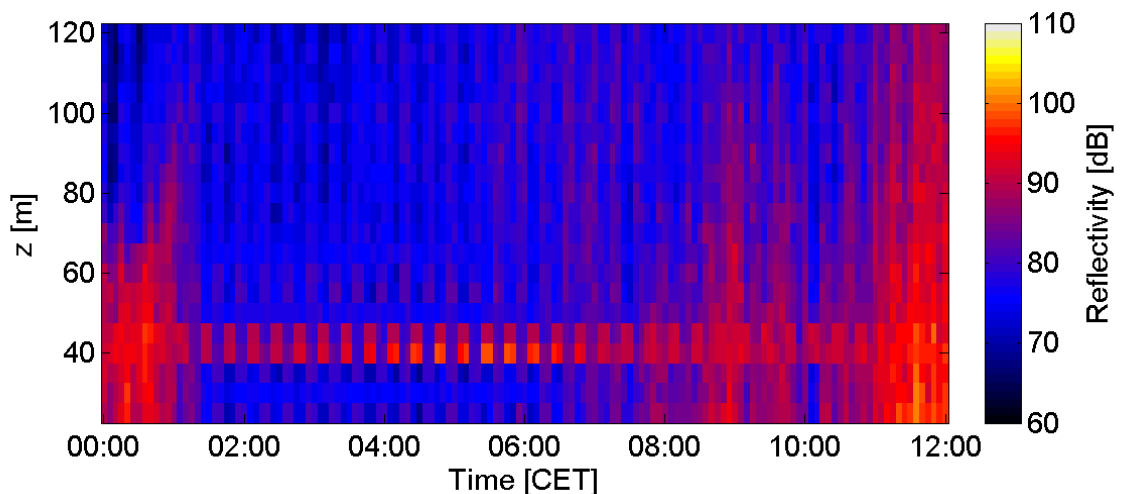


Figure 7: Sodargram of reflectivity for antenna A1 for May 10<sup>th</sup> 2003, 00:00 to 12:00 CET. At 40 m and 45 m the reflectivity is increased due to a fixed echo. The periodical change is caused by the application of two acoustical frequencies for the sounding.

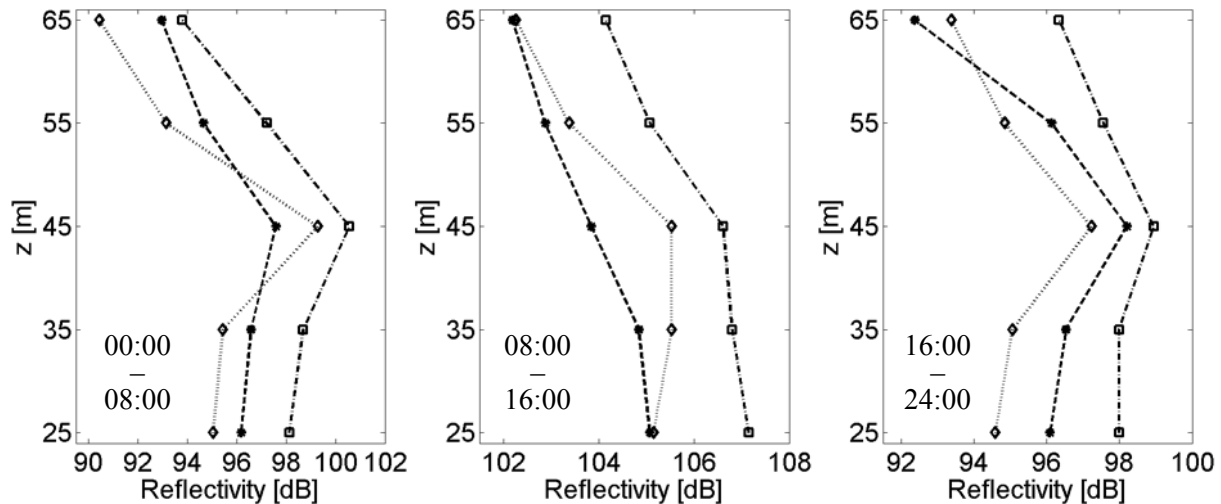


Figure 8: Assemble-averaged profiles of reflectivity for acoustic frequencies 1.6 kHz (dashed line), 1.65 kHz (dash-dot line) and 1.7 kHz (dotted line), antenna A1. Times are CET.

### 3.2.4 Determination of the noise height

The noise height indicates the height, from which no discernable backscattered signal can be received. For heights above the noise height, the SODAR will only receive the ambient noise. The noise height rules the repetition rate of the sounding pulses, because the time between two pulses must be long enough for the pulse to reach the noise height and to return to the antenna. Otherwise the backscattered preceding signal will disturb the next sounding. The noise height can be derived from the backscattered spectra by estimating the height where the peak around the emitted frequency vanishes. An example of the backscattered spectrum from three different heights is shown in Figure 9. For the 40 m gate, a sharp peak around filter 15 is visible. The backscattered spectrum from the 500 m gate shows only a slight peak at filter 16, and from the noise height at 1100 m no peak frequency can be found in the corresponding spectrum. The level of the spectrum from the noise height indicates the level of the ambient noise in the evaluated range of acoustical frequencies. The absence of a peak in the spectrum of the noise height confirms the right determination of this parameter.

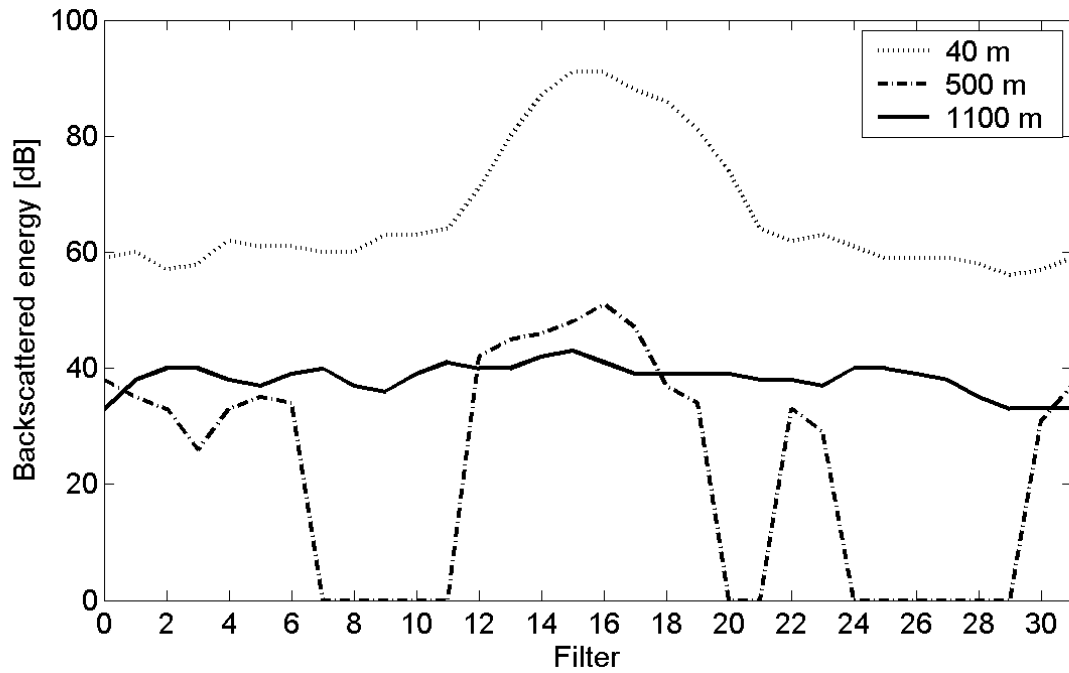


Figure 9: Spectra of the backscattered energy from three different heights for June 3<sup>rd</sup> 2003, 14:45 CET. The emitted acoustical frequency was 1.65 kHz.

### 3.2.5 Sounding parameters for the continuous measurements

From the tests described in the preceding subsections, the parameters listed in Table 2 were used for the continuous measurements.

Table 2: Sounding parameters for the continuous measurements during WALDATEM-2003 and ECHO 2003.

Parameter	WALDATEM-2003	ECHO 2003
Acoustical frequency [kHz]	1.65	1.6
Minimum height [m]	40	20
Maximum height [m]	980	700
Noise height [m]	1100	1000
Height resolution [m]	20	20
Distance of RADAR dish antennas [m]	6.50	6.12

The maximum height indicates the highest gate provided by the SODAR system. The maximum sounding range is much often smaller than the maximum height due to noise effects (see Subsection 2.1.5) and due to weak turbulence (see Subsection 2.1.1).

### 3.3 Data processing

Data from the SODAR-RASS system were obtained as five minute averages and as raw data from each antenna circulation. A circulation is a set of one sounding with each antenna, from which the wind velocity can be calculated (see Subsection 2.1.3). The data were processed using a set of programs developed for this study. As a first step, all data were filtered using the error code. This error code was provided by the system separately for every gate at every antenna. The error code includes flags for important properties of the backscattered spectra and signal-to-noise ratios. Only data with no limitation of the quality were passed onto the further analysis. The next step was the correction of the timestamps. Due to a slight drift of the system clock and due to randomly occurring delays in writing the data to the hard disc of the SODAR controls, the timestamps of the five minutes averages were not consequently equidistant. This deviations were corrected by assigning the next appropriate timestamp to the data or by rejecting the dataset for one time if the difference to the preceding and the following timestamp was too small. Then the gaps occurring in the profiles were filled by applying an interpolation (Akima, 1970) in space over a maximum gap of 100 m. Subsequently, the profiles were denoised, using a filter with 15 % influence of data beyond and 15 % of data below the individual height. As a last step, a temporal interpolation was performed over a maximum gap of ten minutes. This step was skipped for data which are depending on the used acoustical frequency, e.g. for the reflectivity. After this preparation process, 10 and 30 minutes averages were computed. The data processing scheme is shown in Figure 10.

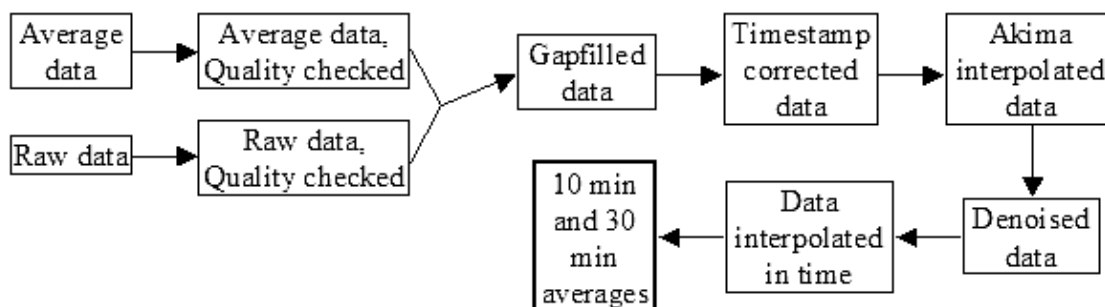


Figure 10: Data processing scheme of the SODAR-RASS data. Standard averaging time is five minutes, longer intervals are averages from five minute average data.

## 4. Results and discussion

This chapter presents the results of the SODAR-RASS measurements. In the following, all heights are geometrical heights  $z$  above ground level unless otherwise stated. Figures designated as a sodagram show a time-height cross section of a directly measured or derived parameter, where the x-axis is the time and the y-axis is the height.

The first section shows the results of the comparison of the SODAR measurements with tower measurements. The second section presents wind and temperature profiles, and the third part shows the development of the mixed layer.

### 4.1 Comparison with tower measurements

Comparisons with tower measurements were done during ECHO 2003 to attain a maximum of quality in the results. The technical specifications of the instruments at the tower can be found in Appendix B. Figure 11 shows the comparison of  $v_h$  in  $z = 50$  m and  $z = 120$  m. At both heights, assuming that the wind speed obtained by the cup anemometers is the “true” value, the SODAR system underestimates  $v_h$ . This effect is more pronounced at high values of  $v_h$  and in the lower gates. The equations for the linear regression and the coefficient of correlation  $R$  are given in Table 3.

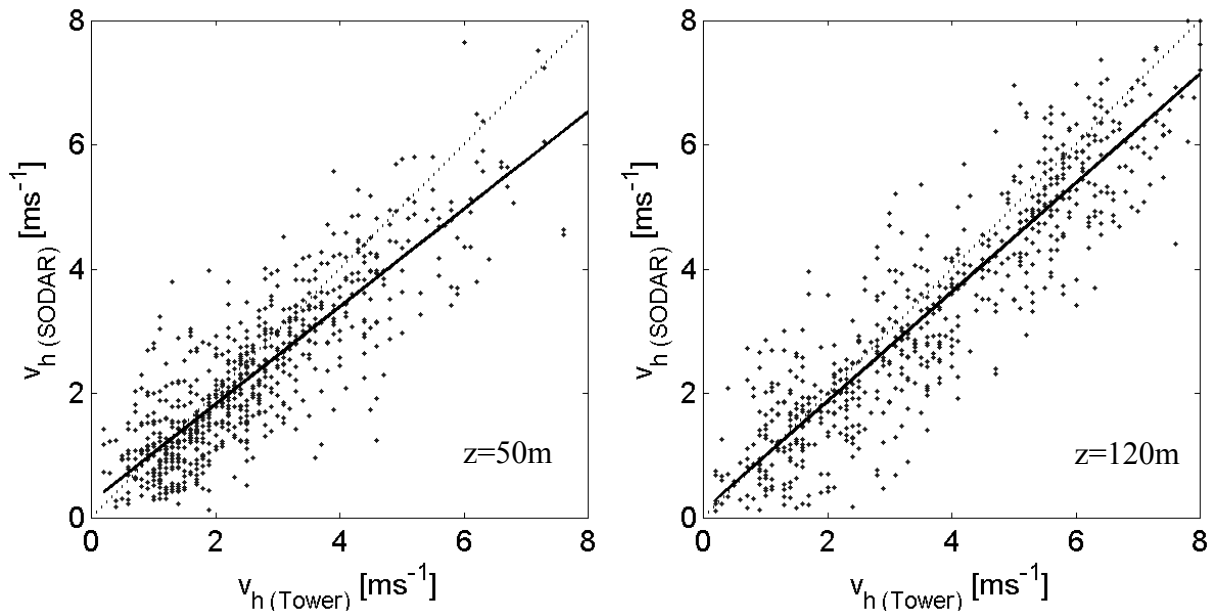


Figure 11: Comparison of the horizontal wind speed  $v_h$ , measured with cup anemometers and with the SODAR system for the entire ECHO 2003 dataset. The solid line indicates the linear regression.  $n = 765$  and  $655$ , respectively.

The measurements in  $z = 50$  m represent the part of the wind profile with the stronger gradient of  $v_h$  compared to  $z = 120$  m. This strong gradient is the result of the short distance to the canopy. The gates of the SODAR represent a cylindrical volume with an extension of 10 m above and below the indicated height, and with a diameter depending on the angle of beam broadening. The measured values thus are average values for the entire volume. In contrast, the cup anemometers of the tower are point measurements, providing exact values of  $v_h$  at the specified height. The mean value of a range within the exponential wind profile with high gradients of  $v_h$ , such as are common in the lower part of the wind profile, is less than the real point value at the middle of that range, which is measured by the cup anemometer. Therefore the SODAR underestimates  $v_h$  in the 50 m gate to a greater extent than it does in the 120 m gate and high values of  $v_h$  lead to a stronger underestimation than low values do. According to Keder et al. (1988), high wind speeds can also lead to an underestimation of  $v_h$  by the SODAR system due to increased levels of noise, causing a lower SNR. Due to the evaluation of the data quality by the SODAR computer, data with high values of  $v_h$  are rejected due to the reduced SNR, causing the average value to be too low. This effect was not found in the dataset used for the comparison between SODAR and tower measurements. Thus the underestimation of  $v_h$  by the SODAR system is only an effect of the volume averaging of the SODAR system.

The comparison of the acoustic temperature derived by the RASS system with the virtual temperature derived from the tower measurements is shown in Figure 12. As the virtual temperature is almost equal to the acoustic temperature (see Section 2.2) both parameters can be compared directly. A slight underestimation of the temperature by the RASS system is evident, the corresponding equation for the linear regression and the coefficient of correlation  $R$  are given in Table 3.

Table 3: Equation and coefficient of correlation  $R$  for the comparisons.

parameter	$z$ [m]	Experiment	Equation	$R$
$v_h$	50 m	ECHO 2003	$\text{SODAR} = 0.784 \cdot \text{TOWER} + 0.260$	0.85
$v_h$	120 m	ECHO 2003	$\text{SODAR} = 0.878 \cdot \text{TOWER} + 0.122$	0.91
$T_v$	120 m	ECHO 2003	$\text{RASS} = 0.931 \cdot \text{TOWER} + 1.101$	0.97

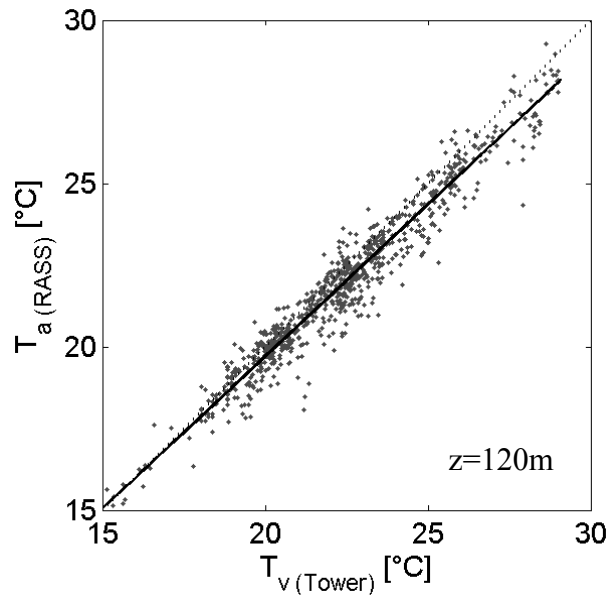


Figure 12: Comparison of the measurements of virtual temperature from a tower ( $z = 120$  m), and the acoustic temperature from the corresponding gate of the RASS system for the entire ECHO 2003 dataset. The solid line indicates the linear regression.  $n = 816$ .

## 4.2 Wind and temperature profiles

This section summarizes the results of wind profile measurements at the Waldstein site. The first subsection gives an overview of the general statistical characteristics of the wind and the mean wind profiles for the entire dataset. Single profiles and single events are presented in the following subsections. In the second subsection the influence of the topography on the wind profiles is discussed. In the subsequent subsection the characteristics of the observed low-level jets LLJ are described. In the last subsection, the occurrence of shear layers is presented.

### 4.2.1 General characteristics

During the experiment WALDATEM-2003, a total amount of 5841 wind profiles with a time resolution of 5 minutes were obtained. A distribution of the wind direction  $\varphi$  in  $z = 40$  m is shown in Figure 13, exhibiting three distinct maxima. From this distribution, three main sectors are derived visually (see Table 4). The sectors are chosen according to  $\varphi$  in a height of 40 m. The further evaluation of the data was done separately for these sectors.

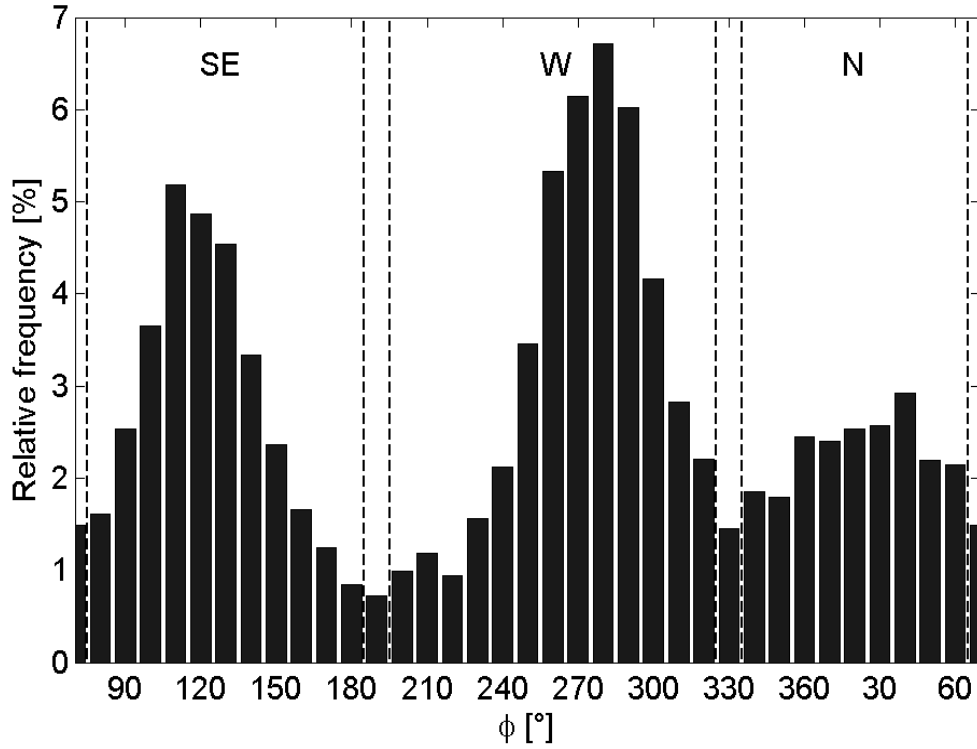


Figure 13: Distribution of relative frequency of the wind direction  $\phi$  in  $z = 40$  m for the entire WALDATEM-2003 dataset.  $n = 5841$ .

Table 4: Limits of the derived three main sectors for wind direction at the Waldstein site.

Sector	Lower limit [°]	Upper limit [°]
N	340	60
SE	80	180
W	200	320

The geostrophic wind defines the upper boundary condition of the wind profiles. The distribution of  $\phi$  in a height of 600 m is shown in Figure 14. The main direction of the geostrophic wind during the WALDATEM-2003 experiment was around  $290^\circ$ . 50 % of the measured geostrophic wind directions were found to lay within the range from  $260^\circ$  to  $320^\circ$ .

Mean wind profiles of each sector for the entire experimental dataset are shown in Figure 15. The profiles for each sector were selected by  $\phi$  in  $z = 40$  m. From these selected profiles the mean profile for each sector was calculated using a vector averaging of each height. Only profiles with available data up to at least 600 m were used.

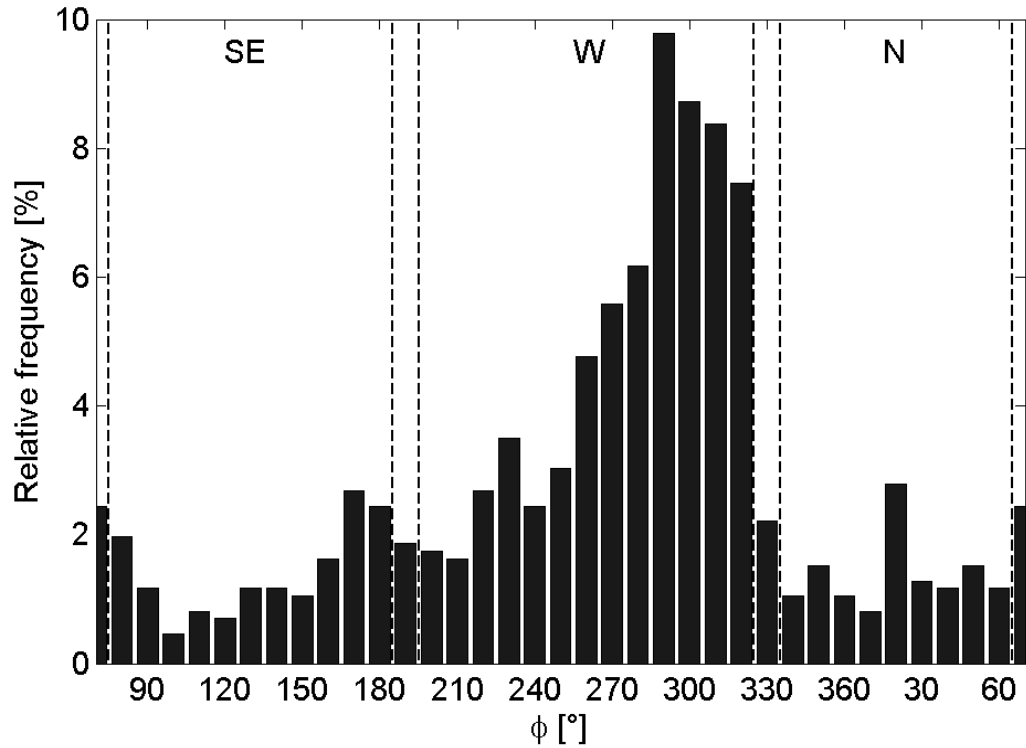


Figure 14: Distribution of relative frequency of geostrophic wind direction  $\phi$  in  $z = 600$  m for the entire WALDATEM-2003 dataset.  $n = 868$ .

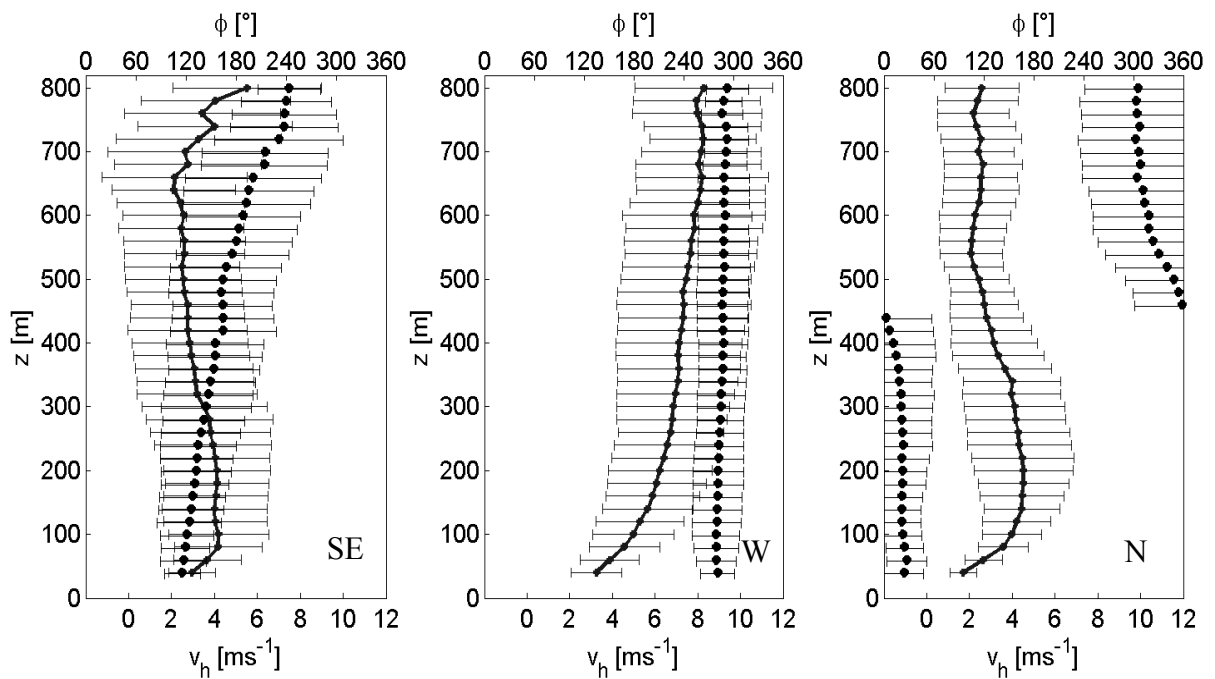


Figure 15: Mean profiles of the horizontal wind speed  $v_h$  (line) and wind direction  $\phi$  (dotted) for a near ground approaching flow from sectors southeast (246 profiles), west (296 profiles) and north (260 profiles), according to Table 4. Bars are standard deviations.

The three main sectors exhibit a different pattern in the mean profiles of  $v_h$  and  $\varphi$ . The SE sector shows a clockwise turn of  $\varphi$  with increasing height of about  $90^\circ$  between 40 m and 600 m. A maximum of  $v_h$  is found between 80 m and 280 m with a minimum at 500 m. The turn of the wind complies with the Ekman spiral (see Section 2.3) only in its direction. The magnitude of approx.  $90^\circ$  is much more than the expected value of approx.  $30^\circ$ . This increased turn is forced by the topography. In the SW of the experimental site, in a distance of approx. 1.5 km, the mountain “Großer Waldstein” acts as an obstacle for the wind field. While the flow in higher altitudes keeps its initial direction, the wind near the ground is forced to flow around the mountain. This deflection causes the wind near the ground to approach the experimental site from directions around SE. The maximum of  $v_h$  found between 80 m and 280 m is the result of a canalising effect. A valley, striking NW-SE and starting at the experimental site, forces the deflected streamlines of the wind field towards the experimental site. This leads to compressed streamlines in the lower altitudes, resulting in an increased wind speed. Similar altitudes of a wind maximum due to a speed up at a mountain ridge were found by Svoboda and Cermak (2002). In the W sector  $\varphi$  turns about  $30^\circ$  clockwise with increasing height, following the Ekman spiral (see Section 2.3). The profile of  $v_h$  shows an exponential increase of  $v_h$  with increasing height. The N sector is characterised by a strong maximum of  $v_h$  in the lowest 400 m. Within these 400 m no noticeable turn of  $\varphi$  can be found. In greater altitudes the wind strongly turns counter-clockwise up to directions around  $300^\circ$  while  $v_h$  remains low. As there are no topographic obstacles in the N sector explaining this disturbance of the wind profile, the impact of the atmospheric stability on the wind profiles is investigated.

#### 4.2.2 Profile dependence on stability parameter $\zeta$ and geostrophic conditions

A common measure for the atmospheric stability is the dimensionless stability parameter  $\zeta$ . It is defined as the measuring height  $z$  divided by the Obukhov length  $L_0$  (Obukhov, 1946), determined in the surface layer.  $L_0$  is defined as

$$L_0 = - \frac{u_{*0}^3}{\kappa \frac{g}{T} \frac{Q_{H0}}{\rho c_p}}, \quad (16)$$

where  $c_p$  is the specific heat at constant pressure for moist air,  $g$  is the acceleration due to gravity,  $\kappa$  is the von-Kármán constant (0.4),  $Q_{H0}$  is the sensible heat flux near the surface,  $\rho$  denotes the mass density of air and  $u_{*0}$  indicates the friction velocity near the surface.  $L_0$  is determined at  $z = 33$  m in the surface layer and is assumed to be valid for the entire ABL. Thus further values of  $\zeta$  are measures of the stability within the surface layer.

The magnitude  $|L|$  is proportional to the thickness of the layer in which shear and friction are important.  $L$  has positive values for stable conditions and negative values for unstable conditions. The values of  $L$  are derived from an ultrasonic anemometer mounted at a tower nearby. As the displacement height  $d$ , which is  $\frac{2}{3}$  of the canopy height, has to be considered in the determination of  $\zeta$ , the height of measurement enters as the aerodynamically height ( $z - d$ ). Thus further values of  $\zeta$  were calculated using Eq. ( 17 ).

$$\zeta = \frac{z - d}{L_0} \quad (17)$$

Several definitions of stability classes exist in literature. The stability classes for  $\zeta$  and the terms used in this study are listed in Table 5. The boundaries of neutrality were chosen according to Foken and Skeib (1983).

Table 5: Classes of the stability parameter  $\zeta$ , used terms and the number of profiles (30 minutes averages) in each sector found for this class for the WAL-DATEM-2003 data.

Term	$\zeta$	SE sector	W sector	N sector
stable	$0.2 \leq \zeta < 1$	29	1	10
near neutral	$-0.3 \leq \zeta < 0.2$	38	98	53
neutral	$-0.0625 < \zeta < 0.125$	27	67	35
unstable	$-1 < \zeta < -0.3$	19	6	19
stable range	$1 > \zeta > 0$	58	43	46
unstable range	$-1 < \zeta < 0$	28	59	36

The wind profiles of the W sector for the atmospheric stability within the stable and the unstable range are shown in Figure 16. The mean profile within the stable range shows a strong and exponential increase of  $v_h$  with increasing height from  $3 \text{ ms}^{-1}$  to  $10 \text{ ms}^{-1}$ , while  $\phi$  turns around  $30^\circ$ .

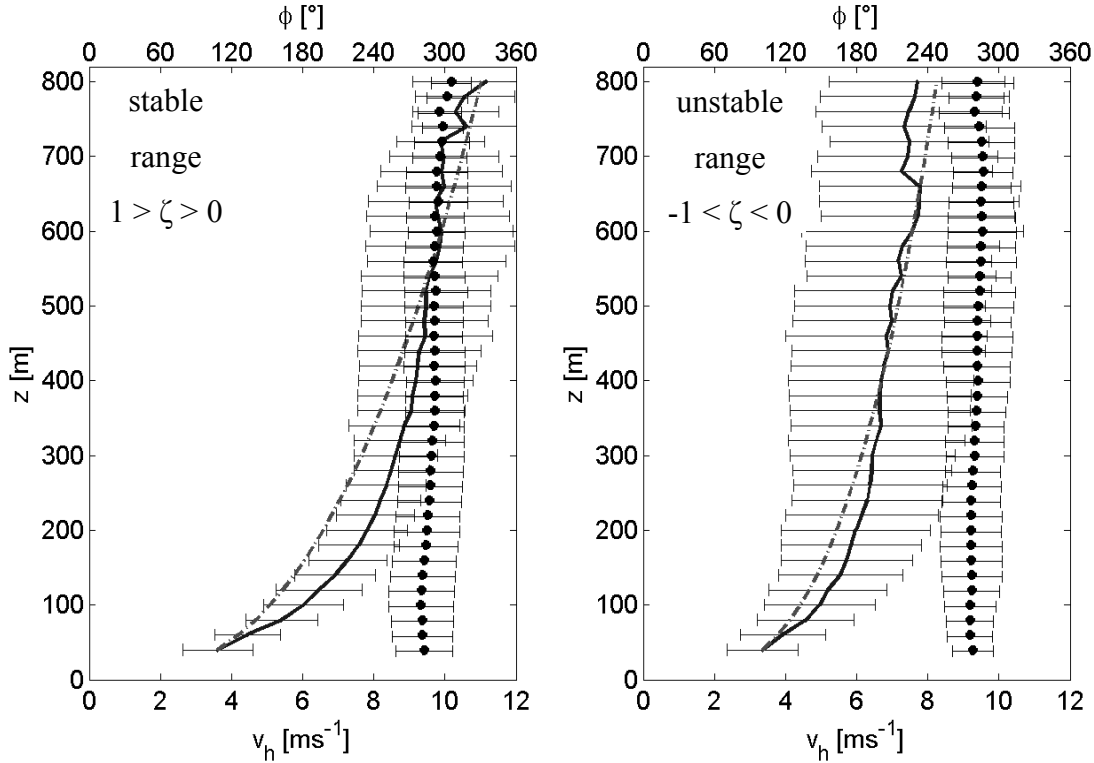


Figure 16: Mean profiles of the horizontal wind speed  $v_h$  (line) and wind direction  $\phi$  (dotted) for the W sector, for the entire WALDATEM-2003 dataset. Bars are standard deviations. The dash-dotted line shows a calculated profile, based on the power law.

For the unstable range, the profile shows an increase of  $v_h$  with increasing height from  $3 \text{ ms}^{-1}$  to almost  $8 \text{ ms}^{-1}$ , while  $\phi$  remains fairly constant over the entire profile. The increase of  $v_h$  with increasing height at unstable conditions is less than at stable conditions, as for unstable conditions the influence of the frictional drag is stronger. The change in  $\phi$  is almost absent under unstable conditions because of the tight coupling of the ground and the ABL as far as it could be investigated in this work. Most of the profiles are found to occur under neutral or near neutral conditions (see Table 5). To compare the mean profile of  $v_h$  with profiles based on the power law (see Section 2.3), profiles of  $v_h$  were calculated using Eq. ( 13 ). The power law exponent  $p$  was determined by using  $v_h$  in  $z = 40 \text{ m}$  and  $z = 600 \text{ m}$ . For the profile of  $v_h$  within the stable range,  $p$  is 0.37, within the unstable range it is 0.30. The power law profiles are shown in Figure 16 together with the mean profiles. The power law profiles overestimate  $v_h$  in the lower part of the profile, but underestimate  $v_h$  above  $z = 600 \text{ m}$ . The crossing from over- to underestimation in  $z = 600 \text{ m}$  is a result from the determination of  $p$ . Nevertheless, the power law profiles do not fit the real mean profile of  $v_h$ .

Wind profiles under different stability conditions for the SE sector are shown in Figure 17. Profiles within the stable range show a strong turn of  $\phi$ . A distinct secondary maximum of  $v_h$

can be observed in  $z = 80$  m. Above this height  $v_h$  decreases up to an altitude of 500 m. For greater altitudes  $v_h$  increases again. Under unstable conditions almost no turn in  $\phi$  can be found up to an altitude of 600 m. A lack of data at heights above 600 m leads to high variations of  $\phi$  and thus makes it impossible to derive reliable results. The profile of  $v_h$  shows a broad maximum, reaching from  $z = 140$  m up to  $z = 500$  m. Above  $z = 500$  m,  $v_h$  decreases. As the number of data points strongly decreases above 600 m, the profile should not be interpreted beyond this altitude. Profiles based on the power law were not calculated, as the power law can not account for a decline of  $v_h$  with increasing height above a maximum of  $v_h$ . Thus the power law is not suitable for profiles within the SE sector. The different shapes of the profiles show a strong dependency of the wind profiles on  $\zeta$  within the SE sector. The influence of the topography is generally most important under stable conditions, because under stable conditions the wind flow occurs in layers which follow the underlying surface. The strong turn in  $\phi$  and the distinct secondary maximum of  $v_h$  near the ground was only observed for conditions within the stable range.

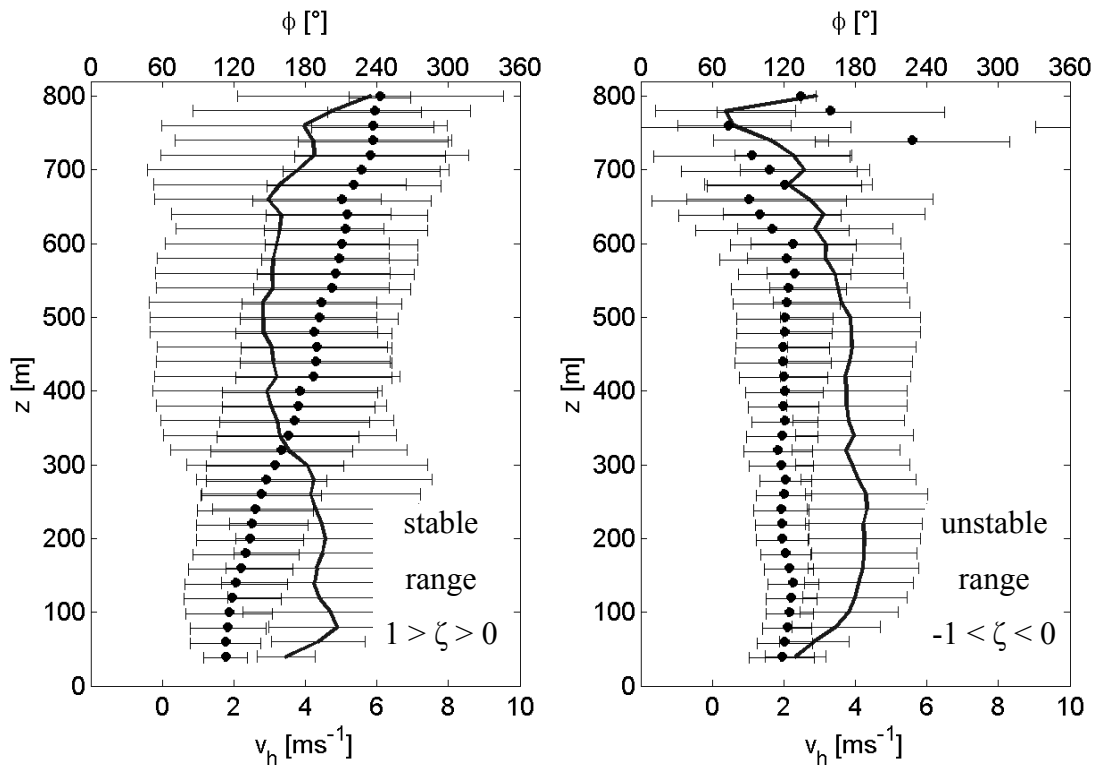


Figure 17: Mean profiles of the horizontal wind speed  $v_h$  (line) and wind direction  $\phi$  (dotted) for the SE sector, for the entire WALDATEM-2003 dataset. Bars are standard deviations.

These findings support the supposed deflection by the mountain “Großer Waldstein” and the canalising effect. Under stable conditions, the value of  $\varphi$  at the upper end of the profile for the SE sector (250 °) are very close to that for the W sector (300 °). For a geostrophic wind direction within these two boundaries, the change of  $\varphi$  near the ground from the SE sector to the W sector and vice versa must take place. Figure 18 shows the dependency of  $\varphi$  in  $z = 40$  m on  $\varphi$  in  $z = 400$  m for profiles within the stable range. The gate in  $z = 400$  m was chosen as a compromise between a great altitude and a high number of data, as the number of data points strongly decreases for higher gates. Within the W sector, the wind direction near the ground follows that in  $z = 400$  m with a small offset. In the SE sector,  $\varphi$  near the ground does not depend on  $\varphi$  in  $z = 400$  m. Regardless of a varying geostrophic wind direction between 100 ° and 240 °,  $\varphi$  in  $z = 40$  m remains at values around 120 °. For values of the geostrophic wind direction greater than 240 °,  $\varphi$  near the ground was found to lay within the W sector. The transition between the SE sector and the W sector, under conditions of the atmospheric stability within the stable range, takes place at a geostrophic wind direction around 240 °. The atmospheric stability is an important parameter for the wind profiles in the SE sector. In the stable range of the atmospheric stability the wind profile departs from an exponential shape for  $v_h$  and an approx. 30 ° clockwise turn with increasing height for  $\varphi$ .

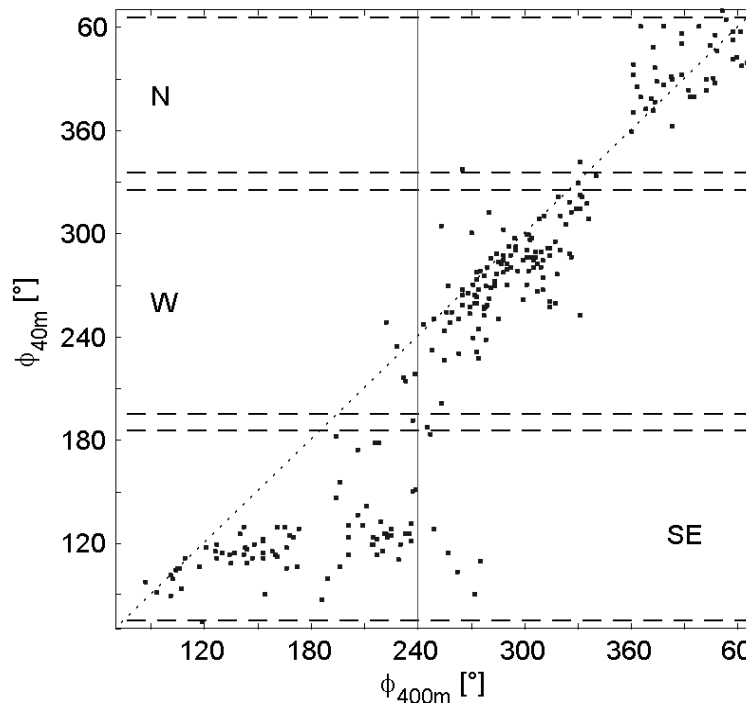


Figure 18: Scatter plot of wind directions  $\varphi$  in 40 m and 400 m for  $\zeta > 0$  (stable range) with the three main sectors indicated by dashed lines. Around 240 ° in 400 m a sudden jump from the west to the south-east sector can be observed, indicated by the vertical line.

Thus for wind from the SE sector it is not possible to infer the wind vector in greater altitudes from the wind near the ground under stable conditions.

Mean wind profiles from the N sector for two different conditions of the atmospheric stability are shown in Figure 19. The maximum of  $v_h$  is most pronounced in profiles within the stable range of  $\zeta$ , while for the unstable range the profiles have only a slight secondary maximum of  $v_h$ . Under stable conditions a slight clockwise turn of  $\phi$  with increasing height was found within the layer of the increased wind speed, reaching up to  $z = 500$  m. Beyond that layer, the wind turns counter-clockwise with increasing height. For the unstable range, the profile of  $\phi$  does not show a turn within the lowest 300 m but in greater altitudes it turns counter-clockwise with increasing height. Although the atmospheric stability has a noticeable effect on the shape of the wind profiles within the N sector, the profiles depart under every stability condition from the exponential shape for  $v_h$  and the Ekman turn of  $\phi$ . Profiles based on the power law were not calculated, as the power law can not account for a decline of  $v_h$  with increasing height above a maximum of  $v_h$ . Thus the power law is not suitable for profiles within the N sector.

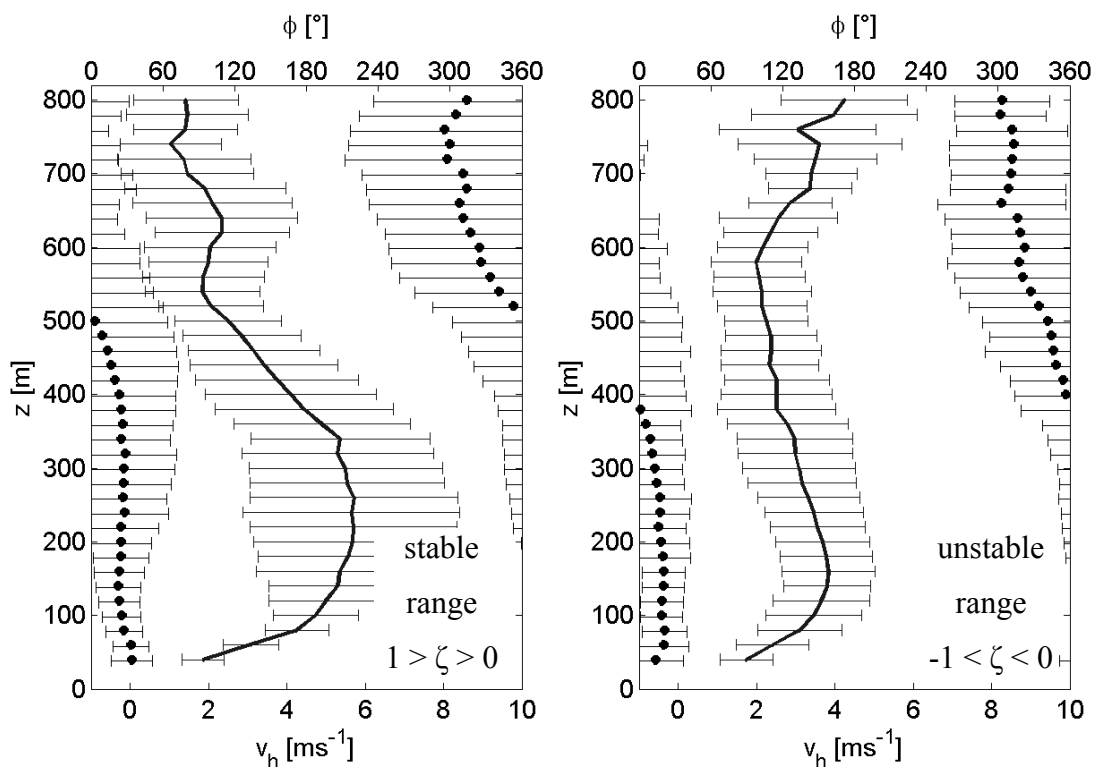


Figure 19: Mean profiles of the horizontal wind speed  $v_h$  (line) and wind direction  $\phi$  (dotted) for the N sector, for the entire WALDATEM-2003 dataset. Bars are standard deviations.

For a wind near the ground from the N sector, the inference of the wind vector in greater altitudes is impossible under every atmospheric stability.

Besides  $v_h$  and  $\phi$ , other wind components show noticeable effects, e.g. the mean vertical wind velocity  $\bar{w}$ . Over flat terrain,  $\bar{w}$  should equal zero. In complex terrain, the stream lines of the wind field are forced upward and downward, resulting in values of  $\bar{w}$  different from zero. Figure 20 shows the dependency of  $\bar{w}$  on  $\phi$ . The W sector shows positive values of  $\bar{w}$ , in the SE sector prevailing negative values of  $\bar{w}$  are found and the N sector is characterised by slightly negative values of  $\bar{w}$ . As the site is located on a saddle, the inflexion of the streamlines is strongly dependent on  $\phi$ . In case of wind from the W sector, the wind field is inflected upward as it follows the rise of the Fichtelgebirge. The SE sector shows a contradictory result. With respect to the valley of the Lehstenbach, the SODAR system is located slightly on the backward side of the saddle, where the wind field is already directed downward, following the slope of the Fichtelgebirge. The values observed for the N sector are caused by the shallow summit Bergkopf (see map in Figure 4), which is located at the eastern boundary of the N sector in  $60^\circ$  direction. The wind flow over the Bergkopf leads to the negative values of  $\bar{w}$  in the N sector.

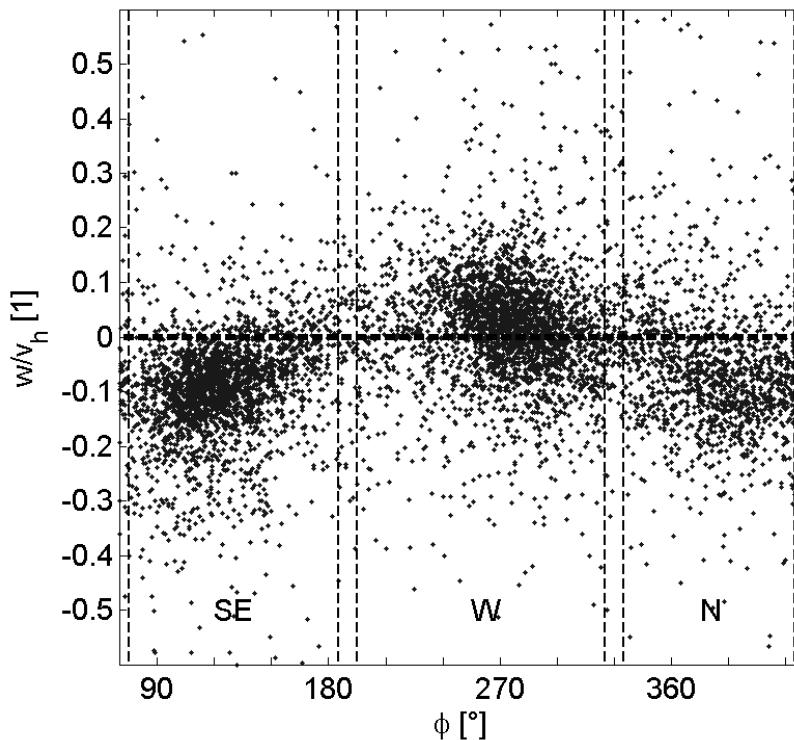


Figure 20: Dependency of the mean vertical wind speed  $\bar{w}$  normalised with the horizontal wind speed  $v_h$  on the wind direction  $\phi$  in  $z = 40$  m for the entire WALDATEM-2003 dataset. A total of 6985 values are displayed.

Comparable but somehow different dependencies of  $\bar{w}$  on  $\varphi$  were reported by Göckede et al. (2004). Using ultrasonic anemometers, they found  $\bar{w}$  equals zero along an axis from ESE to WNW, while Figure 20 shows a zero line crossing around S and NNW. This deviation is mainly caused by the different measuring systems. As the values obtained by the SODAR system are volume averaged values, they can not be directly compared to the point measurements from the ultrasonic anemometer. Furthermore, measurements of  $\bar{w}$  with an ultrasonic anemometer are subject to critical corrections for a tilt of the instrument and flow distortions by the anemometer. The SODAR system does not disturb the flow while measuring and its tilt was determined to equal zero prior to the experiment. The strong dependency of  $\bar{w}$  on  $\varphi$  found in this study and by Göckede et al. (2004) suggests, that for calculations which need data with  $\bar{w}$  equals zero, e.g. the calculation of fluxes, corrections must be done dynamically in such a complex terrain, depending on the current values of  $\varphi$  and  $v_h$ .

### 4.2.3 Topographic effects on single profiles

The influence of the topography on single wind profiles is demonstrated in this subsection. Mean effects of the topography are discussed in Subsection 4.2.1. Figure 21 shows a sodar-gram of  $\varphi$  from June 5<sup>th</sup> to 6<sup>th</sup> 2003. It shows a strong variability of the wind directions. An abrupt change of  $\varphi$  near the ground from the SE sector to the W sector is visible at 17:30 and 00:30 CET. In both cases, the position of the abrupt change of  $\varphi$  is indicated in Figure 21 with a solid line. In greater altitudes, a continuous transition between the two sectors can be found, indicated by dotted lines. Both events are indicated with “A”. As described in Subsection 4.2.1, the abrupt change of  $\varphi$  near the ground is caused by the summit “Großer Waldstein”, deflecting the stream lines of the wind field, and by the “Lehstenbach” valley, canalising the wind field. In contrast to the mean effects in Subsection 4.2.1, Figure 21 shows a time series of single profiles. As the abrupt change of  $\varphi$  near the ground can be found at both transitions of  $\varphi$  from the SE sector to the W sector in Figure 21, the influence of the topography does not only affect the mean wind profiles but is also present in the short time averaged wind profiles. A transit from the N sector to the SE sector is indicated with a “B”. At the moment of the transit, the wind is forced to blow over the top of the shallow summit “Bergkopf” (see map in Figure 4). Figure 22 shows the corresponding sodargram of reflectivity. At the downstream side of the “Bergkopf” the flow becomes turbulent, causing strong temperature fluctuations.

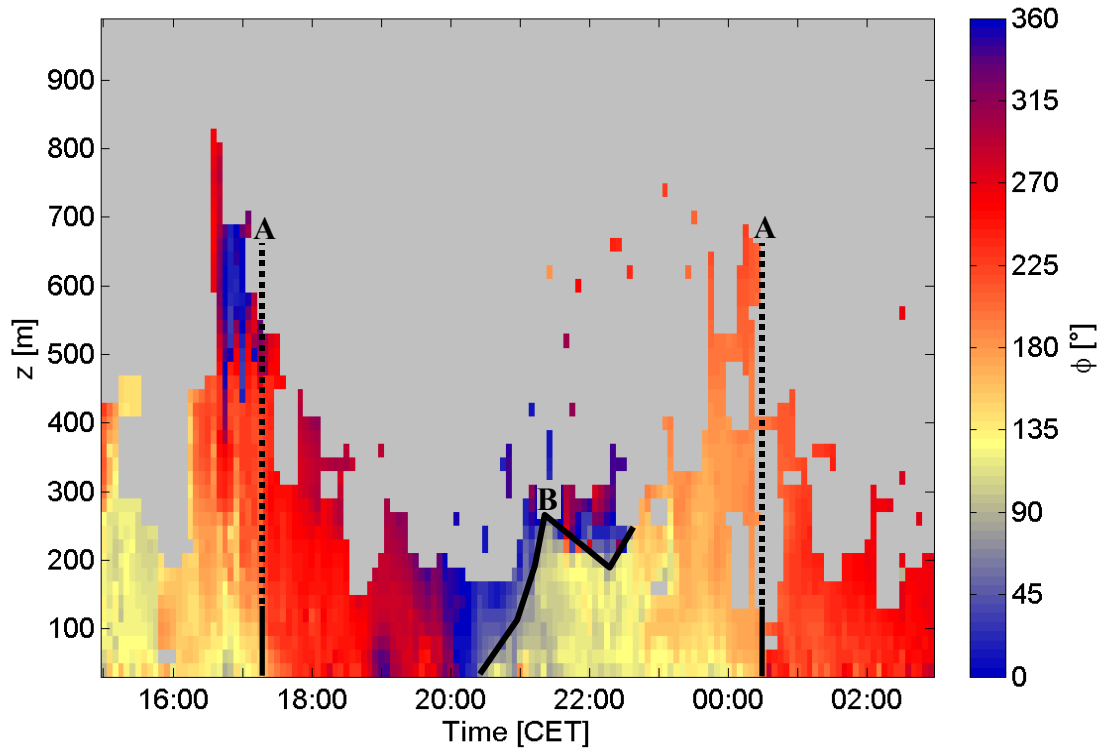


Figure 21: Sodargram of the wind direction  $\phi$  from June 5<sup>th</sup> to 6<sup>th</sup> 2003. Effects mentioned in the text are marked with black lines.

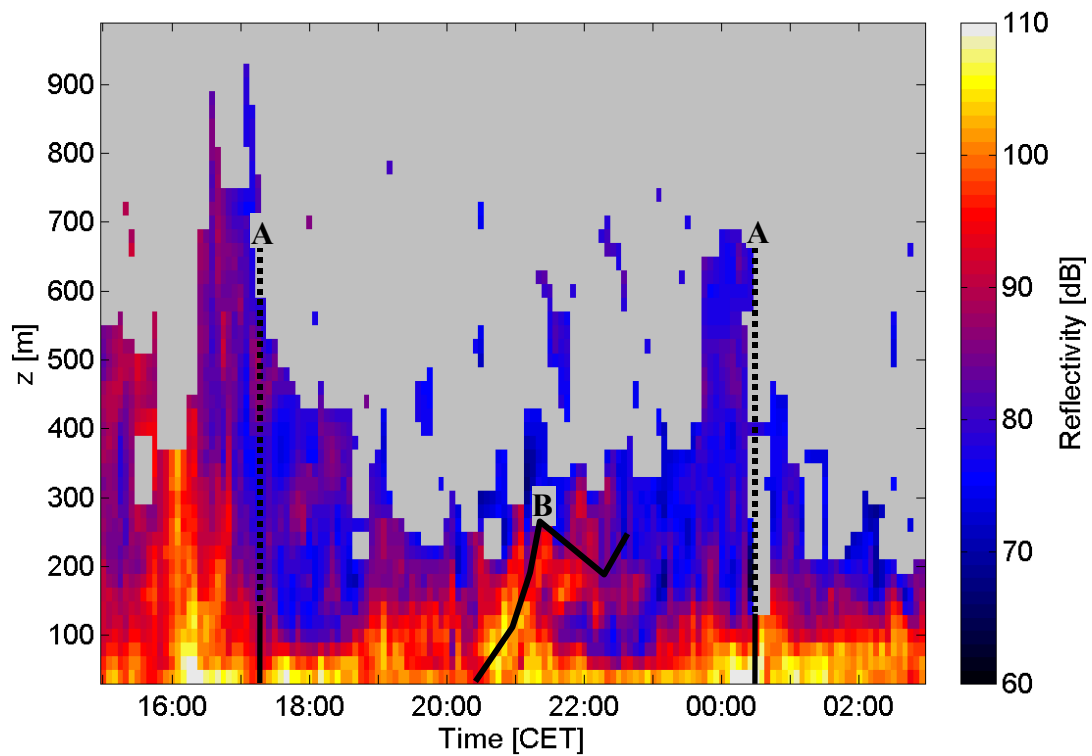


Figure 22: Sodargram of reflectivity June 5<sup>th</sup> to 6<sup>th</sup> 2003. Effects mentioned in the text are marked with black lines.

These fluctuations are advected towards the experimental, resulting in a region of increased reflectivity up to an altitude of 300 m (“B” in Figure 22).

#### 4.2.4 Low-Level Jets

Low-level jets have been observed during the WALDATEM-2003 experiment. Three events with a duration time of more than one hour are presented in this subsection. All of them are characterised by an approaching flow near the ground from the N sector. The basic characteristics of the observed LLJ events can be seen in Table 6.

Table 6: Observed LLJ events and their characteristics. The temperature gradient is a mean value for the entire LLJ event.

Date	Duration [h]	$v_{h \max}$ [ms <sup>-1</sup> ]	$z(v_{h \max})$ [m]	Time ( $v_{h \max}$ ) [CET]	$\Delta T/\Delta z$ [Km <sup>-1</sup> 10 <sup>-2</sup> ]
10 <sup>th</sup> to 11 <sup>th</sup> June	1	8	100	00:15	+1.32
14 <sup>th</sup> to 15 <sup>th</sup> June	10	12	300	02:00	-0.35
6 <sup>th</sup> to 7 <sup>th</sup> July	7	11	approx. 250	00:45	+0.08

The first LLJ event is shown in Figure 23. The horizontal wind speed reaches its maximum value ( $v_{h \max}$ ) of 8 ms<sup>-1</sup> shortly after midnight, while the wind speed above dropped to almost 0 ms<sup>-1</sup>. The entire event lasts only about one hour. It meets several of the criteria for LLJ introduced in Section 2.5. Later in that night, a wind speed profile with a monotone increase of  $v_h$  with increasing height develops, where no secondary maximum is observable. Figure 24 shows the corresponding sodargram of  $\varphi$ . Near the ground,  $\varphi$  turns from the southwest through the SE sector into the N sector. After 01:00 CET the wind near the ground turns slowly back through the SE sector to directions from southwest. In greater altitudes, the wind was found to remain within the W sector. The LLJ occur while the wind comes from the N sector. The maximum intensity of the LLJ was observed when the layer with wind from the N sector has its biggest extent. The onset of the wind flow from the N sector is associated with a noticeable decrease of temperature (Figure 25). This decrease is caused by a cold air mass advected from the north. As it underlies the warmer residual air mass at the site, the temperature gradient  $\Delta T/\Delta z$  changes from -0.16 Km<sup>-1</sup>10<sup>-2</sup> to +1.32 Km<sup>-1</sup>10<sup>-2</sup>, indicating a strong statically stable atmosphere. This stable stratification leads to the increase of  $v_h$  due to the decreased frictional drag.

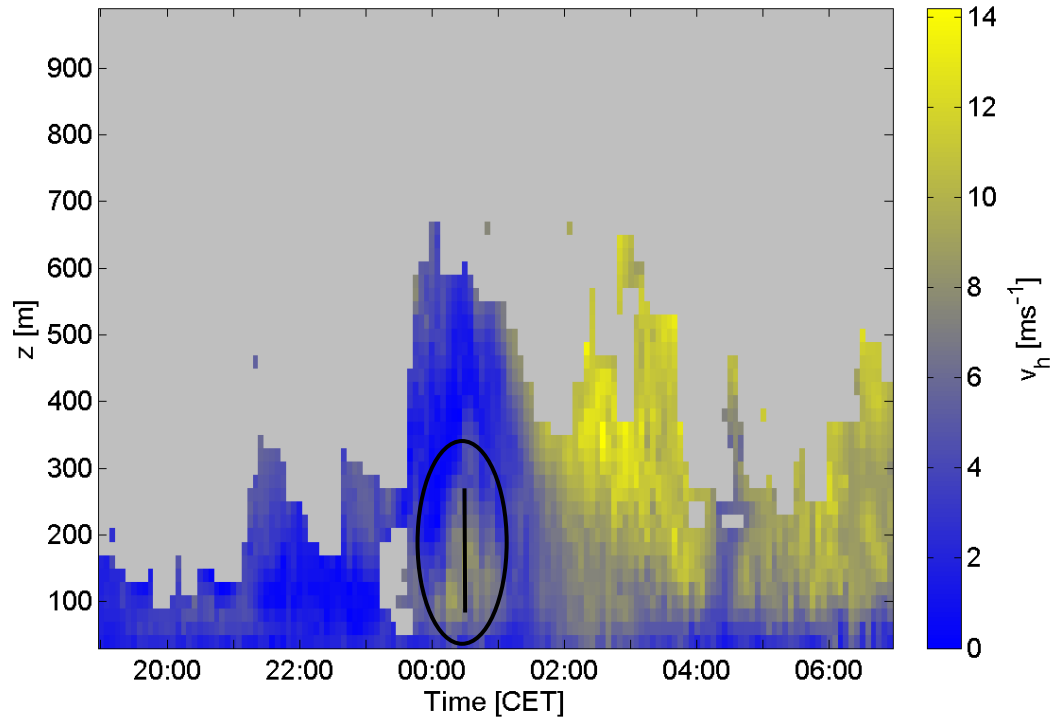


Figure 23: Sodargram of the horizontal wind speed  $v_h$  from 10<sup>th</sup> to 11<sup>th</sup> June 2003. The LLJ is marked with the circle, the black line indicates the time of the maximum intensity of the LLJ.

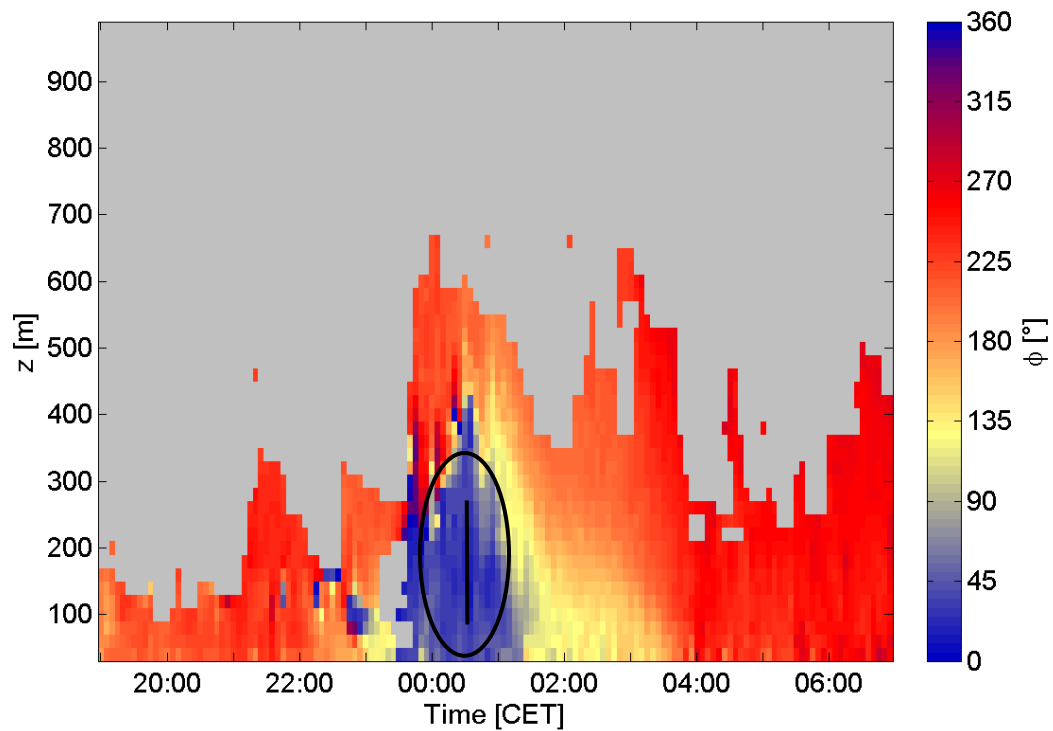


Figure 24: Sodargram of the wind direction  $\phi$  from 10<sup>th</sup> to 11<sup>th</sup> June 2003. The region of the LLJ in Figure 23 is marked with the circle, the black line indicates the time of the maximum intensity of the LLJ in Figure 23.

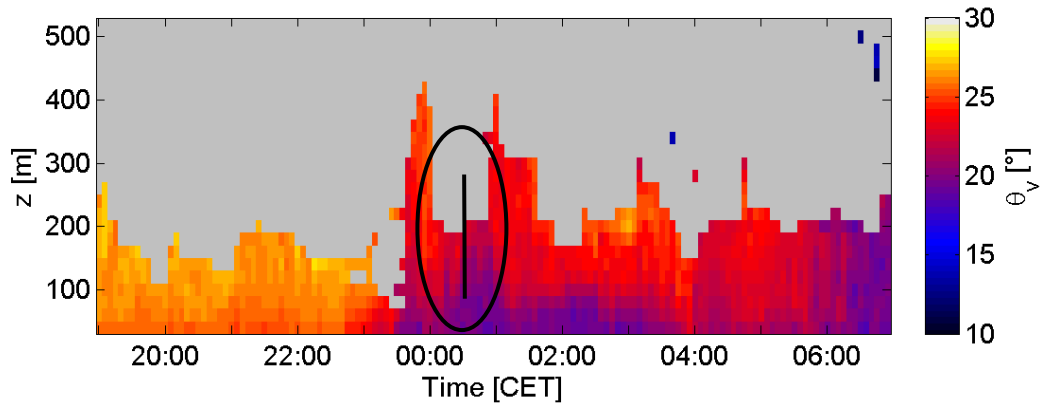


Figure 25: Sodagram of the potential temperature  $\theta$  from June 10<sup>th</sup> to 11<sup>th</sup> 2003. The region of the LLJ in Figure 23 is marked with the circle, the black line indicates the time of the maximum intensity of the LLJ in Figure 23.

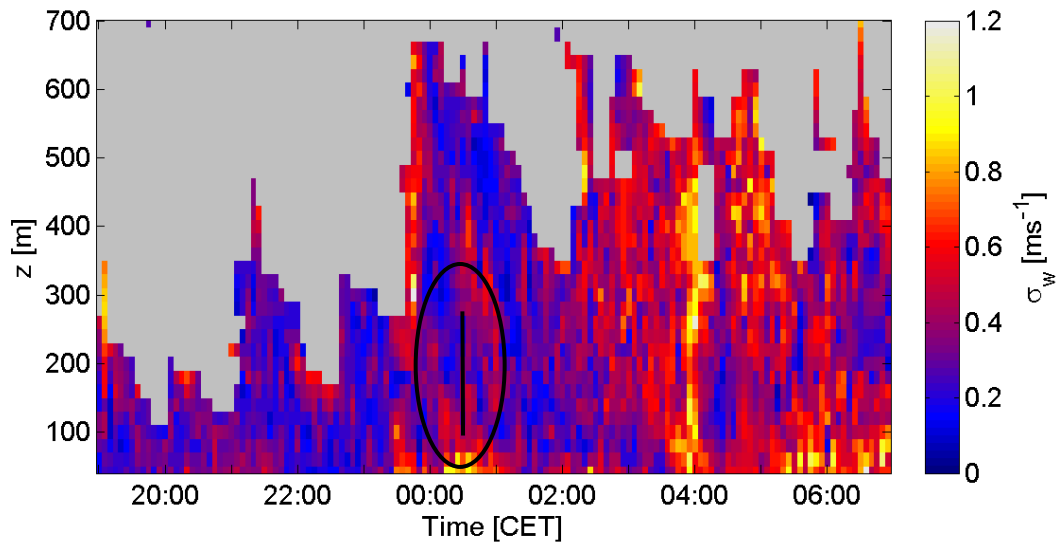


Figure 26: Sodagram of the standard deviation of the vertical wind velocity  $\sigma_w$  from June 10<sup>th</sup> to 11<sup>th</sup> 2003. The region of the LLJ in Figure 23 is marked with the circle, the black line indicates the time of the maximum intensity of the LLJ in Figure 23.

In Figure 26, a region of enhanced turbulence near the ground can be seen shortly after midnight, reaching values of  $\sigma_w$  around  $0.9 \text{ ms}^{-1}$ . The time of the occurrence of this high values of  $\sigma_w$  coincides well to the time of the maximum intensity of the LLJ. It is caused by the strong shear of  $v_h$  between the surface and the LLJ. Similar results were reported by Reitebuch et al. (2000).

The sodagram of  $v_h$  for the second LLJ event in the night from June 14<sup>th</sup> to 15<sup>th</sup> 2003 is shown in Figure 27. Its duration is around 10 hours, which is much longer than that of the first event.  $V_{h \max}$  is reached shortly after midnight with values up to  $12 \text{ ms}^{-1}$ .

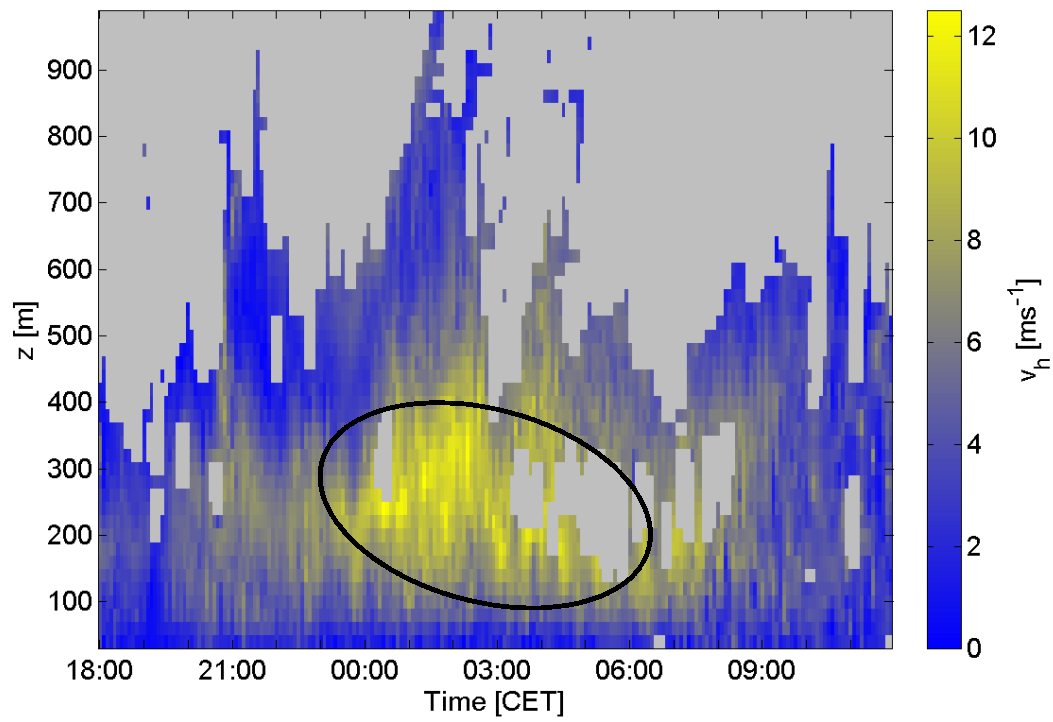


Figure 27: Sodargram of the horizontal wind speed  $v_h$  from 14<sup>th</sup> to 15<sup>th</sup> June 2003. The region of the LLJ is marked.

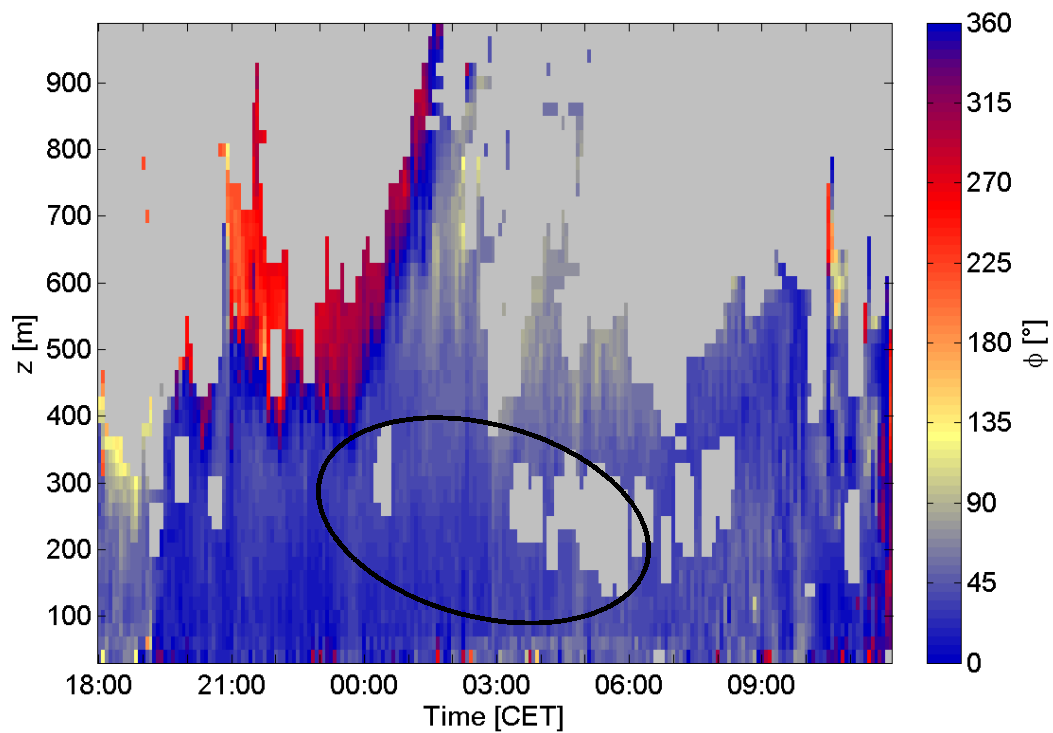


Figure 28: Sodargram of the wind direction  $\phi$  from June 14<sup>th</sup> to 15<sup>th</sup> 2003. The region of the LLJ shown in Figure 27 is indicated.

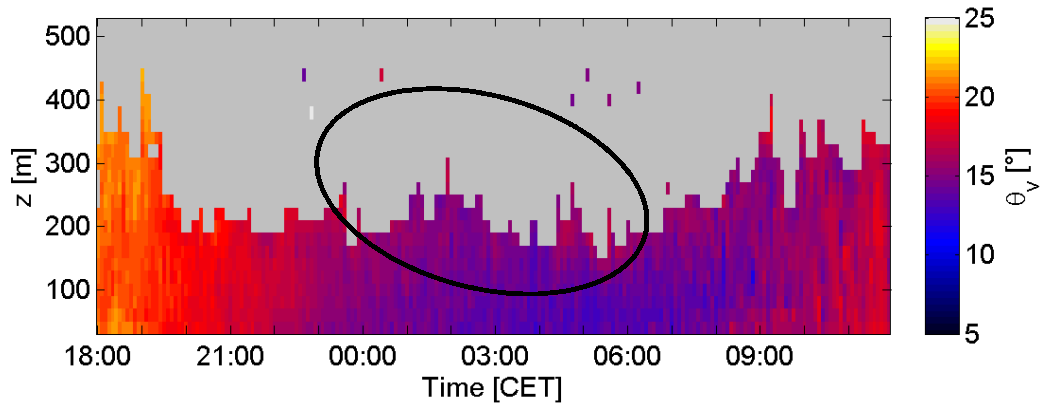


Figure 29: Sodargram of the potential temperature  $\theta$  from June 14<sup>th</sup> to 15<sup>th</sup> 2003. The region of the LLJ shown on in Figure 27 is indicated.

This event meets the category 2 after Bonner (1968), which required a  $v_{h \max} \geq 12 \text{ ms}^{-1}$  and a drop of  $v_h$  above  $z(v_{h \max})$  of at least  $6 \text{ ms}^{-1}$  (see Section 2.5). Figure 28 shows the corresponding sodargram of  $\varphi$ . The LLJ occurs within a layer with wind directions from the N sector beneath a layer with wind directions around west. Before the wind direction changes to N, the wind came from SE. As discussed in Subsection 4.2.1 the wind within the SE sector turns clockwise with increasing height to directions around SW. Due to a limited sounding range, the entire profile of  $\varphi$  could not be observed. With the change of  $\varphi$  to the N sector, the sounding range increased (around 20:45 CET), and  $\varphi$  in greater altitudes shows directions around SW, corresponding to the upper part of the mean profile found for the SE sector (Subsection 4.2.1). In the lower 450 m the flow remains within the N sector. This findings lead to the assumption, that the process forcing the wind to turn into the N sector does not affect the flow above the resulting shear layer. A detailed description of shear layers can be found in Subsection 4.2.5. As the altitude of this shear layer is very variable, the separation into two different air masses is certainly caused by meteorological effects and not by the topography. The latter would cause a shear layer in an altitude remaining relatively constant with time. The maximum intensity of the LLJ is reached around 01:00 CET. At this time, the altitude of the shear layer exceeds the sounding range of the SODAR system. In the sodargram of  $\theta$  (Figure 29), the cooling due to radiation during night is clearly visible, providing stable conditions needed for the LLJ to develop. The temperature gradient  $\Delta T/\Delta z$  changes from  $-0.60 \text{ Km}^{-1}10^{-2}$  prior to the LLJ event to  $-0.35 \text{ Km}^{-1}10^{-2}$  during the event. A sudden change in temperature was not observed. In the chart of the pressure field at ground level (not shown) no front can be found in the experimental area during this event. If the occurrence of the wind from the N sector is

associated with the advection of a different air mass, it has at least no different temperature and is not bound to a strong frontal system.

A third LLJ event occurred in the night from July 6<sup>th</sup> to 7<sup>th</sup> 2003. With its duration time of several hours it is comparable to the event from June 14<sup>th</sup> to 15<sup>th</sup> 2003. Prior to the LLJ event, a temperature gradient  $\Delta T/\Delta z$  of  $-1.16 \text{ Km}^{-1}10^{-2}$  was found, indicating very unstable conditions. During the LLJ event, the atmosphere was found to be stable with  $\Delta T/\Delta z$  of  $+0.08 \text{ Km}^{-1}10^{-2}$ . The sodargram of  $v_h$  is shown in Figure 30. The LLJ lasted approx. seven hours, reaching a maximum wind speed around  $11 \text{ ms}^{-1}$ . Most of the data within the jet are rejected by the quality control due to low values of the SNR. The behaviour of  $\phi$  during this LLJ event is shown in Figure 31. At the onset of the LLJ,  $\phi$  is already within the N sector, but changes from direction around NNW to direction around NNE during the LLJ event. A shear layer, where  $\phi$  turns from directions around N to directions around W, indicates the upper boundary of the jet. This shear layer subsides during the LLJ event.

In the entire dataset of the WALDATEM-2003 experiment, 984 wind profiles with a secondary maximum of the wind speed  $v_{h \text{ max}}$  during the night within the lowest 800 m were detected, according to the criterion from Stull (1988), presented in Section 2.5.  $Z(v_{h \text{ max}})$ , i.e. the altitude of the LLJ, varied mainly between 60 m and 400 m. Nevertheless, higher altitudes were some times found. Figure 32 shows the dependency of  $z(v_{h \text{ max}})$  on  $v_{h \text{ max}}$ . The altitude of the LLJ increases with increasing  $v_{h \text{ max}}$  with a coefficient of correlation of  $R = 0.58$ . This correlation is significant with an error probability of 1 % (Taubenheim, 1969), confirming the results from Banta et al. (2002). The correlation of the LLJ altitude with  $v_{h \text{ max}}$  leads to the conclusion, that high values of  $v_{h \text{ max}}$  can not occur at low altitudes, which is caused by the influence of frictional drag at lower altitudes. The frictional drag prevents  $v_{h \text{ max}}$  to reach greater values. The properties of the visually derived LLJ events presented in this section i.e. the altitude of the LLJ and the values of  $v_{h \text{ max}}$  agree well with the results from other studies (e.g. Brook, 1985; Garrat, 1985; Banta et al., 2002). The characteristics of the phenomenon LLJ, basically  $v_{h \text{ max}}$ ,  $Z(v_{h \text{ max}})$ , appear not to be altered by the topography, while possible ranges of  $\phi$  for a LLJ to occur are strongly dependent on topography.

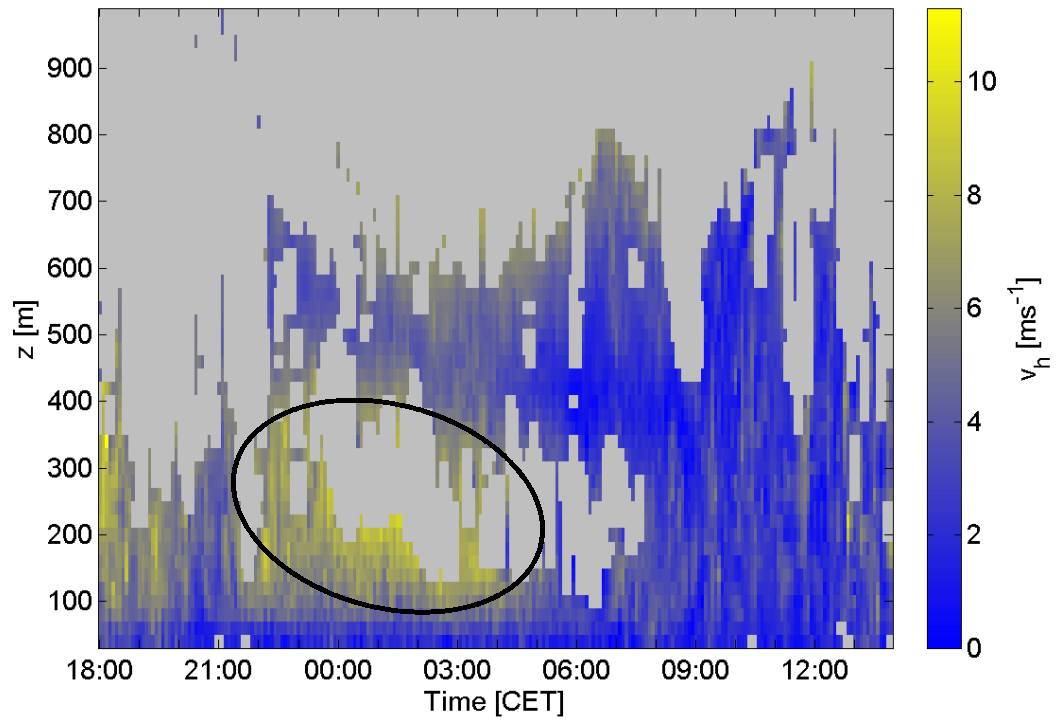


Figure 30: Sodargram of  $v_h$  from July 6<sup>th</sup> to 7<sup>th</sup> 2003. The circle indicates the position of the LLJ.

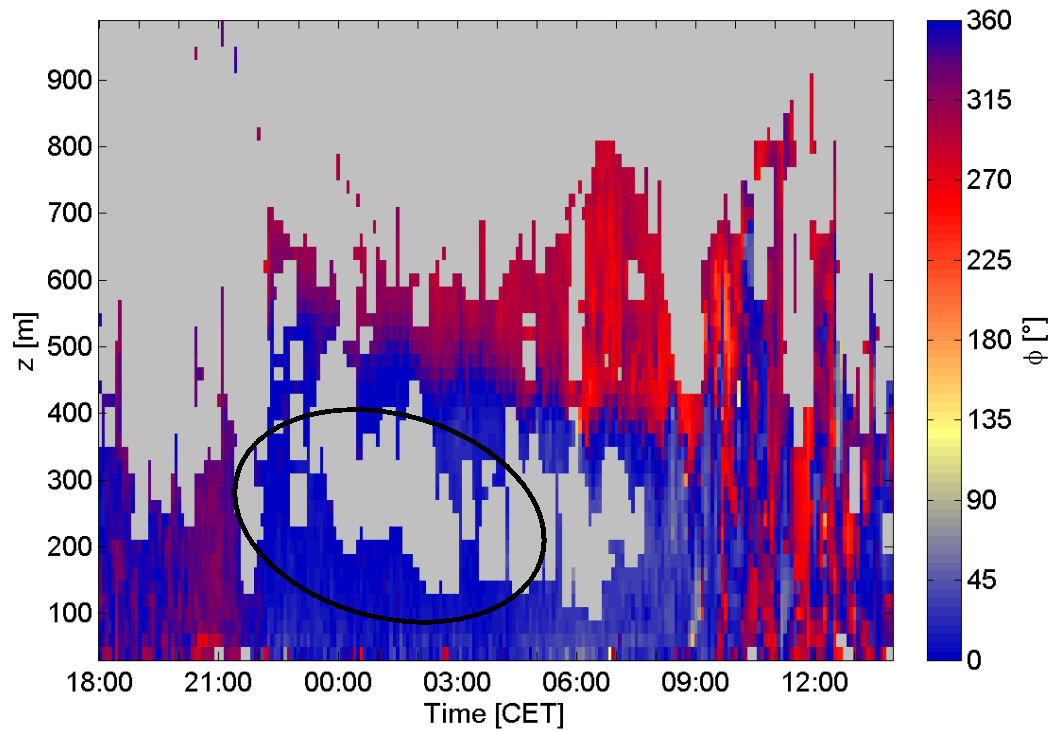


Figure 31: Sodargram of  $\phi$  from July 6<sup>th</sup> to 7<sup>th</sup> 2003. The position of the LLJ from Figure 30 is indicated.

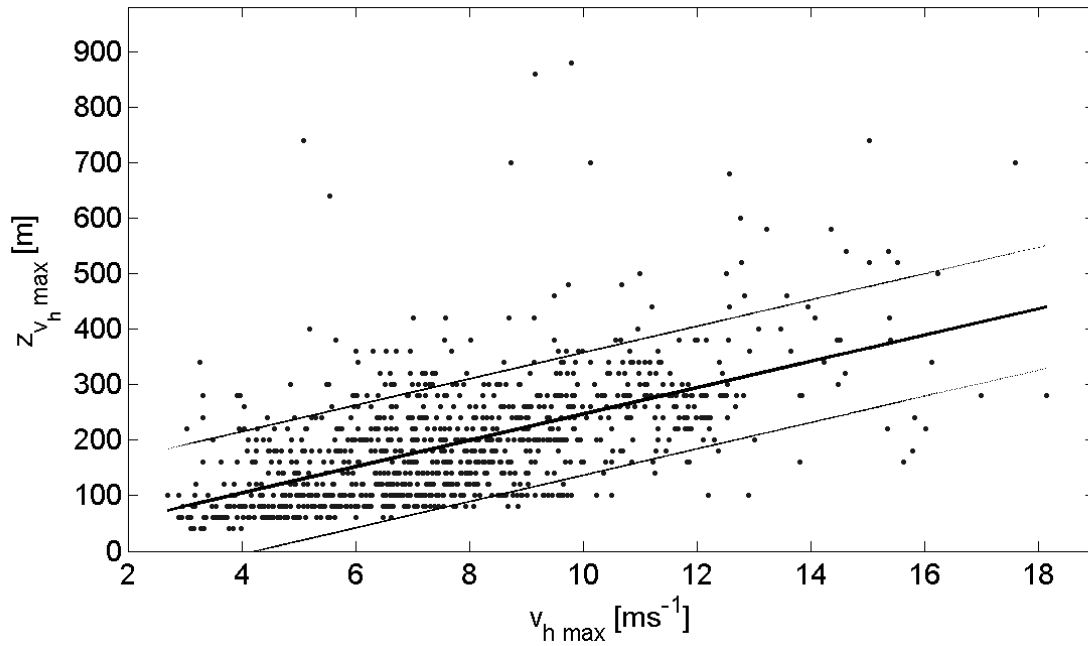


Figure 32: Dependency of the altitude  $z_{v_h \max}$  of the LLJ on the value of the wind speed maximum  $v_{h \max}$ . The middle line represents the linear regression ( $R = 0.58$ ), the upper and lower line indicate  $\pm 1$  standard deviation.  $n=984$  for the entire WALDATEM-2003 experiment.

#### 4.2.5 Shear layers

In this subsection the occurrence of shear layers and of typical patterns in the sodargram of reflectivity are investigated. A shear layer is characterised by a strong change of either  $v_h$  or  $\phi$  with changing altitude. In contrast to a LLJ, a shear layer of  $v_h$  only needs a sudden change of  $v_h$  or  $\phi$  with changing height. A drop below a certain threshold in a greater altitude is not required. Both types of shear can be derived visually from sodargram of  $v_h$  or  $\phi$ . As a strong wind shear mechanically induces turbulence, and two different air masses often have different temperatures, a shear layer often appears as a region of increased reflectivity in a sodargram. Two events of strong shear layers will be presented here.

Figure 33 shows a sodargram of reflectivity for the night from June 13<sup>th</sup> to 14<sup>th</sup> 2003. A scheme to encode patterns in a sodargram of reflectivity was published by Foken et al. (1987). The authors basically distinguish patterns touching the ground and elevated patterns (both horizontal patterns), convective patterns (a vertical pattern) and transitional patterns. Further discriminations are the homogeneity of the structure, the occurrence of multiple patterns and several patterns. Special features, e.g. wave patterns or merging patterns, are assigned as a last step. After this classification Figure 33 shows multiple patterns, consisting of a homogeneous ground based pattern with an overlying elevated wavy pattern. The elevated layer of increased reflectivity shows a wavy structure and merges with the ground based structure around

07:30 CET. Above the elevated layer of increased reflectivity, a region of slightly increased reflectivity can be found. Figure 34 shows the corresponding sodargram of  $\varphi$ . The marked boundary of the elevated maximum of reflectivity encloses very well the region of the intense shear, with the wind turning from E to SW. The strong shear in  $\varphi$  mechanically induces turbulence. This turbulence causes fluctuations of temperature, resulting in high values of reflectivity. The region of slightly increased reflectivity does not have a visible counterpart in the sodargram of  $\varphi$ . Figure 35 shows a sodargram of reflectivity for the morning of July 6<sup>th</sup> 2003. Before 04:00 CET, the structure can be classified as homogeneous pattern touching the ground. Around 04:00 CET, a layer of intense reflectivity separates from the ground based pattern and elevates, until it disintegrates around 07:30 CET. Such a separating pattern was not reported and considered by Foken et al. (1987). The corresponding sodargram of  $\varphi$ , displayed in Figure 36, exhibits a strong shear of  $\varphi$  in the region of the increased reflectivity. Within this shear layer, the wind turns from NNE to WNW with increasing height. The characteristics of both events of shear layers are summarised in Table 7. The temporal change of the altitude of the shear layer is different for both events. In the night from June 13<sup>th</sup> to 14<sup>th</sup>, a decrease of the altitude with time was recorded, while in the morning of June 6<sup>th</sup> altitude increased with time. There was also a difference in  $\varphi$  between the two events. For June 13<sup>th</sup> to 14<sup>th</sup>, the wind near the ground blew from the SE sector, turning clockwise in the shear layer with increasing height to directions around SW. At June 6<sup>th</sup>, the wind near the ground came from the N sector and turned counter clockwise with increasing height in the shear layer to directions around NNW. In both cases, the shear of  $\varphi$  was very intensive with values of  $90 \text{ }^\circ\text{m}^{-1}10^{-2}$  and more.

Table 7: Characteristics of the observed shear layers during WALDATEM-2003.

Date	$\varphi$ beneath	$\varphi$ above	Shear angle [ $^\circ\text{m}^{-1}10^{-2}$ ]
June 13 <sup>th</sup> / 14 <sup>th</sup>	E	SW	120
June 6 <sup>th</sup>	NNE	WNW	90

If one of the resulting layers becomes more dominant with time, it expands while the other layer is compressed or lifted upward. This explains the variation of the altitude of the shear layer with time, where the lower layer was found to expand (June 6<sup>th</sup>) or be compressed (June 12<sup>th</sup> to 14<sup>th</sup>).

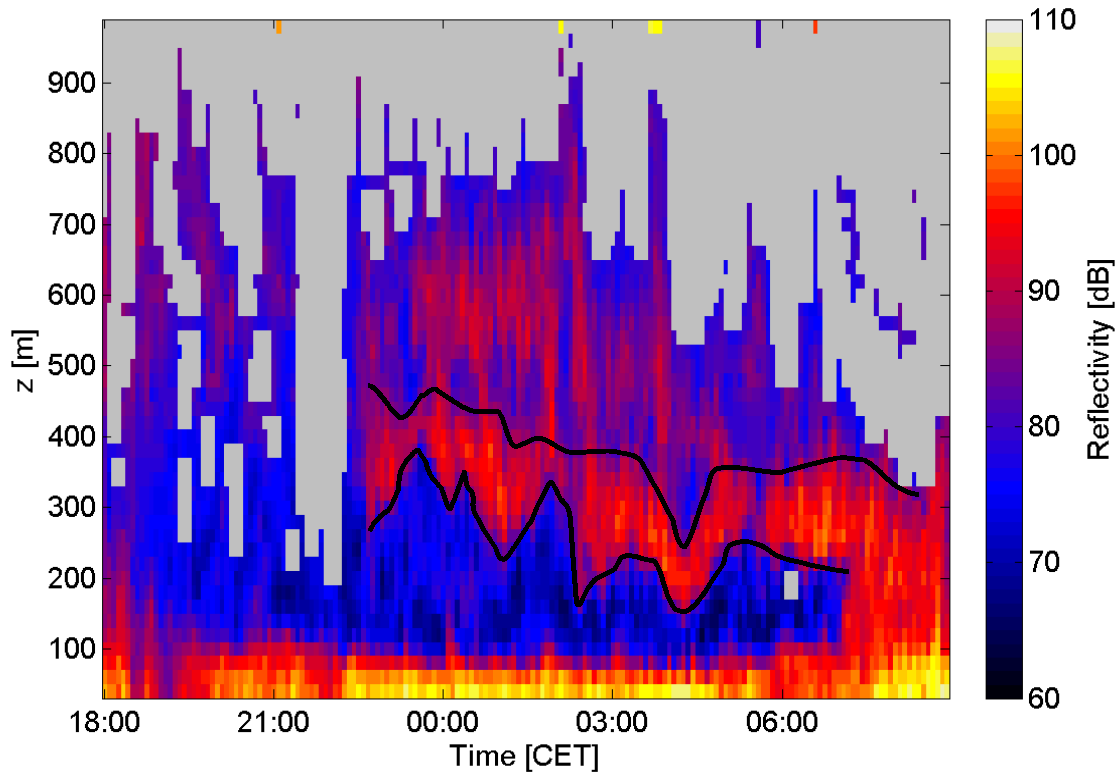


Figure 33: Sodargram of reflectivity from June 13<sup>th</sup> to 14<sup>th</sup> 2003. The boundary of the elevated maximum of reflectivity are marked.

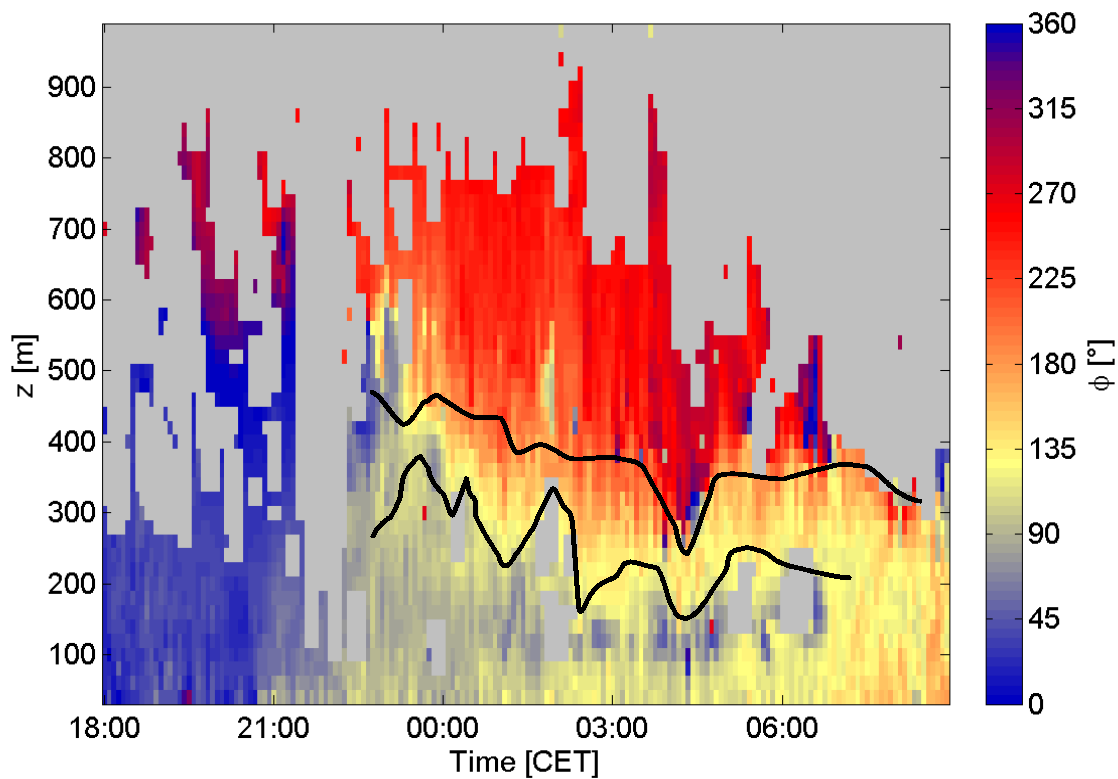


Figure 34: Sodargram of the wind direction  $\phi$  from June 13<sup>th</sup> to 14<sup>th</sup> 2003. The boundary of the elevated maximum of reflectivity is marked.

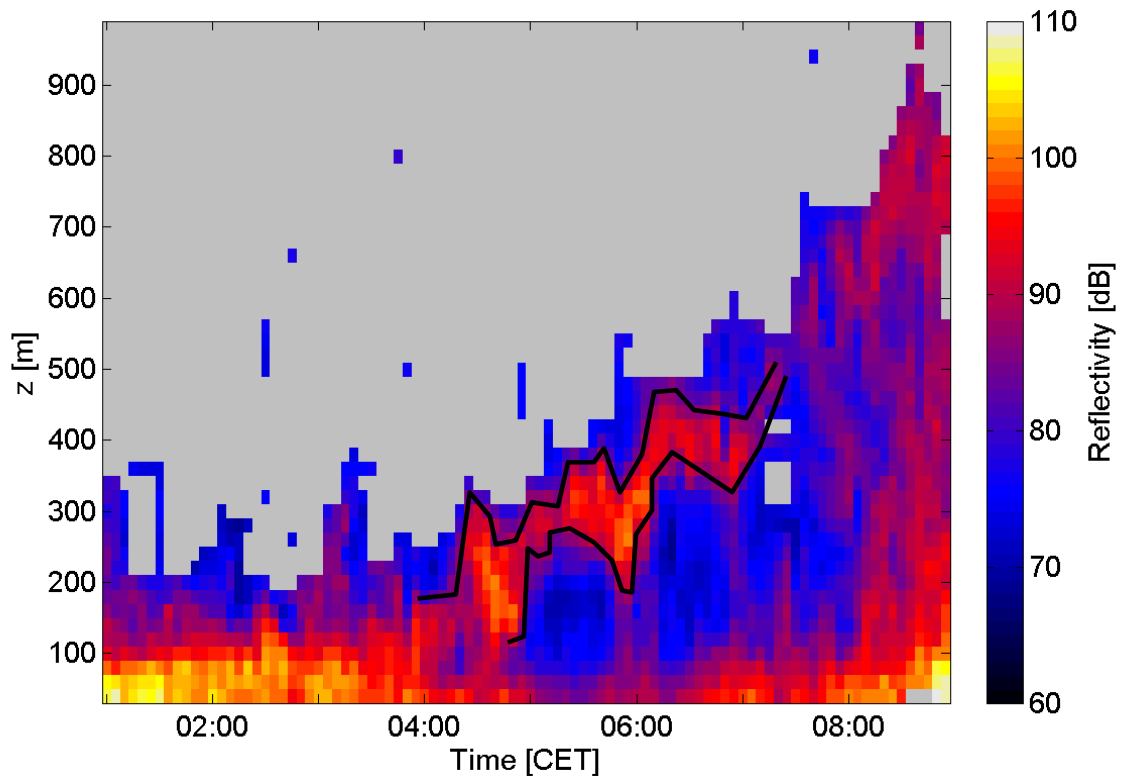


Figure 35: Sodargram of reflectivity from June 6<sup>th</sup> 2003. The boundary of the elevated maximum of reflectivity is marked.

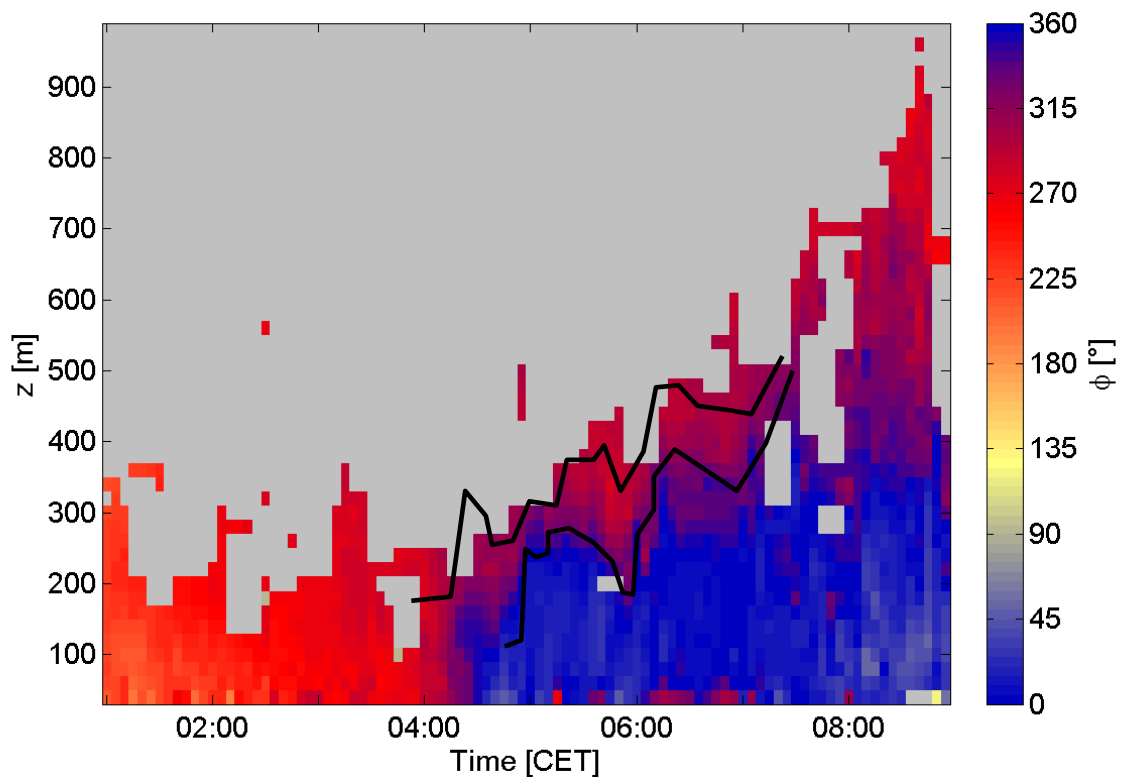


Figure 36: Sodargram of the wind direction  $\phi$  from June 6<sup>th</sup> 2003. The boundary of the elevated maximum of reflectivity is marked.

Regardless of the process of their development, the occurrence of shear layers at the Waldstein site makes assumptions concerning the origin of the advected air masses questionable, if they are only based on the geostrophic wind or the wind near the ground.

To quantify the frequency of occurrence of shear layers and other typical patterns observable in sodargrams of reflectivity, a scheme is needed to classify these patterns. Such a scheme was published by Foken et al. (1987). They basically distinguish between patterns touching the ground, elevated patterns and convective patterns, characterised by vertical structures in the sodargram of reflectivity. Special features can be assigned as a last step to get a detailed description of the pattern. According to this scheme, with slight modifications, frequently occurring patterns in the sodargram of reflectivity were classified. The discerned patterns and their frequency of occurrence during WALDATEM-2003 are summarised in Table 8.

Table 8: Absolute and relative frequency of the occurrence of typical patterns in the sodargram of reflectivity, according to Foken et al. (1987), modified. More than one pattern can be detected at one day or night.

Pattern		Day (42 sodargrams)		Night (41 sodargrams)	
Convective		34	81 %	-	-
Pattern touching the ground	Homogeneous	1	2 %	21	51 %
	Inhomogeneous	3	7 %	18	44 %
Multiple patterns		2	5 %	8	20 %
Several patterns		-	-	1	3 %
Pattern not touching the ground	Continuing beyond the sounding range	1	2 %	-	-
	Elevating pattern in the morning	6	14 %	-	-
Merger of a free and an on-the-ground pattern		2	5 %	4	10 %
No distinct pattern observable		4	10 %	4	10 %
Strong disturbances in sodargram		2	5 %	-	-

As the human eye is very effective in recognising patterns, the number of occurrence of the patterns was obtained visually from the sodargrams of reflectivity. Because one sodargram

can exhibit more than one pattern defined in the first column of Table 8, the sum of all counts exceeds the number of evaluated sodargrams.

### **4.3 Development of the mixed layer**

This section presents the results of the observations of the development of the mixed layer ML and a comparison with the output of a model.

#### **4.3.1 Observations of the development of the mixed layer**

The characteristic pattern of an elevated secondary maximum of reflectivity (Beyrich, 1997; Seibert et al., 2000), which is an indicator of the mixed layer height MLH in a convective boundary layer (CBL) (see Section 2.4), was clearly observable on two days. In this study, the mean height of the elevated maximum of reflectivity will be used as indicator.

In the sodargram of reflectivity (Figure 37) for June 7<sup>th</sup>, such a secondary maximum can be found. The region of the secondary maximum starts to elevate around 06:00 CET at a rate of approx.  $150 \text{ m h}^{-1}$ . Around 06:00 CET a noticeable drop in the reflectivity near the ground can be observed. It is the result of the transition from stable to unstable conditions, where the stratification of the boundary layer is almost neutral. Under such conditions, only weak temperature fluctuations are likely to occur. This leads to low values of reflectivity and short sounding ranges. As the assumption of an elevated region of increased reflectivity as the upper boundary of the ML is valid only under convective conditions, the corresponding sodargram of  $\sigma_w$  is shown in Figure 38. Beneath the marked position of the elevated maximum of reflectivity a very turbulent region due to convection can be found, indicating a zone of intense mixing.

The second day with a clear observation of the development of the ML is June 21<sup>st</sup>. The earliest visible secondary maximum of reflectivity is found at an altitude of 380 m (see Figure 39). The change from a SBL to a CBL is evident in the minimum of reflectivity near the ground around 06:00 CET. The region beneath the elevated maximum of reflectivity shows high and fluctuating values of  $\sigma_w$ , which is typical for a developing ML. As there was no shear layer observed which could cause the reflectivity to increase (not shown), the elevated maximum of reflectivity can be assumed as the MLH. The basic characteristics of the observed development of the ML are summarised in Table 9.

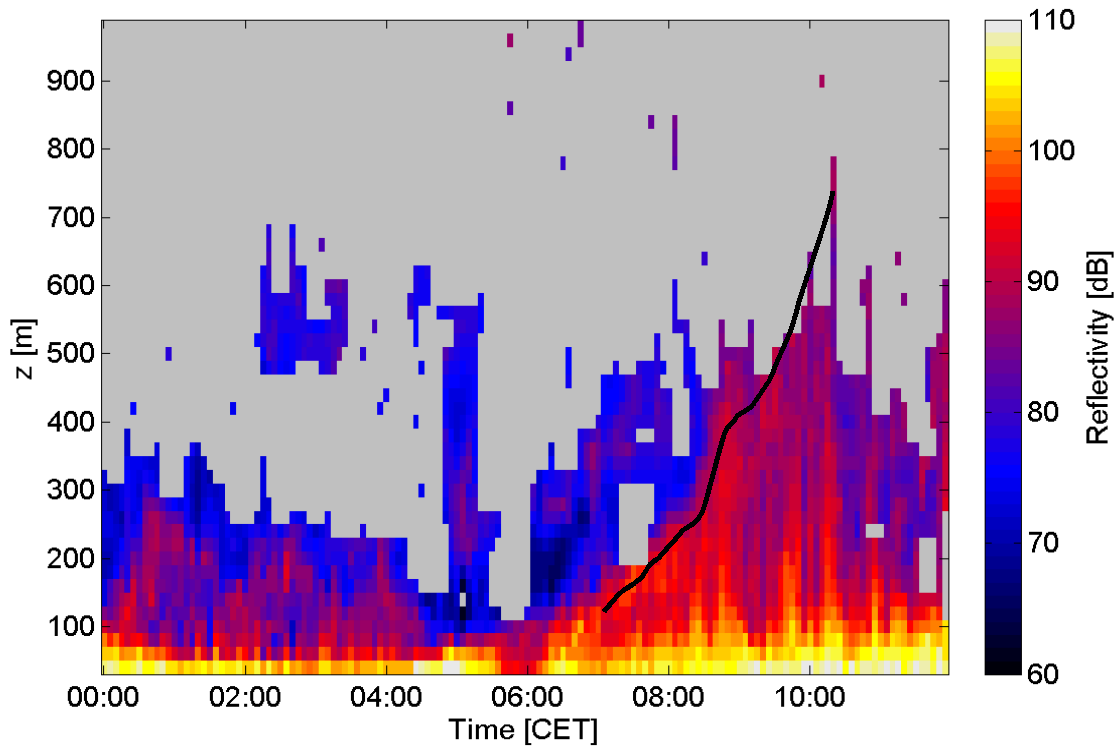


Figure 37: Sodargram of reflectivity from June 7<sup>th</sup> 2003. The position of the elevating secondary maximum of reflectivity is indicated by the line.

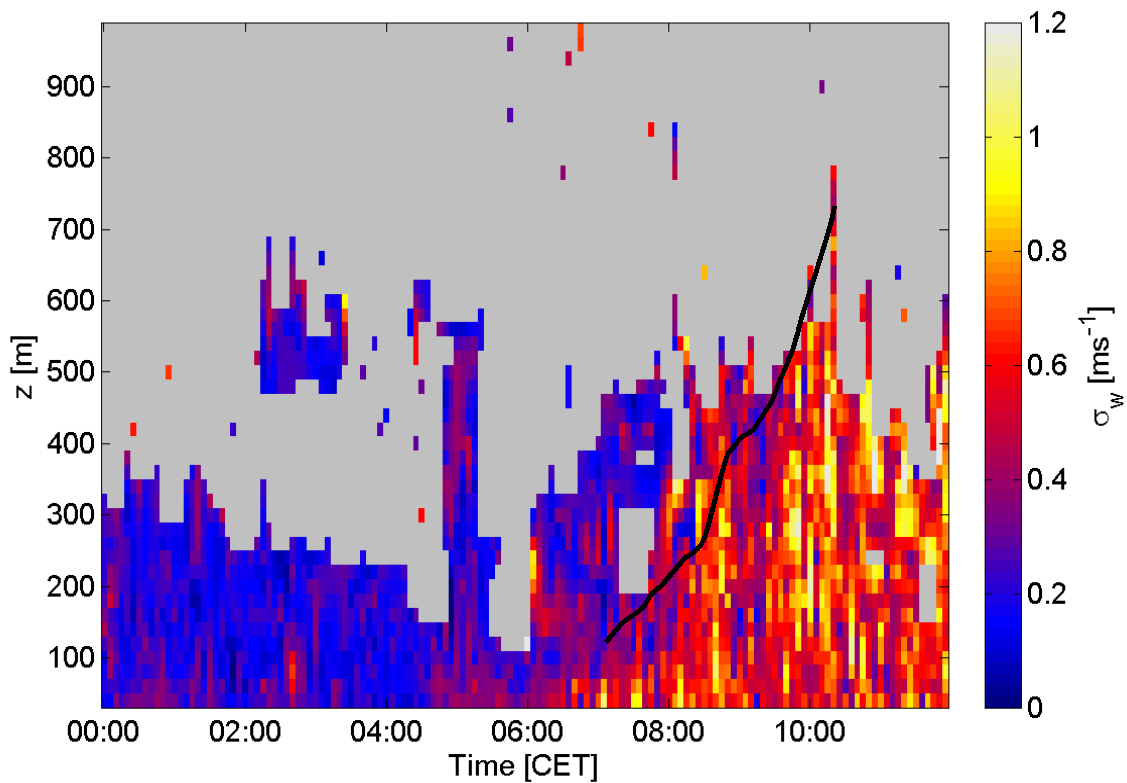


Figure 38: Sodargram of the standard deviation of the vertical wind velocity  $\sigma_w$  from June 7<sup>th</sup> 2003. The line indicates the position of the elevating secondary maximum of reflectivity in Figure 37.

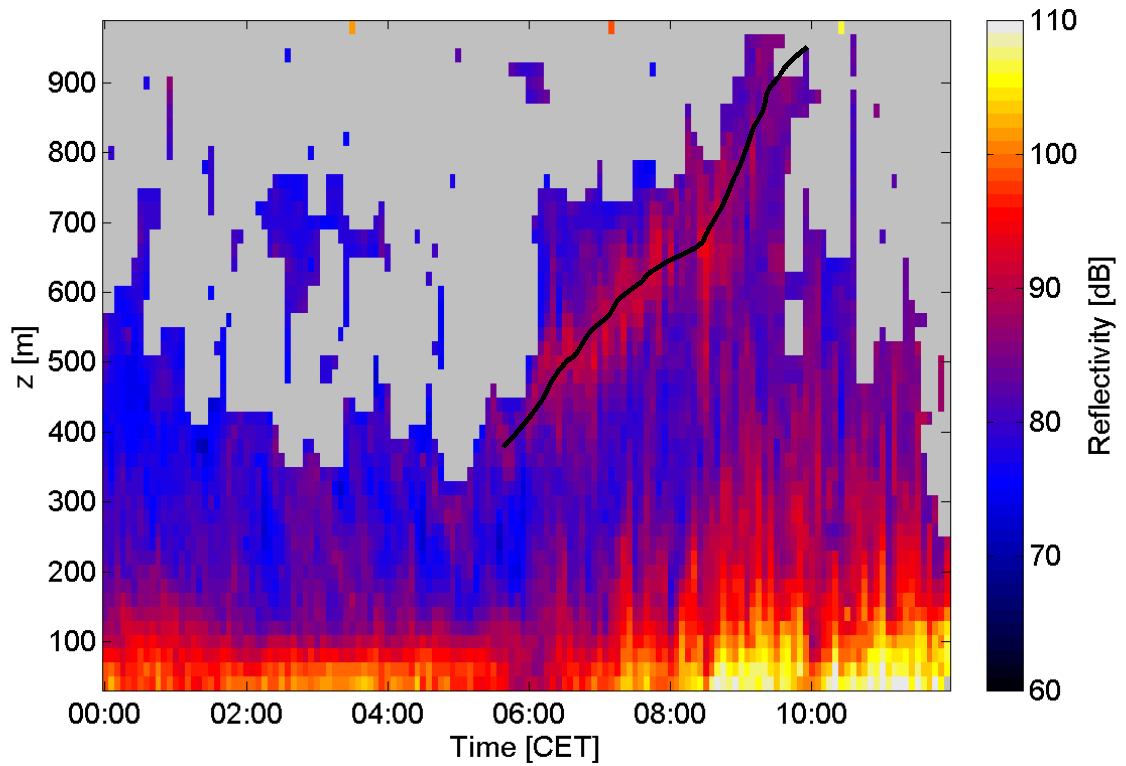


Figure 39: Sodargram of reflectivity from June 21<sup>st</sup> 2003. The position of the elevating secondary maximum of reflectivity is indicated by the line.

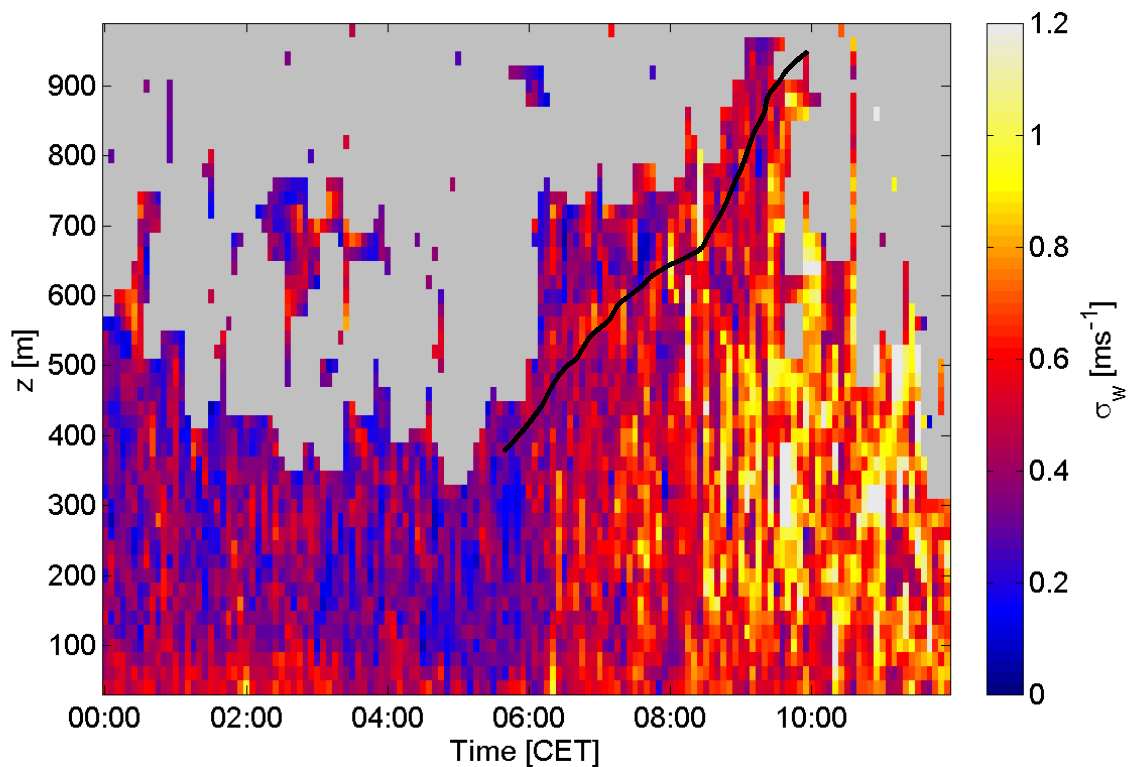


Figure 40: Sodargram of the standard deviation of the vertical wind velocity  $\sigma_w$  from June 21<sup>st</sup> 2003. The line indicates the position of the elevating secondary maximum of reflectivity in Figure 39.

At June 7<sup>th</sup>, a development of the ML was observed from near the ground, while for June 21<sup>st</sup> the earliest elevated maximum of reflectivity, the indicator for the MLH, was found already at an altitude of 380 m. This initial height indicates the altitude of the residual layer of the preceding day. Due to an above-average sounding range in the forenoon of June 21<sup>st</sup>, it was possible to observe the development of the ML up to an altitude of 940 m. The observed elevating rates are comparable to other studies, such as Emeis et al. (2004) and Beyrich (1997).

Table 9: Observations of the development of the mixed layer height during WALDATEM-2003, using the reflectivity criterion after Beyrich (1997).

Date	Height [m] at 06:00 CET	Height [m] at 10:00 CET	Maximum elevat- ing rate [mh <sup>-1</sup> ]	Maximum elevat- ing rate [mh <sup>-1</sup> ]
June 7 <sup>th</sup>	---	520	150	180
June 21 <sup>st</sup>	380	940	140	140

An other possibility is to derive the development of the ML from sodargrams of the categories of diffusion. This was done for categories of diffusion, determined according to KTA 1509 (Kerntechnischer Ausschuss, 1989, Table 7.4). With this attempt it was possible to observe the development of the ML at 15 of 37 days. The mean properties of the development of the ML derived from the categories of diffusion and its standard deviations are summarised in Table 10.

Table 10: Mean development of the mixed layer height during WALDATEM-2003, using the category of diffusion according to KTA 1509 (Kerntechnischer Ausschuss, 1989, Table 7.4). n = 15.

Time of earliest detectable pattern [CET] ± [h]	Height of earliest detectable pattern [m] ± [m]	Time of latest detectable pattern [CET] ± [h]	Height of latest detectable pattern [m] ± [m]	Mean elevat- ing rate [mh <sup>-1</sup> ] ± [mh <sup>-1</sup> ]
8:00 ± 1:20	80 ± 60	9:40 ± 1:00	570 ± 150	330 ± 130

The values of the elevating rates are higher than values derived from the reflectivity, but the onset of the development of the ML was found to be similar. These values agree well with results reported by Coulter (1979). From all observed developments of the ML, 11 events (73 %) were found to occur under wind directions from the SE sector, three events (20 %)

occurred with wind from the W sector and only one event (7 %) was observed with wind blowing from the N sector.

### 4.3.2 Model results of the development of the mixed layer

The boundary layer model by Blackadar (1997) was used in this study to compare the observations of the development of the ML, described in Subsection 4.3.1. The model is a one-dimensional time-dependent model simulation of the atmospheric boundary layer. Three-dimensional versions of this model are used in the Penn State – NCAR mesoscale model and the U.S. National Acid Deposition Model. A detailed description of the one-dimensional model can be found in Blackadar (1997). The model was initialised at 00:00 CET of each day with an observed development of the ML. In lower altitudes, the initial profiles of wind speed and temperature were derived from SODAR data. For heights exceeding the SODAR range, additional data were derived from radiosonde soundings, routinely performed at a site of the German weather service in a distance of approx. 110 km. Initial surface data were obtained from routine measurements at the Waldstein site. Figure 41 shows the MLH for all runs as it was predicted by the model. The main development of the ML begins around 07:00 CET, the maximum elevating rates can be observed between 08:30 CET and 11:30 CET. Later, the height of the ML remains between 1600 m and 2300 m. The mean properties of the model predictions are summarised in Table 11.

Table 11: Model predictions of the mean development of the mixed layer height during WAL-DATEM-2003.  $n = 12$ .

Time of predicted start of ML development [CET] $\pm$ [h]	Initial height of the ML [m] $\pm$ [m]	Time of last value below $z = 1000$ m [CET] $\pm$ [h]	Mean elevating rate [ $\text{mh}^{-1}$ ] $\pm$ [ $\text{mh}^{-1}$ ]
7:50	370	10:00	260
$\pm 0:50$	$\pm 40$	$\pm 1:00$	$\pm 60$

The predicted onset of the development coincides well with the observations, summarised in Table 10. However, the initial height predicted by the model is approx. 300 m higher than in the observations. This can be caused by the height resolution of the model, which is 100 m. The model might need some layers to derive a MLH, limiting the lowest possible prediction. The time of the last predicted values of the MLH below  $z = 1000$  m corresponds well to the last detectable pattern from the observations (Table 10).

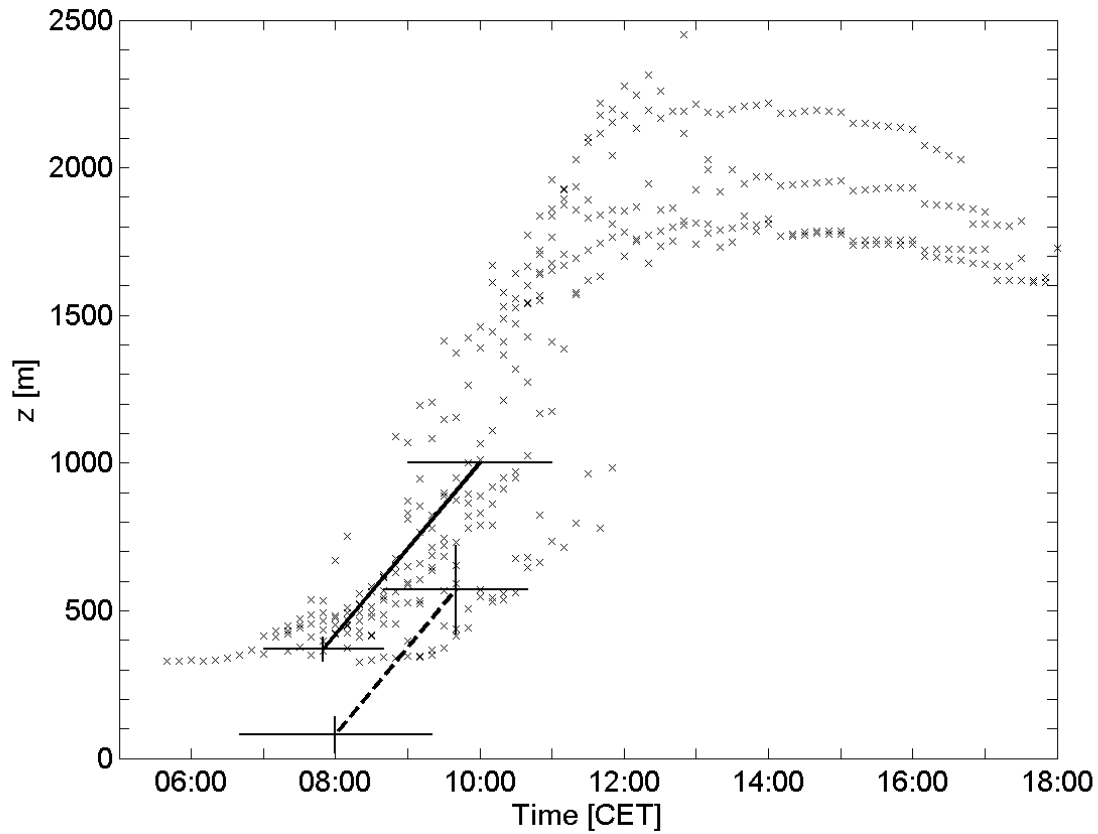


Figure 41: Development of the mixed layer ML on 12 days, as predicted by the Blackadar (1997) model. The two lines indicate the mean properties (solid: model; dotted: observations) of the mixed layer development within the lowest 1000 m. Vertical and horizontal bars are standard deviations.

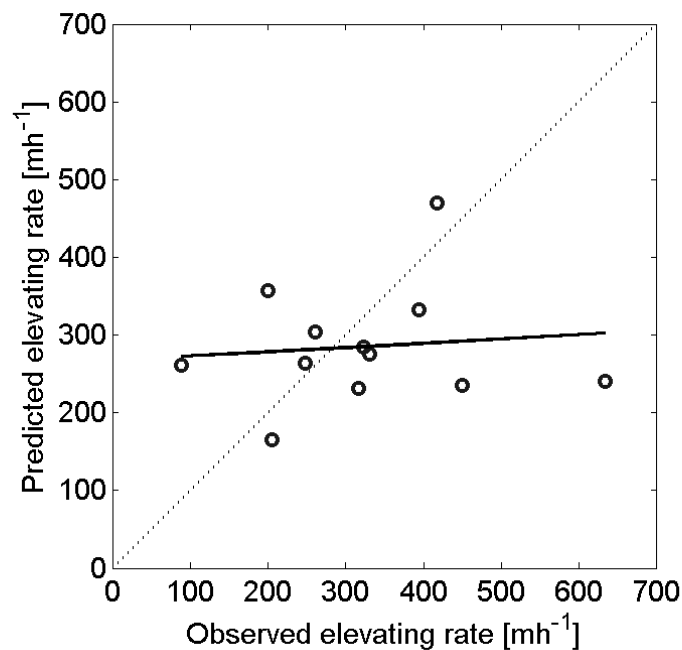


Figure 42: Comparison between the observed elevating rates of the MLH and the predictions from the Blackadar (1997) model. The solid line indicates the linear regression with  $R = 0.10$ .

---

The height of 1000 m was chosen as maximum height where the MLH could have been detected by the SODAR system. When the ML exceeds the range of the SODAR, the model calculations leave the lowest 1000 m of the ABL. The height difference between the last observed pattern (570 m, Table 10) and the exceeding of the lowest 1000 m is approx. 400 m. The absolute heights of the predictions seem to be in general around 350 m greater than in the observations. In contrast, the observed and predicted mean elevating rates are quite comparable. This finding is mainly caused by averaging out the variability of the dynamic development of the mixed layer. A comparison of single elevating rates from observations and model predictions is shown in Figure 42. The low correlation with  $R = 0.10$  indicates, that the development of the ML on a single day can not be represented by the predictions of the model. The individual effects which influence the elevating rate are too complex to be properly considered in calculations based on one initial profile several hours before sunrise.



## 5. Conclusions

The main objective of this study was to extend the characterisation of the Waldstein experimental site by evaluating wind- and temperature profiles in the lower atmospheric boundary layer. All profiles were recorded using a SODAR-RASS. Furthermore, the quality of the measurements was ascertained by comparing SODAR-RASS derived data to standard meteorological mast measurements. The data used for this comparison were obtained in the late summer 2003.

The findings lead to the following conclusions:

- The SODAR-RASS system provides reliable measurements of wind velocity and temperature within the surface layer, where exact measurements are most important due to strong gradients.
- The topography has a severe impact on the determination of the origin of air masses based on the geostrophic wind or the wind near the ground. For disturbed wind fields, no reliable relation between the geostrophic wind and the wind velocity near the ground can be found. So calculations based on trajectories have to be interpreted with caution.
- Extrapolation methods for wind profiles, e.g. the power law, can not cover the complexity of the wind field and thus are not able to substitute measurements.
- Obstacles in the approaching flow prevent low-level jets from developing. As the North sector is the only sector with an undisturbed approaching flow, low-level jet events were only observed for northerly wind directions.
- The criterion of an elevated maximum of reflectivity is not generally applicable at the site, as a clear pattern of increased reflectivity was seldom observed. Nevertheless it enables the observation of the development of the mixed layer over complex terrain on certain days. The development of the mixed layer above a mountain site shows a comparable pattern as observed in urban areas and flat terrain.
- The categories of diffusion provide a good measure to frequently observe the development of the mixed layer. Values of the mean increase of the mixed layer height are generally higher than values obtained with the criterion of an elevated maximum of reflectivity, but are still within the range reported from other sites.
- The Blackadar (1997) model is not suitable to calculate the mixed layer height at a complex site.



---

## 6. References

- Akima, H., 1970. A new method of interpolation and smooth curve fitting based on local procedures. *J. Assoc. Comput. Mach.*, **17**: 589-602.
- Alonso, M. and Finn, E.J., 1967. *Fundamental University Physics, Part 2: Fields and Waves*. Addison-Wesley Publishing Company, Reading, MA., 965 pp.
- Arya, S.P.S., 1981. Parameterizing the height of the stable atmospheric boundary layer. *J. Appl. Meteorol.*, **20**: 1192-1202.
- Arya, S.P.S., 2001. *Introduction to Micrometeorology*. Intern. Geophys. Ser. 79, Academic Press, San Diego, CA., 420 pp.
- Aubrun, S., Koppmann, R., Leitle, B., Moellmann-Coers, M. and Schaub, A., 2004. Physical modeling of an inhomogeneous finite forest area in a wind tunnel - Comparison with field data and Lagrangian dispersion calculations. *Agric. For. Meteorol.*: in press.
- Banta, R.M., Newsom, R.K., Lundquist, J.K., Pichugina, Y.L., Coulter, R.L. and Mahrt, L., 2002. Nocturnal low-level jet characteristics over Kansas during CASES-99. *Boundary-Layer Meteorol.*, **105**: 221-252.
- Batchelor, G.K., 1957. Wave scattering due to turbulence. In: Sherman, F.S., (Ed.). *Symp. on Naval Hydraulics*. *National Academy of Sciences*, Washington, D.C., pp. 409-423.
- Batchelor, G.K., 2000. *An Introduction to Fluid Dynamics*. Cambridge Mathematical Library Cambridge University Press, Cambridge, 635 pp.
- Baxter, R.A., 1991. Determination of mixing heights from data collected during the 1985 CCCAMP field program. *J. Appl. Meteorol.*, **30**: 598-606.
- Beyrich, F. and Weill, A., 1993. Some aspects of determining the stable boundary layer depth from sodar data. *Boundary-Layer Meteorol.*, **63**: 97-116.
- Beyrich, F., 1994. Sodar observations of the stable boundary layer height in relation to the nocturnal low-level jet. *Meteorol. Z.*, **3**: 29-34.
- Beyrich, F., 1995. Mixing-height estimation in the convective boundary layer using SODAR data. *Boundary-Layer Meteorol.*, **74**: 1-18.

- Beyrich, F., 1997. Mixing Height Estimation from SODAR Data - a Critical Discussion. *Atmos. Environ.*, **31**: 3941-3953.
- Blackadar, A.K., 1957. Boundary-layer wind maximum and their significance for the growth of nocturnal inversions. *Bull. Amer. Meteorol. Soc.*, **38**: 283-290.
- Blackadar, A.K. and Tennekes, H., 1968. Asymptotic similarity in neutral barotropic planetary boundary layer. *Journal of Atmospheric Sciences*, **25**: 1015-1020.
- Blackadar, A.K., 1997. Turbulence and diffusion in the atmosphere. Springer-Verlag Berlin Heidelberg New York, Berlin Heidelberg, 185 pp.
- Blokhintzev, D., 1946a. The propagation of sound in an inhomogeneous and moving medium I, II. *J. Acoust. Soc. Amer.*, **18**: 322-334.
- Blokhintzev, D., 1946b. Acoustics of inhomogeneous moving medium. Nauka, Moscow, 206 pp.
- Bonner, W.D., 1968. Climatology of the low level jet. *Mon. Wea. Rev.*, **96**: 833-850.
- Brook, R.R., 1985. The Koorin nocturnal low-level jet. *Boundary-Layer Meteorol.*, **32**: 133-154.
- Buajitti, K. and Blackadar, A.K., 1957. Theoretical studies of diurnal wind-structure variations in the planetary boundary layer. *Quart. J. Roy. Met. Soc.*, **83**: 486-500.
- Corsmeier, U., Kalthoff, N., Kollé, O., Kotzian, M. and Fiedler, F., 1997. Ozone concentration jump in the stable nocturnal boundary layer during a LLJ-event. *Atmos. Environ.*, **31**: 1977-1989.
- Coulter, R.L., 1979. A comparison of three methods for measuring mixing layer height. *J. Appl. Meteorol.*, **18**: 1495-1499.
- Coulter, R.L. and Kallistratova, M.A., 2004. Two decades of progress in sodar techniques: a review of 11 ISARS proceedings. *Meteorol. Atmos. Phys.*, **85**: 3-19.
- Crescenti, G.H., 1998. The degradation of Doppler sodar performance due to noise: A review. *Atmos. Environ.*, **32**: 1499-1509.
- Doran, J.C. and Verholek, M.G., 1978. A note on vertical extrapolation formulas for Weibull velocity distribution parameters. *J. Appl. Meteorol.*, **17**: 410-412.

- Ekman, V.W., 1905. On the influence of the earth's rotation on ocean currents. *Arkiv. Matematik Astron. Fysik, Stockholm*, **2**: 1-52.
- Emeis, S., Münkkel, C., Vogt, S., Müller, W.J. and Schäfer, K., 2003. Vertikale Windprofile in der Ekman-Schicht und Validierung von Mischungsschicht Höhenbestimmungen aus Sodar-Daten. In: *2. Fachgespräch SODAR*, Bundesamt für Strahlenschutz, Oberschleißheim, BfS Schriften, **28**: pp. 115-129.
- Emeis, S., Münkkel, C., Vogt, S., Müller, W.J. and Schäfer, K., 2004. Atmospheric boundary-layer structure from simultaneous SODAR, RASS, and ceilometer measurements. *Atmos. Environ.*, **38**: 273-286.
- Engelbart, D.A.M., Görsdorf, U. and Adedokoun, J.A., 2003. Klimatologie von Low-Level Jets am Observatorium Lindenberg auf der Grundlage operationeller Sodar- und Windprofilermessungen. In: *2. Fachgespräch SODAR*, Bundesamt für Strahlenschutz, Oberschleißheim, BfS Schriften, **28**: pp. 131-140.
- Fetter, R.W., 1961. The EMAC probe - a new concept for remote atmospheric sounding by RADAR. In: *Proc. 9<sup>th</sup> Wea. Radar Conf.*, Kansas City, MO, pp. 385-390.
- Finkelstein, P.L., Kaimal, J.C., Gaynor, J.E., Graves, M.A. and Lockhart, T.J., 1986. Comparison of wind monitoring systems. Part II: Doppler-Sodars. *J. Atmos. Ocean. Technol.*, **3**: 594-604.
- Foken, T. and Skeib, G., 1983. Profile measurements in the atmospheric near-surface layer and the use of suitable universal functions for the determination of the turbulent energy exchange. *Boundary-Layer Meteorol.*, **25**: 55-62.
- Foken, T., Hartmann, K.-H., Keder, J., Küchler, W., Neisser, J. and Vogt, F., 1987. Possibilities of an Optimal Encoding of SODAR Information. *Z. Meteorol.*, **35**: 348-354.
- Foken, T., 2003. *Angewandte Meteorologie, Mikrometeorologische Methoden*. Springer Verlag, Heidelberg, 289 pp.
- Frisch, A.S. and Clifford, S.F., 1974. A study of convection capped by a stable layer using Doppler radar and acoustic echo sounders. *J. Atmos. Sci.*, **31**: 1622-1628.
- Garrat, J.R., 1985. The inland boundary layer at low latitudes. Part 1, The nocturnal jet. *Boundary-Layer Meteorol.*, **32**: 307-327.

- Garrat, J.R., 1992. The atmospheric boundary layer. University Press, Cambridge, 316 pp.
- Gilman, G.W., Coxhead, H.B. and Willis, F.H., 1946. Reflection of sound signals in the troposphere. *J. Acoust. Soc. Amer.*, **18**: 274-283.
- Göckede, M., 2000. *Das Windprofil in den untersten 100 m der Atmosphäre unter besonderer Berücksichtigung der Stabilität der Schichtung*. Diploma thesis, University of Bayreuth, Dept. of Micrometeorology, Bayreuth, 133 pp.
- Göckede, M., Mauder, M. and Foken, T., 2004. Qualitätsbegutachtung komplexer mikrometeorologischer Massstationen im Rahmen des VERTIKO-Projekts. *University of Bayreuth, Dept. of Micrometeorology, Bayreuth, Arbeitsergebnisse*, **25**: 39 pp.
- Hanna, S.R., Burkhardt, C.L. and Paine, R.J., 1985. Mixing height uncertainties. In: *Proc. 7th AMS Symposium on Turbulence and Diffusion*, Boulder, pp. 82-85.
- Hanna, S.R. and Chang, J.C., 1992. Boundary layer parameterizations for applied dispersion modelling over urban areas. *Boundary-Layer Meteorol.*, **58**: 229-259.
- Harris, C.M., 1963. Absorption of sound in air in the audio-frequency range. *J. Acoust. Soc. Amer.*, **35**: 11-17.
- Harris, C.M., 1966. Absorption of sound in air versus humidity and temperature. *J. Acoust. Soc. Amer.*, **40**: 148-159.
- Haugen, D.A. and Kaimal, J.C., 1978. Measuring temperature structure parameter profiles with an acoustic sounder. *J. Appl. Meteorol.*, **17**: 895-899.
- Hess, G.D., 2004. The neutral, barotropic planetary boundary layer, capped by a low-level inversion. *Boundary-Layer Meteorol.*, **110**: 319-355.
- Holton, J.R., 1967. The diurnal boundary layer wind oscillation above sloping terrain. *Tellus*, **19**: 199-205.
- Hsu, S.A., Meindl, E.A. and Gilhousen, D.B., 1994. Determinating the power-law wind-profile exponent under near-neutral stability conditions at sea. *J. Appl. Meteorol.*, **33**: 757-765.
- Irwin, J.S., 1978. A theoretical variation of the wind profile power-law exponent as a function of surface roughness and stability. *Atmos. Environ.*, **13**: 191-194.

- Joffre, S.M., 1984. Power laws and the empirical representation of velocity and directional shear. *J. Appl. Meteorol.*, **23**: 1196-1203.
- Johansson, C., Smedman, A., Högström, U., Brasseur, J.G. and Khanna, S., 2001. Critical test of the Validity of Monin-Obukhov similarity during convective conditions. *Journal of Atmospheric Sciences*, **58**: 1549 - 1566.
- Justus, C.G. and Mikhail, A., 1976. Height variation of wind speed and wind distribution statistics. *Geophys. Res. Lett.*, **3**: 261-264.
- Kaimal, J.C., Abshire, N.L., Chadwick, R.B., Decker, M.T., Hooke, W.H., Kroepfli, R.A., Neff, W.D., Pasqualucci, F. and Hildebrand, P.H., 1982. Estimating the depth of the daytime convective boundary layer. *J. Appl. Meteorol.*, **21**: 1123-1129.
- Kaimal, J.C. and Gaynor, J.E., 1991. Another look at sonic thermometry. *Boundary-Layer Meteorol.*, **56**: 401-410.
- Kaimal, J.C. and Finnigan, J.J., 1994. Atmospheric Boundary Layer Flows: Their Structure and Measurements. Oxford University Press, New York, Oxford, 289 pp.
- Kallistratova, M.A., 1959. Procedure for investigating sound scattering in the atmosphere. *Sov. Phys. Acoust.*, **5**: 512-514.
- Kallistratova, M.A., 1997. Physical Grounds for Acoustic Remote Sensing of the Atmospheric Boundary Layer. In: Singal, S.P., (Ed.). Acoustic Remote Sensing Applications. *Springer Verlag*, Berlin, Heidelberg, New York, pp. 3-34.
- Keder, J., Foken, T., Gerstmann, W. and Schindler, V., 1988. Measurements of wind parameters and heat flux with the sensitron Doppler sodar. *Boundary-Layer Meteorol.*, **46**: 195-204.
- Kelton, G. and Bricout, P., 1964. Wind velocity measurements using sonic techniques. *Bull. Amer. Meteorol. Soc.*, **45**: 571-580.
- Kerntechnischer Ausschuss, 1989. *Instrumentierung zur Ermittlung der Ausbreitung radioaktiver Stoffe in der Atmosphäre*, Sicherheitstechnische Regel des KTA. Bundesamt für Strahlenschutz (BfS), Salzgitter, Germany, 17 pp.
- Koppmann, R., 2003. Emission and chemical transformation of biogenic volatile organic compounds (ECHO). *AFO 2000 Newsletter*, **5**: 7-10.

- Kraichnan, R.H., 1953. The scattering of sound in a turbulent medium. *J. Acoust. Soc. Amer.*, **25**: 1096-1104.
- Kraus, H., Malcher, J. and Schaller, E., 1985. A Nocturnal low level jet during PUKK. *Boundary-Layer Meteorol.*, **31**: 187-195.
- Lau, S.Y. and Chan, S.T., 2003. A crescent-shaped low-level jet as observed by a Doppler radar. *Weather*, **58**: 287-290.
- Lighthill, M.J., 1953. On the energy scattered from the interaction of turbulence with sound or shock waves. *Proc. Cambridge Phil. Soc.*, **49**: 531-555.
- Little, C.G., 1969. Acoustic methods for the remote probing of the lower atmosphere. *Proc. IEEE*, **57**: 571-578.
- Mangold, A., 1999. *Untersuchung der lokalen Einflüsse auf Turbulenzmessungen der Station Weidenbrunnen*. Diploma thesis, University of Bayreuth, Dept. of Micrometeorology, Bayreuth, 175 pp.
- Marshall, J.M., 1972. A radio acoustic sounding system for remote measurements of atmospheric parameters. *Stanford Electronics Laboratorie, US-SEL-72-003, Stanford, CA., Sci. Rep.*, **39**.
- Marshall, J.M., Peterson, A.M. and Barnes Jr., A.A., 1972. Combined radar-acoustic sounding systems. *Appl. Opt.*, **11**: 108-112.
- Marsik, F.J., Fischer, K.W., McDonald, T.D. and Samson, P.J., 1995. Comparison of methods for estimating mixing height used during the 1992 Atlanta Field Initiative. *J. Appl. Meteorol.*, **34**: 1802-1814.
- Matuura, N., Masuda, Y., Inuki, H., Kato, S., Fukao, S., Sato, T. and Tsuda, T., 1986. Radio acoustic measurements of temperature profile in the troposphere and stratosphere. *Nature*, **333**: 426-428.
- May, P.T., Strauch, R.G. and Moran, K.P., 1988. The altitude coverage of temperature measurements using RASS with wind profiler RADARs. *Geophys. Res. Lett.*, **15**: 1381-1384.
- May, P.T., Moran, K.P. and Strauch, R.G., 1989. The accuracy of RASS temperature measurements. *J. Appl. Meteorol.*, **28**: 1329-1335.

- McAllister, L.G., 1968. Acoustic sounding of the lower troposphere. *J. Atmos. Terr. Phys.*, **30**: 1439-1440.
- McAllister, L.G. and Pollard, J.R., 1969a. Acoustic sounding of the lower troposphere. In: *Proc. of the 6th Int. Symp. on remote sensing of the environment*, University of Michigan Press, University of Michigan, pp. 436-450.
- McAllister, L.G., Pollard, J.R., Mahoney, A.R. and Shaw, P.J.R., 1969b. Acoustic sounding - a new approach to the study of atmospheric structure. *Proc. IEEE*, **57**: 579-587.
- Mitchel, M., Arritt, R. and Labas, K., 1995. Climatology of the warm season great plains low-level jet using wind profiler observations. *Weather and Forecasting*, **10**: 576-591.
- Monin, A.S. and Obukhov, A.M., 1954. Osnovnye zakonomernosti turbulentnogo peremeshivaniya v prizemnom sloe atmosfery. *Trudy Inst. Theor. Geofiz. AN SSSR*, **24**: 163-187 (in Russian).
- Monin, A.S., 1962. Characteristics of the scattering of sound in a turbulent atmosphere. *Sov. Phys. Acoust.*, **7**: 370-373 (English translation).
- Moulsley, T.J., Cole, R.S., Asimakopoulos, D.N. and Caughey, S.J., 1979. Simultaneous horizontal and vertical acoustic sounding of the atmospheric boundary layer. *Boundary-Layer Meteorol.*, **17**: 223-230.
- Moulsley, T.J. and Cole, R.S., 1980. A general radar equation for the bistatic acoustic sounder. *Boundary-Layer Meteorol.*, **19**: 359-372.
- Neff, W.D., 1975. Quantitative evaluation of acoustic echoes from the planetary boundary layer. *NOAA, Boulder, CO., Technical Report ERL 322-WPL 38*: 34 pp.
- Neff, W.D., 1978. Beamwidth effects on acoustic backscatter in the planetary boundary layer. *J. Appl. Meteorol.*, **17**: 1514-1520.
- Neff, W.D. and Coulter, R.L., 1986. Acoustic remote sensing. In: Lenschow, D.H., (Ed.). *Probing the atmospheric boundary layer. American Meteorological Society*, Boston, MA, pp. 201-239.
- Noonkester, V.R., 1976. The evolution of the clear air convective layer revealed by surface based remote sensors. *J. Appl. Meteorol.*, **15**: 594-606.

- Obukhov, A.M., 1941. On sound propagation in vertical flow. *Dokl. Akad. Nauk. SSSR*, **39**: 46-49 (in Russian).
- Obukhov, A.M., 1943. Scattering of sound in turbulent flow. *Dokl. Akad. Nauk. SSSR*, **30**: 611-614 (in Russian).
- Obukhov, A.M., 1946. Turbulentnost v temperturnoj-neodnorodnoj atmosphere. *Trudy Inst. Theor. Geofiz. AN SSSR*, **1** (in Russian).
- Panofsky, H.A., Tennekes, H., Lenschow, D.H. and Wyngaard, J.C., 1977. The characteristics of turbulent velocity components in the surface layer under convective conditions. *Boundary-Layer Meteorol.*, **11**: 355-361.
- Pasquill, F., 1961. Estimation of the dispersion of windborne material. *Meteorol. Mag.*, **90**: 33-49.
- Peltier, L.J., Wyngaard, J.C., Khanna, S. and Brasseur, J.G., 1996. Spectra in the unstable surface layer. *Journal of Atmospheric Sciences*, **53**: 49-61.
- Peterson, E.W. and Hennessey, J.P.j., 1978. On the use of power laws for estimates of wind power potential. *J. Appl. Meteorol.*, **17**: 390-394.
- Quintarelli, F., 1993. Acoustic Sounder Observations of Atmospheric Turbulence Parameters in a Convective Boundary Layer. *J. Appl. Meteorol.*, **32**: 1433-1440.
- Reitebuch, O., Strassburger, A., Emeis, S. and Kuttler, W., 2000. Nocturnal secondary ozone concentration maxima analysed by sodar observations and surface measurements. *Atmos. Environ.*, **34**: 4315-4329.
- Roth, R., Wittich, K.P. and Falke, M., 1989. Eine Fallstudie zu einem nächtlichen Windfeld oberhalb der Reibungsschicht bei inhomogenem und instationärem geostrophischem Wind. *Meteorol. Rdsch.*, **41**: 129-136.
- Russel, P.B., Uthe, E.E., Ludwig, F.L. and Shaw, N.A., 1974. A comparison of atmospheric structure as observed with monostatic acoustic sounder and lidar technique. *J. Geophys. Res.*, **79**: 5555-5566.
- Sedefian, L., 1980. On the vertical extraplotion of meanwind power density. *J. Appl. Meteorol.*, **19**: 488-493.

- Seibert, P., Beyrich, F., Gryning, S.E., Joffre, S., Rasmussen, A. and Tercier, P., 1998. Mixing layer depth determination for dispersion modeling. In: Fisher, B.E.A., Erbrink, J.J., Fignardi, S., Jeannet, P. and Thomson, D.J., (Eds.). COST Action 710-Final Report. Harmonisation of the pre-processing of meteorological data for atmospheric dispersion models. *European Commission*, L-2985 Luxembourg, pp. 431.
- Seibert, P., Beyrich, F., Gryning, S.E., Joffre, S., Rasmussen, A. and Tercier, P., 2000. Review and intercomparison of operational methods for the determination of the mixing height. *Atmos. Environ.*, **34**: 1001-1027.
- Simmons, W.R., Wescott, J.W. and Hal Jr., F.F., 1971. Acoustic echo sounding as related to air pollution in urban environments. *NOAA, Boulder, CO, Technical Report ERL 216-WPL 17*: 77 pp.
- Singal, S.P., 1987. Noise problem in the design of SODAR system. *Indian J. Radio & Space Phys.*, **16**: 225-231.
- Stull, R.B., 1988. An introduction to boundary layer meteorology. Kluwer Academic Publisher, Dordrecht, 666 pp.
- Svoboda, J. and Cermak, J., 2002. Vertical profiles of wind speed over a mountain ridge. *Meteorol. Z.*, **11**: 361-366.
- Tatarskii, V.I., 1961. Wave propagation in a turbulent medium. McGraw-Hill, New York, 285 pp.
- Tatarskii, V.I., 1971. The effects of the turbulent atmosphere on wave propagation. In: Israel Program for Scientific Translations. *U.S. Department of Commerce*, Springfield, Virginia, pp. 74-76.
- Taubenheim, J., 1969. Statistische Auswertung geophysikalischer und meteorologischer Daten. Akad. Verlagsges., Leipzig, 386 pp.
- Taylor, G.I., 1915. Eddy motion in the atmosphere. *Phil. Trans. Roy. Soc.*, **215**: 1-26.
- Thomas, C., 2001. *Integral Turbulence Characteristics and Their Parameterisations*. Diploma thesis, University of Bayreuth, Dept. of Micrometeorology, Bayreuth, 101 pp.

- 
- Thomas, C., Ruppert, J., Lüers, J., Schröter, J., Mayer, J.C. and Bertolini, T., 2004. Documentation of the WALDATEM-2003 experiment April, 28<sup>th</sup> to August, 03<sup>rd</sup> 2003. *University of Bayreuth, Dept. of Micrometeorology, Bayreuth, Arbeitsergebnisse*, **24**: 59 pp.
- Thomas, C., Mayer, J.-C., Meixner, F.X. and Foken, T., 2005. Analysis of the low-frequency turbulence above tall vegetation using a Doppler sodar. *Boundary-Layer Meteorol.*: (submitted).
- Thomas, P. and Vogt, S., 1993. Intercomparison of turbulence data measured by SODAR and sonic anemometers. *Boundary-Layer Meteorol.*, **62**: 353-359.
- Tyndall, J., 1874. On the atmosphere as a vehicle of sound. *Phil. Trans. Roy. Soc.*, **164**: 183-244.
- Vogt, S., Thomas, P., Chevalier, G. and Gentou, H., 1990. Long-Term Intercomparison of Temperature Data Measured by RASS and Tower Instruments. In: Singal, S.P., (Ed.). *Acoustic Remote Sensing. Proceedings of the Fifth International Symposium on Acoustic Remote Sensing of the Atmosphere and Oceans. Tata McGraw-Hill Publ. Comp. Ltd, New Delhi*, pp. 115-121.
- Wippermann, F., 1973. *The planetary boundary layer of the atmosphere*. Deutscher Wetterdienst, Offenbach a.M., 346 pp.
- Wyngaard, J.C., Izumi, Y. and Collins Jr., S.A., 1971. Behavior of the Refraction-Index-Structure Parameter near the Ground. *J. Acoust. Soc. Amer.*, **61**: 1646-1650.
- Zilitinkevich, S.S., 1989. Velocity profiles, the resistance law and the dissipation rate of mean flow kinetic energy in a neutrally and stably stratified planetary boundary layer. *Boundary-Layer Meteorol.*, **46**: 367-387.
- Zilitinkevich, S.S. and Esau, I.N., 2002. On integral measures of the neutral barotropic planetary boundary layer. *Boundary-Layer Meteorol.*, **104**: 371-379.

## 7. Index of Figures

- Figure 1: Square shaped phased array with resulting five antennas (a1 – a5). The angles against zenith are indicated as  $\psi_2$  and  $\psi_4$ , the horizontal angle between the antennas is  $90^\circ$ . From: METEK, DSDPA.90 user manual, modified. .... 7
- Figure 2: Classical and molecular attenuation as a function of acoustic frequency. These curves are based on equations given by Neff (1975) for a temperature of  $20^\circ\text{C}$  (Crescenti, 1998). .... 9
- Figure 3: Evolution of the convective and stable boundary layers in response to surface heating and cooling. The time indicated is Local Standard Time LST (Kaimal and Finnigan, 1994, modified). .... 15
- Figure 4: Map of the experimental site of WALDATEM-2003; numbers on isopleths are heights [m] a. s. l. The indicated sectors are main wind sectors, described in Section 4.2.1. Map adapted from: see Index of Maps, Map 1..... 20
- Figure 5: Map of the experimental site during ECHO 2003; numbers on isopleths are heights [m] a. s. l. Map adapted from: see Index of Maps, Map 2..... 20
- Figure 6: Sodargram of reflectivity for antenna A3 for May 5<sup>th</sup> 2003, 12:00 to 24:00 CET. The black lines indicate the beginning of a new scan through the investigated set of acoustical frequencies..... 22
- Figure 7: Sodargram of reflectivity for antenna A1 for May 10<sup>th</sup> 2003, 00:00 to 12:00 CET. At 40 m and 45 m the reflectivity is increased due to a fixed echo. The periodical change is caused by the application of two acoustical frequencies for the sounding. .... 23
- Figure 8: Assemble-averaged profiles of reflectivity for acoustic frequencies 1.6 kHz (dashed line), 1.65 kHz (dash-dot line) and 1.7 kHz (dotted line), antenna A1. Times are CET..... 24
- Figure 9: Spectra of the backscattered energy from three different heights for June 3<sup>rd</sup> 2003, 14:45 CET. The emitted acoustical frequency was 1.65 kHz. .... 25
- Figure 10: Data processing scheme of the SODAR-RASS data. Standard averaging time is five minutes, longer intervals are averages from five minute average data..... 26
- Figure 11: Comparison of the horizontal wind speed  $v_h$ , measured with cup anemometers and with the SODAR system for the entire ECHO 2003 dataset. The solid line indicates the linear regression.  $n = 765$  and  $655$ , respectively. .... 27

Figure 12: Comparison of the measurements of virtual temperature from a tower ( $z = 120$ m), and the acoustic temperature from the corresponding gate of the RASS system for the entire ECHO 2003 dataset. The solid line indicates the linear regression. $n = 816$ .	29
Figure 13: Distribution of relative frequency of the wind direction $\varphi$ in $z = 40$ m for the entire WALDATEM-2003 dataset. $n = 5841$ .	30
Figure 14: Distribution of relative frequency of geostrophic wind direction $\varphi$ in $z = 600$ m for the entire WALDATEM-2003 dataset. $n = 868$ .	31
Figure 15: Mean profiles of the horizontal wind speed $v_h$ (line) and wind direction $\varphi$ (dotted) for a near ground approaching flow from sectors southeast (246 profiles), west (296 profiles) and north (260 profiles), according to Table 4. Bars are standard deviations.	31
Figure 16: Mean profiles of the horizontal wind speed $v_h$ (line) and wind direction $\varphi$ (dotted) for the W sector, for the entire WALDATEM-2003 dataset. Bars are standard deviations. The dash-dotted line shows a calculated profile, based on the power law.	34
Figure 17: Mean profiles of the horizontal wind speed $v_h$ (line) and wind direction $\varphi$ (dotted) for the SE sector, for the entire WALDATEM-2003 dataset. Bars are standard deviations.	35
Figure 18: Scatter plot of wind directions $\varphi$ in 40 m and 400 m for $\zeta > 0$ (stable range) with the three main sectors indicated by dashed lines. Around $240^\circ$ in 400 m a sudden jump from the west to the southeast sector can be observed, indicated by the vertical line.	36
Figure 19: Mean profiles of the horizontal wind speed $v_h$ (line) and wind direction $\varphi$ (dotted) for the N sector, for the entire WALDATEM-2003 dataset. Bars are standard deviations.	37
Figure 20: Dependency of the mean vertical wind speed $\bar{w}$ normalised with the horizontal wind speed $v_h$ on the wind direction $\varphi$ in $z = 40$ m for the entire WALDATEM-2003 dataset. A total of 6985 values are displayed.	38
Figure 21: Sodargram of the wind direction $\varphi$ from June 5 <sup>th</sup> to 6 <sup>th</sup> 2003. Effects mentioned in the text are marked with black lines.	40
Figure 22: Sodargram of reflectivity June 5 <sup>th</sup> to 6 <sup>th</sup> 2003. Effects mentioned in the text are marked with black lines.	40

Figure 23: Sodargram of the horizontal wind speed $v_h$ from 10 <sup>th</sup> to 11 <sup>th</sup> June 2003. The LLJ is marked with the circle, the black line indicates the time of the maximum intensity of the LLJ. ....	42
Figure 24: Sodargram of the wind direction $\phi$ from 10 <sup>th</sup> to 11 <sup>th</sup> June 2003. The region of the LLJ in Figure 23 is marked with the circle, the black line indicates the time of the maximum intensity of the LLJ in Figure 23.....	42
Figure 25: Sodargram of the potential temperature $\theta$ from June 10 <sup>th</sup> to 11 <sup>th</sup> 2003. The region of the LLJ in Figure 23 is marked with the circle, the black line indicates the time of the maximum intensity of the LLJ in Figure 23.....	43
Figure 26: Sodargram of the standard deviation of the vertical wind velocity $\sigma_w$ from June 10 <sup>th</sup> to 11 <sup>th</sup> 2003. The region of the LLJ in Figure 23 is marked with the circle, the black line indicates the time of the maximum intensity of the LLJ in Figure 23.....	43
Figure 27: Sodargram of the horizontal wind speed $v_h$ from 14 <sup>th</sup> to 15 <sup>th</sup> June 2003. The region of the LLJ is marked.....	44
Figure 28: Sodargram of the wind direction $\phi$ from June 14 <sup>th</sup> to 15 <sup>th</sup> 2003. The region of the LLJ shown in Figure 27 is indicated.....	44
Figure 29: Sodargram of the potential temperature $\theta$ from June 14 <sup>th</sup> to 15 <sup>th</sup> 2003. The region of the LLJ shown on in Figure 27 is indicated. ....	45
Figure 30: Sodargram of $v_h$ from July 6 <sup>th</sup> to 7 <sup>th</sup> 2003. The circle indicates the position of the LLJ.....	47
Figure 31: Sodargram of $\phi$ from July 6 <sup>th</sup> to 7 <sup>th</sup> 2003. The position of the LLJ from Figure 30 is indicated.....	47
Figure 32: Dependency of the altitude $z$ ( $v_{h \max}$ ) of the LLJ on the value of the wind speed maximum $v_{h \max}$ . The middle line represents the linear regression ( $R = 0.58$ ), the upper and lower line indicate $\pm 1$ standard deviation. $n=984$ for the entire WALDATEM-2003 experiment. ....	48
Figure 33: Sodargram of reflectivity from June 13 <sup>th</sup> to 14 <sup>th</sup> 2003. The boundary of the elevated maximum of reflectivity are marked.....	50
Figure 34: Sodargram of the wind direction $\phi$ from June 13 <sup>th</sup> to 14 <sup>th</sup> 2003. The boundary of the elevated maximum of reflectivity is marked.....	50
Figure 35: Sodargram of reflectivity from June 6 <sup>th</sup> 2003. The boundary of the elevated maximum of reflectivity is marked. ....	51

Figure 36: Sodargram of the wind direction $\varphi$ from June 6 <sup>th</sup> 2003. The boundary of the elevated maximum of reflectivity is marked.....	51
Figure 37: Sodargram of reflectivity from June 7 <sup>th</sup> 2003. The position of the elevating secondary maximum of reflectivity is indicated by the line. ....	54
Figure 38: Sodargram of the standard deviation of the vertical wind velocity $\sigma_w$ from June 7 <sup>th</sup> 2003. The line indicates the position of the elevating secondary maximum of reflectivity in Figure 37.....	54
Figure 39: Sodargram of reflectivity from June 21 <sup>st</sup> 2003. The position of the elevating secondary maximum of reflectivity is indicated by the line. ....	55
Figure 40: Sodargram of the standard deviation of the vertical wind velocity $\sigma_w$ from June 21 <sup>st</sup> 2003. The line indicates the position of the elevating secondary maximum of reflectivity in Figure 39.....	55
Figure 41: Development of the mixed layer ML on 12 days, as predicted by the Blackadar (1997) model. The two lines indicate the mean properties (solid: model; dotted: observations) of the mixed layer development within the lowest 1000 m. Vertical and horizontal bars are standard deviations.....	58
Figure 42: Comparison between the observed elevating rates of the MLH and the predictions from the Blackadar (1997) model. The solid line indicates the linear regression with $R = 0.10$ . ....	58

## 8. Index of Maps

- Map 1: TK 25, page 5837 Weißenstadt, 1973. Normalausgabe mit Waldflächen. Bayerisches Landesvermessungsamt, München.
- Map 2: TK 50, page L5104 Düren, 1979. Normalausgabe. Landesvermessungsamt Nordrhein-Westfalen, Bonn.

## 9. Index of Tables

Table 1:	Categories of LLJ given by Bonner (1968) with the additional category 1 given by Mitchel et al. (1995). $\Delta v$ indicates the drop of $v_h$ above the jet. The highest category with fulfilled requirements is valid. ....	17
Table 2:	Sounding parameters for the continuous measurements during WALDATEM-2003 and ECHO 2003. ....	25
Table 3:	Equation and coefficient of correlation R for the comparisons.....	28
Table 4:	Limits of the derived three main sectors for wind direction at the Waldstein site.....	30
Table 5:	Classes of the stability parameter $\zeta$ , used terms and the number of profiles (30 minutes averages) in each sector found for this class for the WALDATEM-2003 data.....	33
Table 6:	Observed LLJ events and their characteristics. The temperature gradient is a mean value for the entire LLJ event. ....	41
Table 7:	Characteristics of the observed shear layers during WALDATEM-2003.....	49
Table 8:	Absolute and relative frequency of the occurrence of typical patterns in the sodagram of reflectivity, according to Foken et al. (1987), modified. More than one pattern can be detected at one day or night.....	52
Table 9:	Observations of the development of the mixed layer height during WALDATEM-2003, using the reflectivity criterion after Beyrich (1997). ....	56
Table 10:	Mean development of the mixed layer height during WALDATEM-2003, using the category of diffusion according to KTA 1509 (Kerntechnischer Ausschuss, 1989), Table 7.4. $n = 15$ . ....	56
Table 11:	Model predictions of the mean development of the mixed layer height during WALDATEM-2003. $n = 12$ . ....	57

## 10. Index of the used abbreviations and symbols

### General symbols and abbreviations

ABL	atmospheric boundary layer	
CBL	convective boundary layer	
CET	Central European time (GMT +1)	
LLJ	low-level jet	
LST	local standard time	
ML	mixed layer	
MLH	mixed layer height	m
RADAR	radio detecting and ranging	
RASS	radio acoustic sounding system	
SBL	stable boundary layer	
SNR	signal-to-noise ratio	-
SODAR	sound detecting and ranging	

### Greek symbols

$\alpha_c$	classical attenuation coefficient	$m^{-1}$
$\alpha_e$	excess attenuation coefficient	$m^{-1}$
$\alpha_m$	molecular attenuation coefficient	$m^{-1}$
$\Delta T$	difference of air temperature between two measuring heights	K
$\Delta z$	difference between two measuring heights	m
$\zeta$	stability parameter = $z/L$	-
$\theta$	potential temperature	K
$\theta_v$	virtual potential temperature	K
$\Theta_B$	Bragg angle	°
$\kappa$	adiabatic coefficient of air (1.402)	-
$\kappa$	von-Kármán constant (0.4)	-
$\lambda_a$	wavelength of acoustic pulse	m
$\lambda_e$	wavelength of the electromagnetic wave	m
$\mu$	stratification parameter of the resistance law	-

---

$\Psi$	tilt angle against zenith	°
$\rho$	mass density of air	$\text{kg}\cdot\text{m}^{-3}$
$\varphi$	wind direction	°
$\sigma$	scattering cross section	$\text{m}^{-1}$
$\sigma_w$	standard deviation of the vertical wind velocity	$\text{ms}^{-1}$
$\tau$	transmitted pulse length	s

**Latin symbols**

A	antenna aperture	$\text{m}^2$
$A(\mu)$	universal function of the resistance law	-
$B(\mu)$	universal function of the resistance law	-
$c_a$	speed of sound	$\text{ms}^{-1}$
$c_p$	specific heat at constant pressure for moist air	$\text{J}\cdot\text{kg}^{-1}\text{K}^{-1}$
$C_N^2$	refraction structure parameter	$\text{m}^{-2/3}$
$C_T^2$	temperature structure parameter	$\text{Km}^{-2/3}$
d	displacement height	m
e	water vapour pressure	hPa
$E_R$	efficiency of received power	-
$E_T$	efficiency of transmitted power	-
f	frequency	$\text{s}^{-1}$
$f_e$	emitted frequency	$\text{s}^{-1}$
$f_s$	backscattered frequency	$\text{s}^{-1}$
g	acceleration due to gravity	$\text{ms}^{-2}$
G	effective aperture factor	-
k	wave number	$\text{m}^{-1}$
$l_i$	wavelength of inhomogeneity	m
$L_0$	Obukhov length determined within the surface layer	m
M	molar mass of air (0.02896)	$\text{kg}\cdot\text{mol}^{-1}$
n	number of samples	-
p	mean air pressure	hPa
p	power-law exponent	-
$P_R$	received acoustic power	W

---

$P_T$	transmitted acoustic power	W
$Q_{H0}$	sensible heat flux near the surface	$Wm^{-2}$
R	coefficient of correlation	-
R	universal gas constant (8.3145)	$J \cdot mol^{-1} K^{-1}$
$R_s$	distance of the scattering volume from the antenna	m
T	ambient air temperature	K
$T_a$	acoustic temperature	K
$T_v$	virtual temperature	K
$u_{*0}$	friction velocity near the surface	$ms^{-1}$
$V_h$	horizontal wind speed	$ms^{-1}$
$V_{h \max}$	maximum horizontal wind speed in a low-level jet	$ms^{-1}$
$V_r$	radial wind velocity	$ms^{-1}$
w	vertical wind speed	$ms^{-1}$
$\bar{w}$	mean vertical wind velocity	$ms^{-1}$
$w'$	fluctuation of vertical wind velocity	$ms^{-1}$
z	geometrical height	m
z-d	aerodynamically height	m
z ( $V_{h \max}$ )	geometrical height of the low-level jet maximum	m

## 11. Appendix A

### Technical specifications of the used SODAR RASS system.

#### *SODAR*

##### Type

- DSDPA.90/64

##### Manufacturer

- METEK, Meteorologische Messtechnik GmbH, Germany

##### Operating range

- Wind velocity  $0 - 35 \text{ ms}^{-1}$
- Wind direction  $0 - 360^\circ$
- Standard deviation of radial components  $0 - 3 \text{ ms}^{-1}$

##### Accuracy

- Wind velocity (  $0 - 5 \text{ ms}^{-1}$  )  $\pm 0.5 \text{ ms}^{-1}$
- Wind velocity (  $5 - 35 \text{ ms}^{-1}$  )  $\pm 10 \%$
- Wind direction  $\pm 5^\circ$
- Radial components  $\pm 0.1 \text{ ms}^{-1}$
- Standard deviation of radial components  $\pm 0.15 \text{ ms}^{-1}$

##### Range of measurements

- Minimum height 10 m
- Height resolution 5 – 100 m
- Availability 80 % up to 200 m

##### Transmitted frequency

- Tunable 1.0 – 4.0 kHz

**RASS**

## Transmitter

- Operating frequency 1290 MHz
- Transmitting power 20 W
- Frequency stability  $2 \cdot 10^{-6}$
- Single Side Band Phase-noise -100 dBc/Hz
- Modulation Continuous wave

## Receiver

- Detection phase synchronously with respect to transmit signal
- Noise Figure 1.5 dB
- Bandwidth  $32 \cdot (c_a / \Delta h)$  [ $\Delta h =$  height res. ]
- Noise Bandwidth  $(c_a / \Delta h)$

## Antennas

- Parabolic Dish diameter  $\varnothing$  1.8 m

**Entire system**

## Electrical values

- SODAR computer 230 V, 250 W
- Power supply 230 V, 2500 W

## Data transfer

- 4 RS-232 (V.24) interfaces 110 – 38400 Baud

## 12. Appendix B

### Technical specifications of the tower equipment at the research center Jülich.

#### *Cup anemometer*

##### Type

- Windgeschwindigkeitssensor LISA

##### Manufacturer

- Siggelkow Gerätebau GmbH, Germany

##### Startup speed

- $< 0.1 \text{ ms}^{-1}$
- Low startup speed due to solenoid bearing

##### Accuracy

- $\pm 1 \%$

##### Range of measurement

- $0 - 60 \text{ ms}^{-1}$

#### *Thermometer*

##### Type

- Ventilated aspiration psychrometer with PT100 sensor DIN 60751 B, 1/3 DIN-tolerance

##### Manufacturer

- Theodor Friedrichs Geräte und Systeme GmbH, Germany

##### Accuracy

- $\pm 0.1 \text{ K}$

***Relative humidity***

## Type

- 800 L 100

## Manufacturer

- Wilh. Lambrecht GmbH, Germany

## Accuracy

- $\pm 3 \%$

***Mean air pressure***

## Type

- PDC 8010

## Manufacturer

- Tiltz Industriemechanik

## Accuracy

- $\pm 1$  hPa, determined by comparisons with station barometer

## Acknowledgements

First of all, I wish to thank Prof. Dr. Thomas Foken for giving me invaluable support during the experiment and for very helpful discussions about analysis and interpretation of the data.

I am deeply grateful to Christoph Thomas, who gave me help and valuable support any time I needed one and encouraged me to develop a critical scientific style of working.

A special thank belongs to Prof. Dr. Franz X. Meixner from the Max Planck Institute for Chemistry for providing his SODAR-RASS system for the experiments.

I also wish to thank Dr. Johannes Lüers for his helpful ideas concerning the processing of the dataset.

A lot of thanks belong to the staff of the Bayreuther Institute für Terrestrische Ökosystemforschung (BITÖK), especially Johannes Olesch and Gerhard Müller for their active support during the experiment WALDATEM-2003.

A great thank belongs to my parents for supporting my studies, making this thesis possible.

I thank my friends Catharina, Sibylle, Florian and Klaus for reviewing this thesis and for their helpful ideas in many discussions.

Lastly, I wish to thank Hannele for understanding and encouraging me all the time during this work.

## **Eidesstattliche Erklärung**

Hiermit versichere ich, diese Arbeit selbstständig verfasst und keine anderen als die angegebenen Hilfsmittel und Quellen verwendet zu haben.

Bayreuth, den 11. März 2005

Jens Mayer